



Development and validation of a real time pumping kite model

M.B. Ruppert
August 20, 2012

Master of Science Thesis



Development and validation of a real time pumping kite model

MASTER OF SCIENCE THESIS

For the degree of Master of Science in Applied Sciences at the
Delft University of Technology

M.B. Ruppert

August 2012

Graduation committee:

Prof. Dr. W. J. Ockels
Dr. Ing. R. Schmehl
Dr.Ir. W.A.A.M. Bierbooms
Ir. R. van der Vlugt

Faculty of Aerospace Engineering
Faculty of Applied Sciences
Delft University of Technology



Copyright M.B. Ruppert
Cover photo is taken by M.B. Ruppert during the
technology demonstration of 22th June 2012 at
the Maasvlakte 2, Port of Rotterdam, Holland
All rights reserved

SUMMARY

A pumping kite system is a new innovative way to generate sustainable energy. A large kite is used to generate a pulling force which is transmitted to the ground by a tether. The tether is reeled off a drum that is connected to a generator. When the tether is completely unwound the kite is controlled in such a way it hovers down like a parachute, with almost no traction force, and the tether is reeled-in. This results in a cycle which produces a net amount of energy. Currently multiple institutes and companies are investigating and developing such pumping kite systems, including the ASSET institute at the TU Delft.

A simple, realistic and fast kite model is essential during the development of these systems. Such a model could be used for: estimation of the power production, structural optimization, trajectory optimization and for example autopilot development. This thesis describes the development of a realistic real time capable pumping kite model.

Initially a literature study gives an overview of the current models available in literature. It explains the advantages and shortcomings of the different approaches. Main shortcoming of most kite models is their limited validation. As a result their accuracy is unknown.

Secondary, the measurement data of a 20kW prototype, which has been developed by the ASSET kite group, is used in an extensive data analysis and system identification. The general dynamics are described and multiple relevant phenomena are found. Especially the rotation of the kite has been studied. A useful relation is found which couples the rotation of the kite to the steer input and the side slip angle (or gravitational vector). This relation originates from a moment study of the kite on a quasi-static basis and corresponds with measurement data. Further the sagging of the tether due to tether drag and pod dynamics has been studied. Relatively small sag angles of 0-15° are found during regular flights and a characteristic pattern indicates that especially the pod dynamics play a role in the flight dynamics. Finally the aerodynamic forces acting on the kite have been studied and coefficients needed for an aerodynamic force model have been fitted to the measurement data.

It is concluded, based on the literature study and data analysis, that a semi-rigid body modelling approach is most suited. The semi-rigid body model simulated the kite as a point mass with one additional degree of freedom, namely the rotation of the kite around the tether (yawing of the kite). The pitch angle of the kite, which is adjustable in the real system, is incorporated in the model by a variable constrain instead of an additional degree of freedom. The semi-rigid body kite model proves to be a simple and computer efficient model.

The kite model is connected to two different tether models. A single spring-damper tether model which simulates the tether as straight and a discretised point mass model which is able to simulate the dynamics of the tether and pod.

The kite model with both tether models have been validated by comparing the models to measurement data. Both models seem to realistically simulate the current kite system. The model with a straight spring damper tether model runs approximately 7x real time¹ and correctly simulates all variables except the sag of the tether. The discretised tether model simulates these effect correctly but at the cost of simulation speed. Currently it runs approximately 0.5x real time. The discretised model additionally shows more realistic behaviour during non-normal flight conditions.

¹ Running on a normal desktop computer with Intel Duo Core processor E4400 (@2.00 GHZ) and 2GB RA.M

PREFACE

As a child I was already playing with kites. Endlessly I could fly a kite at the beach and each year the kites became bigger and more powerful. But it would take a presentation of Prof. Dr. Wubbo J. Ockels during my master Sustainable Energy Technology to understand the possibilities of kites for power production. I'm still amazed by the idea and each time I see the 25m² kite gliding through the air the elegance of the concept becomes once more clear.

I took the photograph on the front cover of this thesis during a technology demonstration of the ASSET (TU Delft) kite group at the Maasvlakte on the 22 of June 2012. For me this picture shows the entire story of kite power and even sustainable development in general. On the left of the picture (and the reverse side of this thesis) you could see the Eneco coal power plant polluting our environment. Next to it stands the first generation of sustainable wind energy, the wind turbines. And high above the kite is flying producing energy. The picture immediately shows the various advantages of kite power. It flies higher, uses less material and is more versatile.

I have been interested in sustainable development for a long time. The development of new sustainable, reliable and distributed energy sources is of great importance. To contribute to such a new innovative idea has been a great experience.

I would like to thank Prof. Dr. Wubbo J. Ockels for starting the kite powered energy concept, giving me the opportunity to do this thesis. And for many interesting talks and ideas on the topic of sustainable energy.

My special thanks goes to my supervisors Dr. Ing Roland Schmehl. Over the past year he has helped me numerous times. Without his review and support this thesis would not have been here.

I would like to thank Dr.ir. W.A.A.M. Bierbooms for reading this thesis and being part of my graduation committee.

I would also like to thank all members of the Kite Power group. The many brainstorming and discussions have helped me tremendously in understanding the kite system and in the development of the model.

Finally I would like to thank my parents, friends, family and especially my girlfriend Rachel for all the support they gave me throughout this and the past years of my studies.

Delft, University of Technology

M.B. Ruppert

August 2012

CONTENT

Summary	v
Preface	vii
Content	ix
Nomenclature.....	xii
1 Introduction	1
2 Literature study	3
2.1 High altitude wind.....	3
2.2 High altitude wind power concepts.....	4
2.3 Market of high altitude wind power.....	6
2.4 Kite power research at the TU Delft	7
2.5 System layout of current system	8
2.6 Kite models in literature	12
2.7 Validation of kite models	26
2.8 Tether models in literature.....	29
2.9 Table of kite models.....	30
3 Thesis goal and approach.....	33
3.1 Goal.....	33
3.2 Approach.....	33
4 Reference frames and definitions	35
4.1 Table of reference frames.....	35
4.2 Earth fixed frames.....	36
4.3 Kite fixed reference frames.....	36
4.4 Steering and power values.....	37
5 Data analysis and System identification	39
5.1 Data selection	39
5.2 Positions and velocities.....	39
5.3 Forces.....	40
5.4 Power, energy and reeling speed	42
5.5 Orientation of the kite relative to the tether	44
5.6 Steering of the kite.....	47

5.7	Apparent wind speed model.....	53
5.8	Angle of attack and side slip angle.....	55
5.9	GPS Accuracy.....	55
5.10	Aerodynamic coefficients.....	57
5.11	Developed software to analyse data.....	61
6	Kite model.....	63
6.1	Model options.....	63
6.2	Semi rigid body kite model	64
6.3	Implementation in Simulink.....	74
7	Tether model.....	77
7.1	Model options.....	77
7.2	Discretised point mass tether model.....	78
7.3	Dyneema properties	83
7.4	Validation of tether model.....	83
7.5	Integration with kite model	85
7.6	Implementation in Simulink.....	86
8	Results and validation.....	87
8.1	Data selection	87
8.2	Altered lift curve	88
8.3	Positions and velocities.....	88
8.4	Forces and reeling speed	90
8.5	Power.....	91
8.6	Orientation of the kite relative to the tether	91
8.7	Angle of attack and side slip angle.....	92
8.8	Steer inputs.....	94
8.9	Simulation time.....	94
9	Conclusions	97
10	Recommendations.....	99

Appendix A: Parameters	101
Appendix B: Nomenclature	103
Appendix C: Reference frames	107
Appendix D: Transformation matrices of reference frames	115
Appendix E: Matlab code reference frames plotting tool	117
Appendix F: Experimental determination of Dyneema properties	121
11 References:	129

NOMENCLATURE

GENERAL SYMBOLS

\parallel	Parallel	[-]
\perp	Normal	[-]
$\langle \rangle$	Average	[-]

LATIN SYMBOL

a	Pseudo acceleration of the kite	m/s^2
\mathbf{a}	Inertial accelerations	m/s^2
$a(P_s)$	Forward/backward wingtip offset due to steer input P_s (twist)	m
A_ξ / A_η	Amplitudes of Lissajous-figures	rad
A_{kite}	Projected surface area $(\mathbf{XY})_B$	m^2
A_{side}	Projected side surface area of kite. $(\mathbf{XZ})_B$	m^2
A_T	Cross sectional area of the tether	m^2
b	Wing span	m
c	Strain-speed proportional damping constant tether	Ns/m
c_0	Unit damping constant	Ns
c_1	Yaw correlation coefficient 1 (w.r.t. steer input)	[-]
c_2	Yaw correlation coefficient 2 (w.r.t. gravity)	[-]
c_3	Yaw correlation coefficient 3 (w.r.t. side slip)	[-]
c_4	Side force correlation coefficient	[-]
$C_{\perp D,T}$	Normal tether drag coefficient	[-]
$C_{\parallel D,T}$	Parallel (friction) tether drag coefficient	[-]
C_D	Drag coefficient	[-]
C_L	Lift coefficient	[-]
C_R	Resultant aerodynamic force coefficient	[-]
C_S	Side force coefficient	[-]
C_Z	Aerodynamic moment coefficient (around \mathbf{z}_B axis)	[-]
d_T	Diameter tether	[m]
D	Resultant aerodynamic drag force	N
E_T	Tether elasticity modulus	N/m^2
\mathbf{F}	Resultant force	N
\mathbf{F}_{Aer}	Aerodynamic force	N
\mathbf{F}_{cf}	Centrifugal force	Nn
\mathbf{F}_{Drag}	Aerodynamic drag force	N
\mathbf{F}_{Gra}	Gravitational force	N
\mathbf{F}_{Lift}	Aerodynamic lift force	N
\mathbf{F}_{Tether}	Tether force	N
$\mathbf{F}_{Tether Drag}$	Drag force tether	N
$\mathbf{F}_{Tether Gra}$	Gravitational force tether	[-]
\mathbf{g}	Gravitational acceleration constant	m/s^2
G_e	Glide ratio (see (2-11))	[-]
I	Moment of inertia	$kg \cdot m^2$
k	Correction factor in mechanical energy equation	[-]
k	Spring constant tether	N/m

k_0	Unit spring constant	N
l_0	Length of unstretched tether element	m
l_j	Length of tether element j	m
L	Resultant aerodynamic lift force	N
\mathcal{L}	Lagrangian function of the kite system	J
m	Effective inertial mass of the kite and the cable	kg
\bar{m}	Effective gravitational mass of the kite and the cable	kg
m_{kite}	Mass of kite	kg
m_{pod}	Mass of control pod	kg
m_{tether}	Mass of tether	kg
M	Moment	N.m
p	Roll rate	rad/sec
\mathbf{p}^{OP}	Position vector, vector from origin to kite	m
\mathbf{P}	Position kite	[-]
P^{abs}	Measured potentiometer values	[-]
P_M	Mechanical power	W
P_p	Relative potentiometer power	%
P_S	Relative potentiometer steering	%
q	Generalized coordinates $q := (r, \vartheta, \eta)^T$ of the kite	[m,rad,rad]
\dot{q}	Pitch rate	rad/sec
Q	Generalized forces	N
r	Yaw rate	rad/sec
r	Spherical coordinates radius/length cable	m
r_{ref}	Unstretched tether length	m
\mathbf{R}_j	Position mass j	m
S	Scaling matrix	[-]
t	Time	sec
${}^A\mathbf{T}_B$	Transformation matrix from reference frame B to reference frame A	[-]
T_{kin}	Kinetic energy of kite and cable	J
U	Potential energy of kite and cable	J
\mathbf{U}	Input vector	[-]
\mathbf{v}_{App}	Apparent wind velocity	m/s
\mathbf{v}_{Cross}	Crosswind velocity (perpendicular to tether)	m/s
\mathbf{v}_{Kite}	Velocity of kite	m/s
\mathbf{v}_L	Reel out velocity winch	m/s
\mathbf{v}_{ref}	Wind velocity at reference height	m/s
\mathbf{v}_{Wind}	Wind velocity	m/s
WPD	Wind power density	W/m ²
\mathbf{X}	State vector	[-]
z	Height above ground	m
z_0	Surface roughness length	m
z_{ref}	Height of wind sensor	m

GREEK SYMBOL

α	Angular acceleration	rad/s ²
α	Aerodynamic angle of attack	rad
β	Aerodynamic side slip angle	rad
η	Elevation angle	rad
ϑ	Azimuth angle (w.r.t \mathbf{x}_{EG})	rad
$\theta^{K,SE}$	Pitch of kite relative to \mathbf{p}^{0P} (= straight tether assumption)	rad
θ_0	Pitch of kite w.r.t earth	rad
ξ	Azimuth angle (w.r.t \mathbf{x}_W)	rad
ρ_{air}	Density air (at height of the kite)	kg/m ³
ρ_{tether}	Density tether	kg/m ³
$\phi^{K,SE}$	Roll of kite relative to \mathbf{p}^{0P} (= straight tether assumption)	rad
ϕ_0	Roll of kite w.r.t earth	rad
χ_W	Downwind direction (azimuth angle w.r.t. \mathbf{x}_{EG})	rad
$\psi^{K,SE}$	Yaw (rotating) of kite around \mathbf{p}^{0P} (= straight tether assumption)	rad
ψ_0	Yaw of kite w.r.t earth	rad
$\omega^{EG,K}$	Rotation rates of kite (p, q, r)	rad/sec
Ω	Volume of the kite	m ³

ABBREVIATIONS

ASSET	Applied Sustainable Science Engineering and Technology
Avg	Average
CAD	Computer Aided Design
FEM	Finite Element Method
GUI	Graphical user interface

1 INTRODUCTION

Energy is the critical resource for every society. The availability and cost of energy determines for a large part the complexity and wealth of a society. Since the transition to a fossil fuel based society in the industrial revolution around 1800 the world's average per capita income increased over tenfold, while the world's population increased over six fold [1]. Due to the abundance of easy accessible energy in the form of fossil fuels the wealth of societies could grow tremendously. However the tide is turning. Currently the availability of easy energy is declining. More and more effort has to be made to produce the same amount of energy, which can clearly be seen on the increasing price of fossil fuels. Add to that the present awareness of the negative environmental side effects of fossil fuels, the fast growing world's population and the geopolitical problems concerned with the production and distribution of fossil fuels and you can understand the immense problem mankind is facing. To sustain our current level of wealth the quest for sustainable, low-cost and easy accessible energy is one of the most urgent challenges of today.

Currently there is a massive development going on in sustainable energy, in 2010 investments in sustainable energy grew 32% to 211 billion dollar [2]. Among the possibilities for sustainable energy are solar, hydroelectricity, wind, and biomass energy sources. One source of energy that has received significant attention over the years is wind. Wind power is currently one of the most affordable sources of renewable energy and has a large potential. But wind power has some complications. Wind power can only supplement a small fraction of the total energy needs. This has a number of contributing factors. Wind is not always present at low altitudes so a backup is required, wind turbines are expensive in comparison with conventional energy sources and wind turbines have a relative small power output, which means that a large number of wind turbines is needed. To overcome these problems a number of concepts for wind energy production at higher altitudes have come up. This could solve some deficiencies because at higher altitudes the wind is more powerful and consistent [3].

In this report, one particular concept for extracting the energy available in the high altitude winds is explored. In 1980 Loyd wrote a visionary paper exploring the possibility of generating electrical power using the pulling force of a tethered airfoils, i.e., kites [4]. The concept is named the pumping kite power system. The concept does not attempting to locate the wind turbine system at high altitudes but the wind at high altitude is used to mechanically drive a ground based generator. A large kite generates a pulling force which is transmitted to the ground by a tether. The tether is reeled of a drum that is connected to a generator producing energy. When the tether is completely unwound the kite is controlled in such a way it hovers down, like a parachute, with almost no traction force and the tether is reeled-in. This results in a cycle which produces a net amount of energy. Due to the cyclic behaviour this concept is called a pumping kite system.

The market potential of high altitude wind technology has been assessed by Gerrard Hassan [5]. The main conclusion is "From what is visible now of the young airborne technology and industry the concepts seem to have a promising potential to play a vital role in the renewable energy sector". Evidently the worldwide interest in high altitude wind is growing fast in the past years [6]. Multiple research groups and companies are researching and developing systems for high altitude wind energy systems. Most of them, including the ASSET group at the TU Delft, are exploring the option of the pumping kite system. At the ASSET group at the TU Delft a first pumping kite power system prototype was successfully tested in 2007.

Many research question have still to be answered to perfect the system and to be able to make it a commercial competing product. Nevertheless the potential of high altitude wind energy is substantial, M. Ippolito, founder of the high altitude wind power company KiteGen, shows it as follows: "A single hypothetical fan of only 20 cm in diameter, immersed in the jet stream, could actually provide plenty of energy for a house all year round, both day and night" [7].

Most research groups and companies are developing computer models of the system to assist the development of the system. There is a need for realistic models of the system for various purposes among which: estimating the energy production, structural optimization of the system, optimization of kite trajectories, controller software development and for example to train kite pilots. Realistic modelling of a pumping kite system has however proved to be challenging. A kite is flexible and will deform due to aerodynamic forces and steer inputs, the deformation will influence the shape of the kite which influences the aerodynamic forces. This is obviously a loop and challenging to model.

There are multiple pumping kite models described in scientific literature all slightly different in assumptions, approach and complexity. Currently very little is known about the validity of these models. The models are limited or not at all validated. This has multiple causes. Currently only a couple of research groups have a prototype and could do validation but even then it proved to be difficult to measure all states of the system.

This thesis focuses on the evaluation (and validation) of present pumping kite models described in literature. This will be done by comparing existing pumping kite models described in literature with data from the prototype available at the TU Delft. The final goal is the development of a real-time kite power model which simulates the present kite power system from the TU Delft realistically.

The first part of the thesis forms the literature review and is focused on the current status of technology with respect to kite modelling (chapter 2). The second part analyses the measurement data of the prototype of the TU Delft. An extensive data analyses and system identification gives insight in the dynamics of the system (chapter 5). In the third part the development of a kite models is described (chapter 6 and 7). After which the developed model is compared with measurement data (chapter 8). Finally conclusions are drawn (chapter 9) and recommendations for further development and improvements are given (chapter 10).

2 LITERATURE STUDY

Aim of this literature study is to give an overview of the current status of technology with respect to modelling of a pumping kite power systems. To understand the background first the wind at high altitude and different high altitude wind energy concepts are explored. After that a broad overview of the present kite models is given.

2.1 HIGH ALTITUDE WIND

Wind is formed by a complex interaction between solar radiation, earth's rotation, and a variety of other factors. Generally it can be said that wind is increasing with altitude and that the wind is forming bundles of fast winds generally located between 7 and 16 km of altitude called jet streams [3]. In these streams there is a constant wind with average speeds in the order of 40 m/s. At lower altitudes the earth's surface slows down the wind. The wind profile between 0 and 500m is mainly influenced by the earth surface and can be described with the 'log law' which is defined by [8]:

$$\mathbf{v}_{\text{Wind}}(z) = \mathbf{v}_{\text{ref}} \frac{\ln\left(\frac{z}{z_0}\right)}{\ln\left(\frac{z_{\text{ref}}}{z_0}\right)} \quad (2-1)$$

Where z is the altitude, \mathbf{v}_{ref} is the known wind speed at reference height z_{ref} and z_0 is the surface roughness length that varies from 0.03 for smooth surfaces such as a lake or ocean to 2 for an urban area with tall buildings. The height above ground where surface friction has a negligible effect on wind speed is called the "gradient height". Typical values for the predicted gradient height are 460 m for large cities, 370 m for suburbs, 270 m for open terrain, and 210 m for open sea [9].

Real wind data gives a picture of the wind profile above the gradient height. In Figure 2-1 the average wind in relation to height is given for a place, the Bilt, in the Netherlands. For this graph daily wind data from the KNMI is used over a period of 20 years [10]. It can be seen that wind speeds increase till 10 km and average wind speeds at 10 km height are 7 times higher than at ground level.

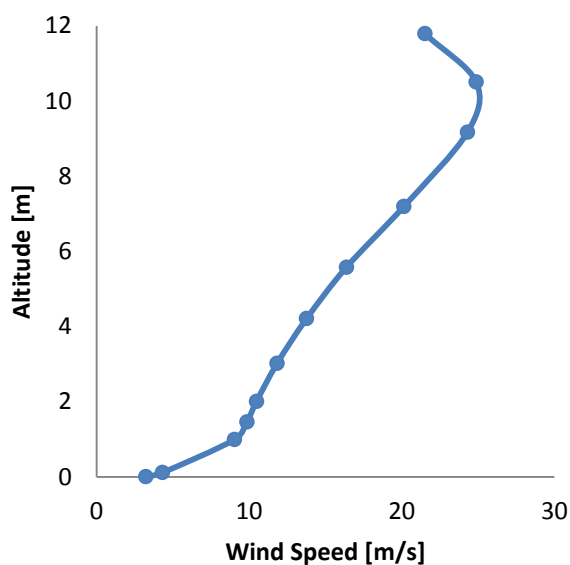


FIGURE 2-1, AVERAGE WIND SPEED IN 'THE BILT' [10]

Altitude KM	Available Power [kW/m ²]
0,00	0,041
0,11	0,091
0,99	0,771
1,46	0,901
2,00	0,986
3,01	1,240
4,21	1,738
5,57	2,520
7,19	3,818
9,16	5,042
10,50	4,477
11,78	2,428

TABLE 1, WIND POWER DENSITY VS. ALTITUDE

The power available in the wind is expressed by the wind power density (WPD):

$$WPD = \frac{1}{2} \rho_{air} V_{Wind}^3 \quad (2-2)$$

This formula clearly shows the significance of higher wind speeds. The power available increases with the cube of the wind speed. Hence, doubling the wind speed increases the available power by eight times. It should be mentioned that the air density reduces at altitude but still the effect is large. Table 1 displays the available wind power at different heights. It can be seen that around 50 times more energy is available at 10 km. It is this fact that resulted in many concept for wind energy production at high altitude. In addition the wind is more consistent at higher altitudes [3].

In 2009 Archer and Caldeira [11] assessed the global amount of energy available in the jet streams and found that the wind speeds in the jet stream are an order of magnitude faster than those near the ground and reach an average wind speed of 40m/s. They calculated that the total wind energy in the jet streams is roughly 100 times the global energy demand and reach energy density's over 10kW/m² at optimal places. There is still some debate on-going if the values stated are realistic. Miller, Gans and Kleidon [12] published a critical report stating that only 7.5TW is available which is two orders of magnitude lower than the estimates of Archer and Caldeira and that high altitude wind power extraction will have substantial environmental side effects. Nevertheless, even if the findings of Miller are correct and 'only' 7.5TW is available this would result in an enormous potential resource of renewable energy.

2.2 HIGH ALTITUDE WIND POWER CONCEPTS

High Altitude wind power systems are electro-mechanical systems that extract power from the kinetic energy of the winds high in the sky. To harness the energy available at high altitude a variety of systems have been proposed. In this literature study only the 'pumping system' and the 'drag power system' are reviewed. Both concepts are first described by Loyd [4]. The concepts, the application of crosswind power and the model Loyd derived still form the basis of most of present high altitude wind power concepts and research. An overview of the other concepts can be found in the market study of Gerrard Hassan [5] and the work of Schmehl [13].

2.2.1 PUMPING KITE CONCEPT

The first system Loyd proposed used the large pulling forces of a kite to pull a tether off a drum. Loyd called this option 'lift power' because the lift of the kite was responsible for the tether force. Nowadays this is called a 'pumping kite system' or 'traction kite system'. Figure 2-2 illustrates the concept. A kite is attached to a long tether that is connected to a power generator on the ground. The process consists of two phases: the generation phase and the retraction phase.

During the generation phase the kite is controlled such that it delivers a high pulling force to the cable. This is achieved by flying the kite crosswind, commonly in a lying figure of 8 pattern. At the same time a cable is reeled of a drum that is connected to a generator which generates electricity. When there is no cable left on the drum, the system goes into retraction phase. The kite is controlled in such a way that there is a minimum tension. In general this is reached by changing the pitch of the kite. This kite state is called 'de-powered' and generates almost now force. In the retraction phase the generator is used as a motor and reels the tether and kite in. When the portion of the cable that was pulled out is fully retrieved, the generation phase starts again. The energy needed to reel in the kite during the retraction phase is only a fraction of the energy that is produced during the generation phase.

This results in a cyclic (pumping) process with a phase which generates energy and a phase that consumes energy, but with a net positive effect. This is illustrated in Figure 2-3 where the mechanical power during a couple of cycles is shown. The data is mechanical power is measured during a test flight of the current pumping kite prototype of the TU Delft .

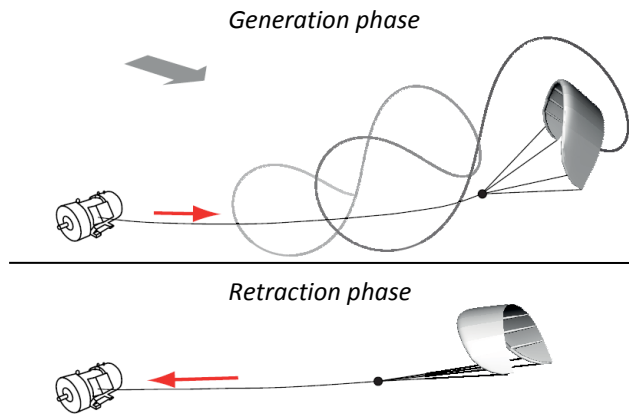


FIGURE 2-2, WORKING PRINCIPLE OF THE PUMPING KITE SYSTEM [14]

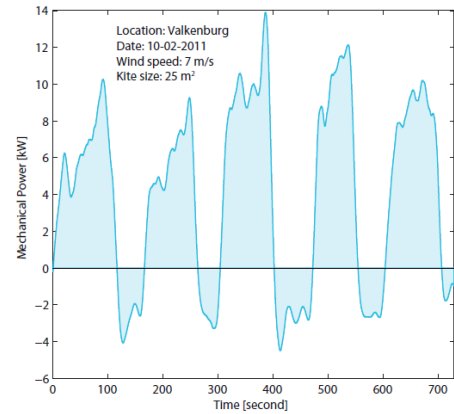


FIGURE 2-3, POWER PRODUCTION

2.2.2 DRAG POWER CONCEPT

A second option Loyd proposed was the so called 'drag power concept'. This concept is basically a flying windmill. A kite, or other flying object, flies across the air on a fixed tether (Figure 2-5). When flying in a pattern the kite reaches high speeds. In this concept the kite is slowed down by a rotors which is connected to a generator placed on the kite. The rotor generates power which is transported to the surface via the tether. Advantage of this approach is that in contrary to the pumping kite power system a continuous energy production is accomplished. Loyd calculated that theoretical both concepts generate the same amount of energy. Disadvantage is the added weight of rotors, generators and the thicker cables, due to the transport of electricity to the ground, which lower the performance. Currently a Californian company, Makani Power inc, is exploring this option. Advantage is that the generators could also be used as motors and therefore the flying apparatus could easily do automated launch and landing procedures.



FIGURE 2-4, DRAG POWER CONCEPT OF MAKANI POWER [15]



FIGURE 2-5, DRAG POWER CONCEPT, GENERATORS MOUNTED ON WING [15]

2.2.3 CROSSWIND POWER

In Loyd's paper there were some important findings, he calculated with a simple model that a kite with an area of 576m^2 could produce 6.7MW in the drag concept. But besides that Loyd noticed the importance of crosswind, far more energy can be extracted by flying a kite across the air. When a kite is flown across the air a so called apparent wind is created. The apparent wind speed is the wind experienced by the kite. This wind is a result of the wind and the velocity of the kite. When flying in the so called wind window the apparent wind is higher than the wind velocity.

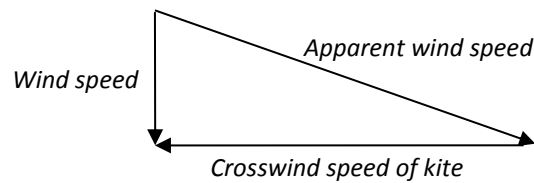


FIGURE 2-6, APPARENT WIND SPEED VECTOR

The forces of the kite and as well the power produced increase with the apparent wind speed and therefore flying across the air increases the total generated energy. The modelling is further explained in 2.6.1, the principle of crosswind is further studied by Terink [16].

2.3 MARKET OF HIGH ALTITUDE WIND POWER.

Between 2000 and 2012 the worldwide interest in renewable energy en high altitude wind power has grown tremendously. Worldwide multiple company's and research groups started to develop high altitude wind power systems. The graph displays the number of institutes involved with high altitude wind power.

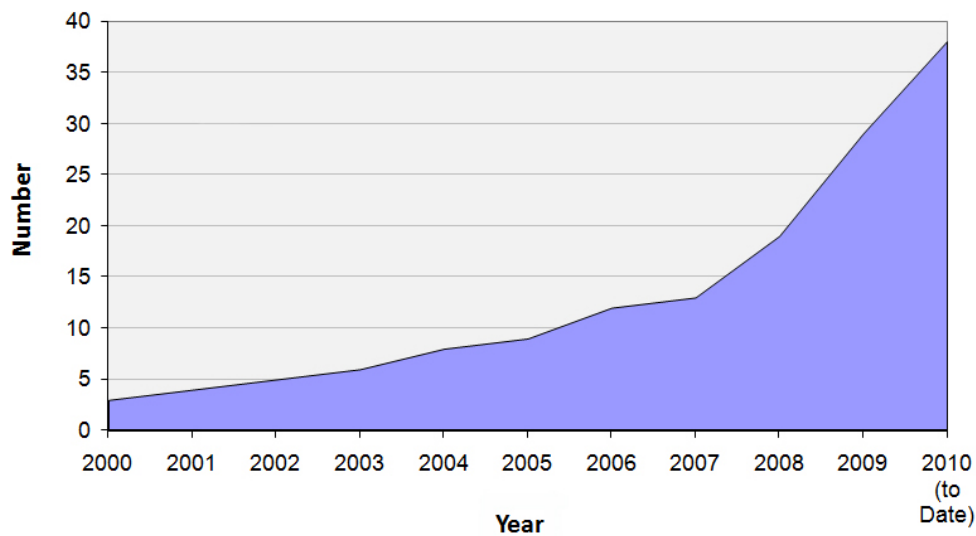


FIGURE 2-7, NUMBER OF INSTITUTES INVOLVED IN HIGH ALTITUDE WIND ENERGY [17]

An overview of all institutes and there concept choices can be found in the market study of Gerrard Hassan and the status report 'Airborne Wind Energy 2011' of Schmehl [5, 13]. Following Gerrard Hassan the predominant concepts choice is the pumping kite concept followed by the drag power concept. Almost all research groups have futuristic concepts however for the initial development they start with the 'simple' pumping kite and drag power concept.

This thesis focuses on the validation and development of models for pumping kite systems. Therefore a small overview is given from institutes currently developing pumping kite systems.

Research groups	Research	Prototype	Approximately people involved
ASSET, TU Delft	All facets of the system	20 kW prototype	20 [18]
KU Leuven	Mainly control	Small rotating lab test for control purposes	16 [19]
Politecnico di torino, Italy	All facets	Prototype 10 kW	Terminated 2011
ETH Zurich, Fachhochschule Nordwestschweiz	All facets, focus on advance kite technology, tensairity	Prototype 10 kW	20 [20]
Sussex University, England	Control, visual tracking	Kite with control pod	4 [21]
Research Institute of Mechanical Engineering Problems, Rusia	Analytic modelling, Control	-	4
Lisboa Roskilde, Denmark	Aerodynamic force modelling	-	2
Norwegian University of Science and Technology	Modelling	-	3

TABLE 2, RESEARCH GROUPS IN PUMPING KITE POWER SYSTEMS, JUNE 2012

Companies	Prototype size	Remark	People involved
Skysails	55 kW Prototype	+ 60 million	40 [22]
Ampyx power	10 kW Prototype		11 [23]
KiteGen	3 MW Prototype 10 kW Prototype		9 [24]
Windlift	12 kW prototype	Funded by U.S. Department of Defence	4 [25]
Enerkite	30 kW prototype	100 kW Groundstation	8 [26]

TABLE 3, COMPANIES IN PUMPING KITE POWER SYSTEMS, JUNE 2012

2.4 KITE POWER RESEARCH AT THE TU DELFT

Ockels started in 2004 a research group at the TU Delft which studies the use of kites for energy production. Initial research focused on an alternative high altitude wind power concept, called the Laddermill, which Ockels patented in 1996 [27]. In the Laddermill concept multiple kites or wings are coupled together in one system to form an endless loop. For more information see [10].



FIGURE 2-8, LADDERMILL CONCEPT [10]

After evaluating the Laddermill concept it was concluded [28], that controlling and understanding a single kite was already difficult enough and as a result the focus shifted towards the pumping kite systems and crosswind power. In 2007 the first pumping kite power system prototype was successfully tested [29]. By the end of 2010 a successful demonstration was made with a second prototype with a power of 20 kW. The last years were used to gain more insight in the system and current research focuses on optimizing the energy output, designing better kites and fully automating the system. In 2011 the first automated flight was recorded.

2.5 SYSTEM LAYOUT OF CURRENT SYSTEM

The aim of this thesis is the modelling of the current kite power system. Therefore an overview is given from the current kite power system. The kite power system can be split into five subsystems as seen in Figure 2-9

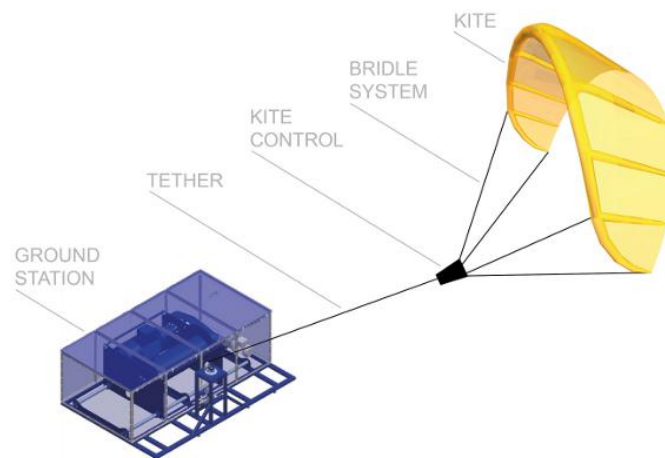


FIGURE 2-9, CURRENT 20KW PROTOTYPE [18]

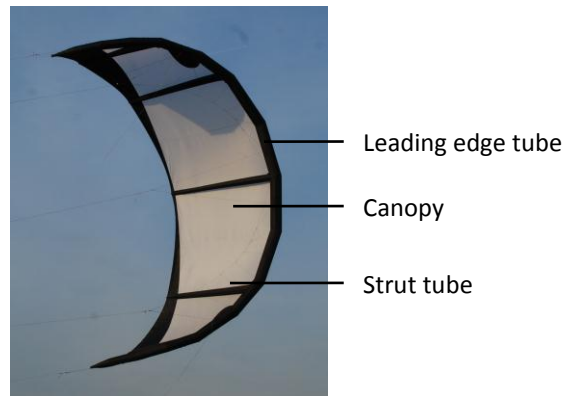
KITE

A kite is a tethered airfoil. As an airfoil moves through the air, the pressure difference between the upper side and the underside of the wing generates a lifting force. This force is responsible for the acceleration of the kite and the pulling force in the line. In the past, kite designing was mainly a trial and error process. Due to the interest in high wind power systems and also due to the fast growing sport of kite surfing the interest in more advanced kite research picked up. Presently kites are developed at the TU Delft on a more scientific basis.

The main requirements of a kite intended for power production are a high maximum pulling force, a high depower ratio, and good controllability of the kite [30]. The need for a high pulling force is obvious, this is achieved by an aerodynamic efficient kite with a high wing loading. The depower ratio is the ratio between the force during the reeling out phase and the reeling in phase. This ratio must be as high as possible to lower the energy wasted during the retraction phase. Lastly the kite should be controllable and stable. Higher depower ratios generally decrease the controllability, so a compromise has to be made.

These kite properties are currently found in kites used for kite-surfing and therefore the current kite design is based on commercial kites for kite-surfing. Especially in the so called LEI-Kites. A LEI Kite consists of three basic elements: a leading edge (LE) tube, strut tubes and a canopy. The leading edge and strut tubes give structural stiffness and additionally the leading edge tube defines the shape of the nose of the wing. The canopy completes the wing. For kite power application a bridle is added to the LEI-kites to handle the increased wing loading. The advantage of LEI-kites above other concepts is the high depower ratio and controllability.

Currently two LEI kites are used at the TU Delft. The first kite is a 25m² LEI kite which has been specially designed for kite power application. The design is based on the design of the F-series from Mutiny Kites [31] however the design has been strongly modified and improved over the past years. The second kite is a 14m² commercial LEI-kite, The Hydra from Genetrix [32], which is slightly modified for kite power applications. The 25m² Mutiny kite is used for low to medium wind conditions and the Genetrix kite is used in high wind conditions. A new kite is developed based on the concept of the Genetrix kite. Main improvement in the Genetrix kite compared to the Mutiny kite is the higher maximum pulling force due to a higher maximal surface tension and a different layout of the bridle (see Bridle and Tether).

FIGURE 2-10, THE HYDRA 14M²FIGURE 2-11, MUTINY 25M² V2

Key numbers:

	Hydra	Mutiny
Surface	14	25
Projected surface	11	18 M2
Weight	10 kg	12 kg
Aerodynamic Performance	-	5-6
Maximum Surface tension	55kg/m2	33 kg/m2
Maximum Pulling force	6000 N	5800 N
Bridle concept	No pulley's	With pulley's
Tensairity principle used	Yes	No

TABLE 4, KITE PARAMETERS

In the future new, more innovative kite shapes are intended to be developed. One of the possibilities developed at the TU Delft is the 'Kiteplane'. The 'Kiteplane' is a conceptual name for an inflatable kite, which can ascend like a kite and descend like an airplane. More information can be found in the work of Terink [16].



FIGURE 2-12, KITEPLANE

BRIDLE AND TETHER

The bridle is responsible for the redirection of aerodynamic forces into the tether and the support of the kite. Due to the bridle the kite is able to keep the desired shape and the canopy tension is redirected and reduced. Further the bridle plays an important role in the depowering of the kite. Figure 2-13 shows the concept, due to the bridle the kite can rotate, by doing so the angle of attack is lowered which reduces the aerodynamic performance [33].

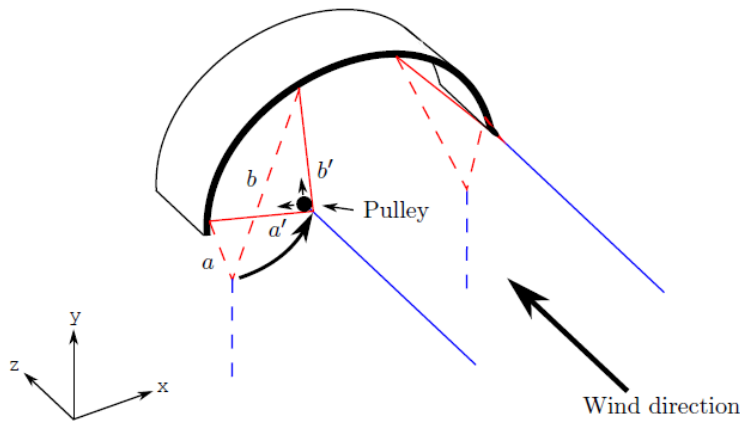


FIGURE 2-13, BRIDLE LAYOUT TO ACCOMMODATE ROTATING OF THE KITE

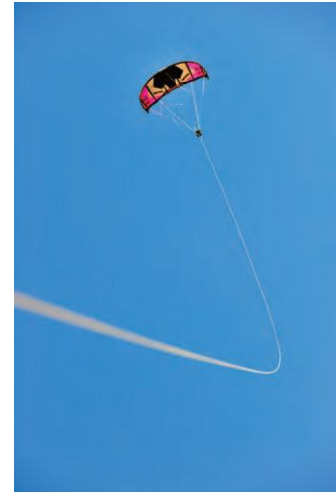


FIGURE 2-14, TETHER SAG

The tether guides the forces of the kite to the ground station. The mass of the tether becomes much higher than the mass of the kite when flying with long and thick tethers and the drag force on the tether increases as well with the tether length as with the diameter. As a result the tether has an important role in the system dynamics. Effects like sag of the cable can clearly be seen when flying on a cable of 300m (Figure 2-14). To minimize these effects the tether line should be light and with minimal aerodynamic drag. Currently a 4 mm tether is used made out of ultra-high-molecular-weight polyethylene (UHMWPE) - developed by DSM with a total length of 1,000 m.

CONTROL UNIT

To control the kite a wireless control unit is used. The control unit controls the steering and the pulling force of the kite with two servo motors. The pulling force is changed by altering the kite's angle of attack. Further the control pod gathers multiple sensors data and transmits it to the ground station by a wireless link.

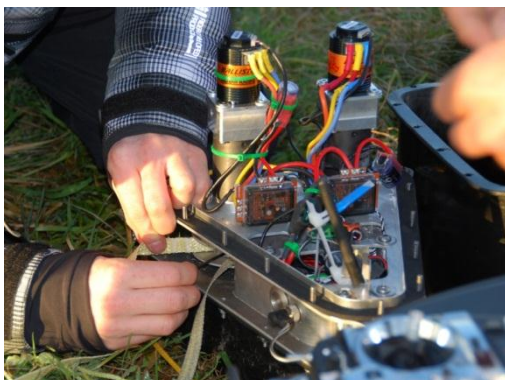


FIGURE 2-15, CONTROL POD



FIGURE 2-16, CONTROL POD UNDER KITE

GROUNDSTATION

The ground station converts the pulling force in the tether to electricity. It consists of a motor, a drum and all electronics needed to control the ground station. The motor is a synchronous motor which also works as a generator. This thesis will not go into detail about the dynamics of the ground station, but assumes that the winch is able to give a predefined force on the tether or a predefined reeling velocity. More information about the ground station and modelling of the ground station can be found in the study of Schölkopf [34].

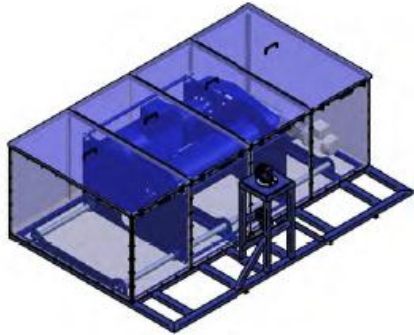


FIGURE 2-17, CAD DRAWING GROUNDSTATION



FIGURE 2-18, INSIDE GROUNDSTATION

SENSORS

In the system there are multiple sensors present which measure the state of the system. Main sensors are the X-Sence MTI-G sensor in the kite which is measuring the position, velocities, accelerations and orientation of the kite. Further the forces and reeling speed of the tether are measured at the ground station and the wind velocity is measured at a wind station positioned at 6 m height. Finally there is a pitot tube between the bridle to measure the apparent wind velocity. All sensor data is sent to the control software located at the ground station.

2.6 KITE MODELS IN LITERATURE

Almost all research groups use and developed system models for multiple purpose. Most models are used to assess the potential of kite power or for control purposes. The models described in the various published papers differ slightly in complexity and assumptions. This chapter gives an overview of the current models used for kite power systems. First the simple analytic models are describe after which the point mass model is explained. Secondly the rigid body model is explained. Finally the more complex multi plate models, multi body and FEM models are elaborated. A table with all models is present in 2.9.

2.6.1 ANALYTIC MODELS

Analytic models form the basis of kite power system modelling. The analytic models are mainly used for assessing the potential of the kite system but also give a baseline for the more complex models. The basis of the analytic model is found in the paper of Loyd [4]. The analytic model is further expanded by Terink and Argatov [16, 35, 36].

CROSSWIND MOTION LAW

Starting point for Loyd's analytic model is the fact that the kite can be seen as an weightless tethered plane. Like an airplane the kite produces lift and drag forces as it moves relative to the air. The analytic model is based on the assumption that there is equilibrium between the three forces, the lift and drag forces and the tether forces. The model neglects the inertia and weight of the kite.

The lift and drag forces are calculated with the widely used aerodynamic formulas [37]:

$$L = \frac{1}{2} \rho_{air} C_L A_{kite} |\mathbf{v}_{App}|^2$$

$$D = \frac{1}{2} \rho_{air} C_D A_{kite} |\mathbf{v}_{App}|^2$$
(2-3)

Where ρ_{air} is the density of air, A_{kite} is the projected area of the kite, C_L and C_D are the lift and drag coefficient of the kite for the current flight condition and \mathbf{v}_{App} is the apparent wind speed. The apparent wind speed is the velocity of the air passing the wing. It can be computed as:

$$\mathbf{v}_{App} = \mathbf{v}_{Wind} - \mathbf{v}_{Kite}$$
(2-4)

Where \mathbf{v}_{Wind} is the wind vector, and \mathbf{v}_{Kite} in the velocity vector of the kite. Loyd derived the so called crosswind motion law, when equilibrium between the forces is assumed a relation for the apparent wind speed can be obtained.

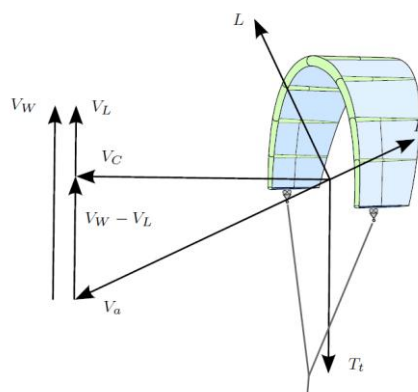


FIGURE 2-19, CROSSWIND EQUILIBRIUM LOYD [4]

In Figure 2-19 the force and velocity vectors are shown and the following relation can be deduced:

$$\mathbf{v}_{\text{Cross}} = (\mathbf{v}_{\text{Wind}} - \mathbf{v}_L) \frac{L}{D} \quad (2-5)$$

Where \mathbf{v}_L is the reel out speed of the line and $\frac{L}{D}$ is the lift over drag ratio of the whole kite system including the tether. The lift over drag ratio is also called the glide ratio and is equal to $\frac{C_L}{C_D}$. Loyd assumes that the inclination angle with the earth's surface is zero and that the kite flies perfectly crosswind (=parallel to the ground). The relation couples the speed of the kite to the aerodynamic performance. With the crosswind motion law it is possible to find an analytic formula for the power production of a kite power system:

$$P_M = \frac{1}{2} \rho_{\text{air}} C_L A_{\text{kite}} |\mathbf{v}_{\text{Wind}}|^3 k \quad (2-6)$$

Where k is a function describing the operational mode of the kite. When the kite is flying in crosswind motion, which is the most useful operational mode for a pumping kite system, the coefficient k is given by:

$$k = \left(\frac{L}{D} \right)^2 \left(\frac{v_L}{v_{\text{Wind}}} \right) \left(1 - \frac{v_L}{v_{\text{Wind}}} \right)^2 \quad (2-7)$$

Most interesting is to find the maximum power production of such a system. Loyd deduces that the maximum value of k is:

$$k^{\text{max}} = \frac{4}{27} \left(\frac{L}{D} \right)^2 \quad (2-8)$$

Which occurs at

$$v_L = \frac{1}{3} v_{\text{Wind}} \quad (2-9)$$

This means that the optimal reel out speed of a kite power system is approximately one third of the wind speed (when flying optimal crosswind with a zero inclination angle).

REFINED CROSSWIND MOTION LAW

Argatov [35] further expanded Loyd's analytic model. Loyd's analytic model is for a special case of the kite moving orthogonally to a uniform wind flow. In reality the kite constantly changes direction with respect to the wind and violates Loyd's equation. Argatov establishes the refined crosswind motion law, which determines the relation between the crosswind speed of the kite ($\mathbf{v}_{\text{Cross}}$) and the wind (\mathbf{v}_{Wind}) in all flight conditions. Further he extended the analyse of Loyd by taking into account some effects of gravity and tether drag. Based on the refined crosswind motion law the force in the tether can be calculated as:

$$F_{\parallel \text{Aer}} = \frac{1}{2} \rho_{\text{air}} A_{\text{kite}} C_L G_e \sqrt{1 + G_e^2} (v_{\parallel \text{Wind}} - v_L)^2 \quad (2-10)$$

Where the subscript 'll' means the component parallel with the tether. So $v_{\parallel \text{wind}}$ is the wind component in the direction of the tether. G_e is the effective glide, which is the lift of drag ratio of the whole kite system.

As noted before the tether adds drag to the kite system. Therefore the effective glide ratio is estimated as:

$$G_e = \frac{L}{D + F_{tether}} = \frac{C_L}{C_D + \frac{C_{\perp} r d_T}{4A_{kite}}} \quad (2-11)$$

With the forces known, Argatov estimates the mechanical energy with:

$$P_M = v_L \left(\frac{1}{2} \rho_{air} A_{kite} C_L G_e \sqrt{1 + G_e^2} (v_{\parallel wind} - v_L)^2 + F_{\parallel cf} - F_{\parallel Gra} - F_{\parallel Tether Gra} + F_{\parallel Tether Drag} \right) \quad (2-12)$$

Where $F_{\parallel cf}$ are the average centrifugal forces, $F_{\parallel Gra}$ are the average gravitational forces, $F_{\parallel Tether Gra}$ is the average effect of the weight of the cable and $F_{\parallel Tether drag}$ is the average drag component along the cable. Only the components in direction of the tether are included. Similar to Loyd's analysis Argatov optimises the reeling speed for maximum power. The following optimum reeling speed is found:

$$v_L = \frac{1}{3} v_{\parallel Wind} + \frac{F_{\parallel cf} - F_{\parallel Gra} - F_{\parallel Tether Gra} + F_{\parallel Tether Drag}}{\rho_{air} A_{kite} C_L v_{\parallel Wind} G_e \sqrt{1 + G_e^2}} \quad (2-13)$$

The second term is found to be very small. Argatov gives a numerical example and shows that effect of the second term is less than 1%. As a result almost the same equation as Loyd (2-9) is derived, except that the fact that the optimal reeling speed now depends on $v_{\parallel Wind}$ instead of v_{Wind} .

Argatov continues by estimating the average mechanical power over a 'figure of 8' trajectory. The following illustrative formulas are derived.

$$\begin{aligned} \langle P_M^{\max} \rangle &\approx \frac{1}{2} \rho_{air} A_{kite} C_L v_{Wind}^3 \cos^3 \eta_* k_0 k_* \\ k_0 &= \frac{4}{27} G_e \sqrt{1 + G_e^2} \\ k_* &= 1 + \frac{2}{3} \frac{\langle F_{\parallel cf} \rangle - \langle F_{\parallel Gra} \rangle - \langle F_{\parallel Tether Gra} \rangle + \langle F_{\parallel Tether drag} \rangle}{\rho_{air} A_{kite} C_L k_0 v_{Wind}^2 \cos^2 \eta_*} \end{aligned} \quad (2-14)$$

Here η_* is the mean inclination angle of the kite with respect to the horizon. It is found that the effects of the correction terms k_* is approximately 1 and k_0 is almost $\frac{4}{27} G_e$. So the formula can be further simplified to:

$$\langle P_M^{\max} \rangle \approx \frac{1}{2} \rho_{air} A_{kite} C_L v_{Wind}^3 \cos^3 \eta_* \frac{4}{27} G_e^2 \quad (2-15)$$

For an mean inclination angle of $\eta_* = 0$ and neglecting all external forces we again see the result obtained by Loyd (2-6). Equation (2-15) shows the relevant variables of a pumping kite system and is useful as a baseline model. Note that only the reeling-out phase is simulated. In reference [36] Argatov incorporates the reeling-in phase and performance coefficients of different open loop and closed loop figures are found.

In reference [38] the analytic model is used to do a structural optimization of the kite power system. In reference [39] the effect of steering and inertia on the model are studied. Both effects do not have a substantial impact on the prediction of average power. In addition the effect from tether sag on the kite's angle of attack is investigated.

2.6.2 POINT MASS MODEL

The analytic models described in are a limited representation of reality, at least the orientation and the inertia and weight effects are neglected. For control purposes, optimal trajectory finding and performance analysis a dynamic model is needed which takes into account these effects. The most simple way to do this is via a point mass model. In a point mass model the kite is modelled with a lift and drag force acting at a point mass placed at the center of gravity of the kite. Diehl published a point mass model in 2001 which formed the basis of many studies [40].

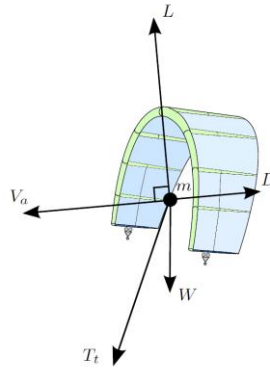


FIGURE 2-20, POINT MASS MODEL

Figure 2-20 shows the model of Diehl. v_{App} is the aerodynamic velocity, L is the lift force, D the drag force T_{tether} is the resulting tether force and W the weight of the point mass.

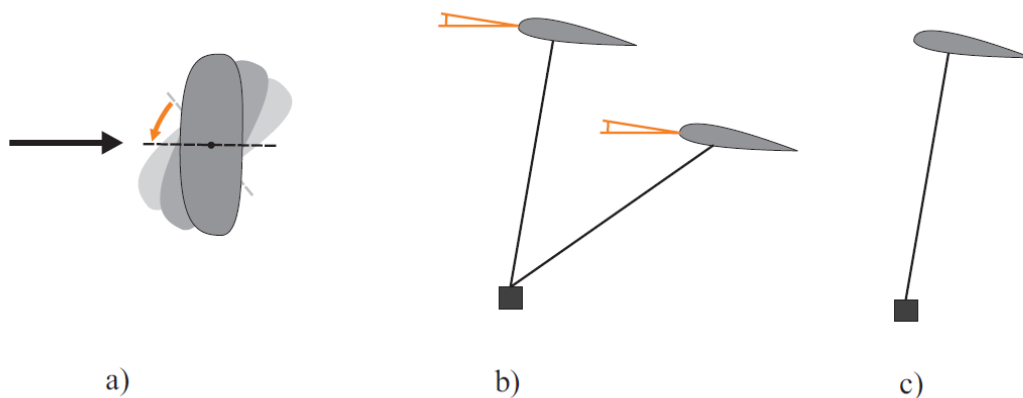


FIGURE 2-21, MODELLING ASSUMPTIONS DIEHL [41]

The model is based on three assumptions (Figure 2-21). First of all it is assumed that the kite immediately aligns itself to the apparent wind speed. As a result the side slip angle is assumed to be zero.

This assumption has been studied by Baayen with video analysis [42]. Figure 2-22 and Figure 2-23 shows frames of the video.



FIGURE 2-22, NO SLIP DURING STRAIGHT FLIGHT [43]



FIGURE 2-23, SIDE SLIP DURING TURNS [43]

It was observed that this assumption is a good estimate during high apparent wind speeds, i.e. when doing crosswind flying. In low apparent wind conditions, low speed manoeuvres and in proximity of the edge of the wind window, the kite flies with an offset. Second assumption is a constant angle of attack. Again this assumption is approximately valid for high apparent wind speeds. Thirdly the tether was simulated as rigid, so the flexibility of the tether was neglected.

As a result of these assumptions the kite orientation is coupled to the apparent wind. The drag force is defined parallel to the apparent wind speed vector. The lift force is by definition perpendicular to the drag force. This leaves one degree of freedom. The last degree of freedom, the rotation of the lift vector around the drag vector, is used for control and is defined by the angle of the lift in respect to the straight tether.

In a point mass model the steering of the kite is simulated due to directly rotating the lift vector. In literature this control method is often referred to as 'roll' of the kite. This is however incorrect. Due to the rotation of the lift vector a side force is applied to the point mass. Due to the side force the kite obtains a sideways acceleration which results in a different kite velocity. This leads to a change in the direction of the apparent wind. The orientation of the kite will rotate along with the apparent wind (since it is fixed by definition). This rotation of the kite is a combination of mainly yaw and a little roll (depending on the angle of attack).

Disadvantage of the point mass model is that it neglects the attitude dynamics and flexible modes. The orientation of the kite is directly coupled to the wind vector and position vector. This prevents the correct calculation of angles of attack and sideslip angles.

The basic point mass model by Diehl is applied and extended in various papers for different purposes. Nevertheless the basic principles stay the same. Differences can mainly be found in the aerodynamic forces model (see chapter 2.6.9) and sometimes a tether model (see chapter 2.8) or a variable angle of attack is added. Chapter 2.9 gives an overview of the current models available and their function. Point mass models are used in kite research because they are relatively easy and computer efficient. Since a point mass has only three degrees of freedom the differential equations stays limited to a 6th order ODE. This makes it possible to do real-time modelling and the model can be used for all kinds of control purposes.

2.6.3 RIGID BODY MODEL

A rigid body is an idealization of a solid body of finite size in which deformation is neglected. In a rigid body model forces and moments are applied to this non-deformable body which results into displacements and rotations of the body. In contrast to the point mass model the rigid body has an orientation and therefore takes into account attitude dynamics. An aircraft can be regarded to a great extent as a rigid body and is in general modelled by rigid body models. To overcome the limitations of the point mass kite model some attempts have been undertaken to simulate the kite as a rigid body.

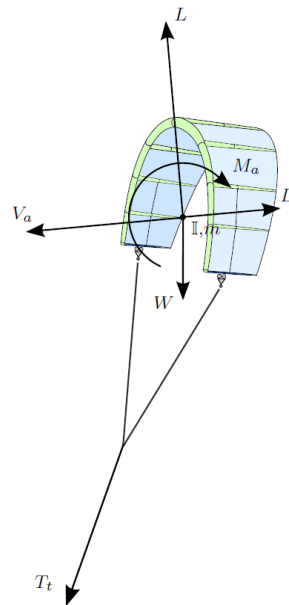


FIGURE 2-24, RIGID BODY MODEL

Figure 2-24 shows illustrative the principle of a rigid body model, where compared to the point mass model moments are present and the kite has a moment of inertia I . A rigid body has six degrees of freedom resulting in a set of six equations of motion, three for translation and three for rotation. The performance of a rigid body models depends mainly on the aerodynamic forces and moments modelling. The aerodynamic forces and moments are calculated in the body reference frame. This in contrast to the point mass model where the aerodynamic forces are calculated in the wind reference frame.

Currently only two rigid models attempts are described in literature. Williams [44] describes an approach for a standard rigid body model. In order to utilize the rigid kite model aerodynamic parameters for the kite have to be found. A Tornado vortex-lattice software is used to find an initial guess for the aerodynamic parameters. His paper shows a working kite model and real test data from the TU Delft prototype however no comparison is made between the model and the test data.

Limitations of the point mass and rigid body model became apparent by realizing that a surf kite does not produce the steering entirely through a roll, pitch or yaw manoeuvre but the kite is also structurally deformed. The deformations induce additional changes to the direction of forces and moments as well as changing inertia properties. A second problem of the rigid body model is the stiffness of the model. Large forces and the small inertia results in stiff differential equations. To correctly simulate the dynamics of the rigid body small time steps are needed.

To overcome the problem of the deforming kite and changing inertia properties de Groot [45] developed a new approach. By reducing a complex multibody kite model of Breukels [46] (see 2.6.7) to a rigid body model. The flexibility of kite is taken into account in the rigid model by using aerodynamic parameters and an inertia tensor which changes depending on the steer input and apparent wind velocity. Thus by changing the aerodynamic

parameters and inertia tensor depending on the steer input and apparent wind velocity the deforming kite shape is simulated. This theoretically would give a realistic kite model. However the identification of the aerodynamic and structural model is difficult. De Groot uses the multibody kite model of Breukels for the aerodynamic and structural model identification. He is able to determine an aerodynamic and structural model as a function of the states of the rigid body model. The identified aerodynamic and structural model is implemented in the rigid model. The validation is performed by simulating the rigid body model and comparing it to the multibody model.

Advantage of this approach is the fact it incorporates the flexibility of the kite and still the kite is modelled as a rigid body which is fast to solve. However the aerodynamic and structural model has to be found for every flight condition. Currently the parameters are found by using the more complex multibody simulation of Breukels, this is found to be very time consuming and error sensitive. It is still the question if real test data could be used for the derivation of the aerodynamic force model. Further the model is never validated with test data. In the results can be seen that the aerodynamic model depends strongly on the steer inputs and apparent wind speed. This makes it questionable if the current aerodynamic force model is appropriate. It is doubtful if the kite model will give realistic results compared to actual test data.

2.6.4 SEMI RIGID BODY MODEL

The two rigid body models described above are the only efforts currently found in literature. An explanation is the problems in deriving a correct aerodynamic model and the fact that the light structure results in very stiff differential equations. To overcome the problem off the stiff differential equations several solutions are proposed. The key is the realization that some degrees of freedom are constrained in the kite system. Due to the bridle two axis of the kite are basically constraint. There is one axis around which the kite can turn. In addition the translation of the kite is constrained in one direction by the tether. This observation led to multiple models where some of the degrees of freedom are reduced.

Terink [16] models a kiteplane by five degrees of freedom. The first three degrees of freedom are the spherical coordinates of the tether end point. Since the kite plane is laterally bridled to the tether, the connection between the tether and the kiteplane is represented by a hinge that allows pitching of the kiteplane. This pitching motion is actually the fifth degree of freedom. The fourth is the longitudinal rotation of the tether. The rotation around the tether in fact determines the orientation of the hinge connection.

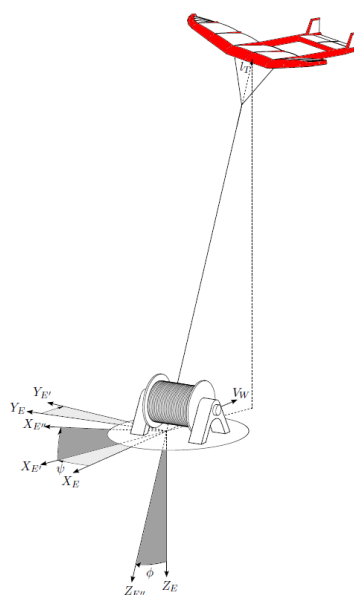


FIGURE 2-25, DEGREES OF FREEDOM IN KITEPLANE MODEL TERINK [16]

The equations of motion for the kiteplane system are derived using Lagrangian mechanics with the five degrees of freedom as generalized coordinates. Terink uses the model to assess the dynamic stability of the kiteplane and for control.

Knappskog [47] proposed a kite model based on four degrees of freedom. Contrary to Terink, Newtonian mechanics are used. Knappskog simulates only three translational and one rotation. This seems a valid assumption since the bridle constrains the rotation of the kite in two directions. This simplification leads to simpler and faster models. Nevertheless the correct modelling of the aerodynamic force remains essential.

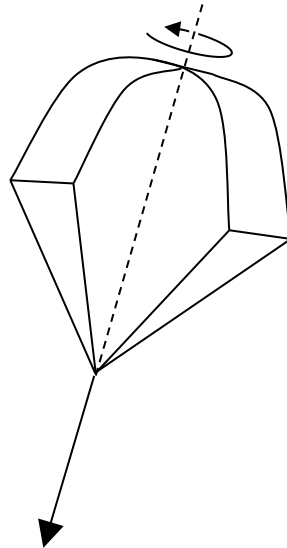


FIGURE 2-26, SEMI-RIGID BODY MODEL KNAPPSKOG [47]

The last semi-rigid body model worth describing is the 9-DOF model of Houska [48]. Like stated before rigid body models normally only have 6 degrees of freedom but it is possible to extend rigid models to include various flexible modes. Houska proposes two things. First of all three degrees of freedom are added. Namely the individual position of the two control cards and as a third degree of freedom the movement of the tips towards each, this movement is found to be characteristic for surf kites and is called 'jellyfish' movements. The second thing Houska proposed was to simulate the inertia of the kite on a quasi-static basis. Houska [48] states that the inertia forces are very small compared to the external aerodynamic forces and therefore are negligible. This assumption immediately solves the problems with the stiff differential equations.

2.6.5 MULTI-PLATE MODEL

In literature Williams tried to overcome the problems with the non-flexible rigid body model by simulating the kite as a so called multi-plate model [49, 50]. In this model the kite is simulated as a set of plates which are connected to each other by springs and hinges. Figure 2-27 shows a picture of the concept.

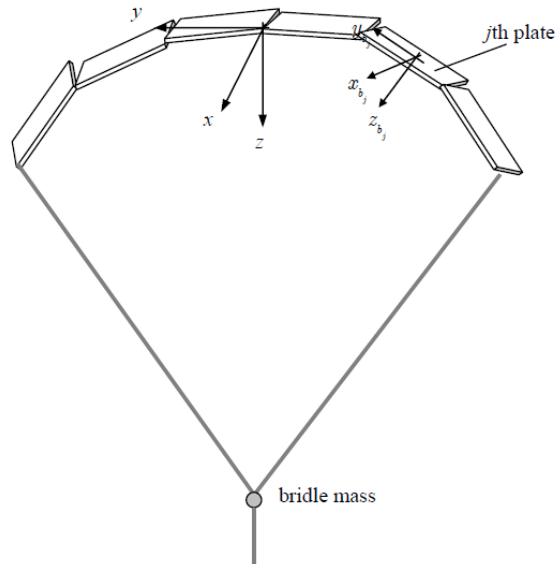


FIGURE 2-27, MULTI-PLATE MODEL [49]

Because the kite is simulated as a set of plates it is possible to simulate the deformation of the kite. Each plate has its own angle of attack and side slip angle. In this model steering is simulated due to the structural deformation of the kite and the shift of aerodynamic forces as a result. This is a big improvement in contrary to the steering in rigid body models where steering is solely simulated by changing aerodynamic forces. Also the change of inertia due to the deformation is taken into account. To find the equations of motion Williams used the method of Lagrange.

According to Williams a disadvantage of this mathematical model is that it can be difficult to establish an equilibrium configuration. A correct balance has to be found for a certain flight condition between the lift and drag forces, gravity, tether tension and aerodynamic moment. Furthermore the equations of motion are highly nonlinear and complicated which makes it hard to find analytic solutions in general.

Another difficulty is the identification of the coefficients off the hinges and springs between the plates. These have to be estimated to simulate the deformation of the kite realistically.

2.6.6 LUMPED MASS MODEL

Furey [51] proposed another model approach to simulate the deformation of the kite. By modelling the kite as two rows of five point masses connected to each other with constraints. Figure 2-28 gives an overview of the model.

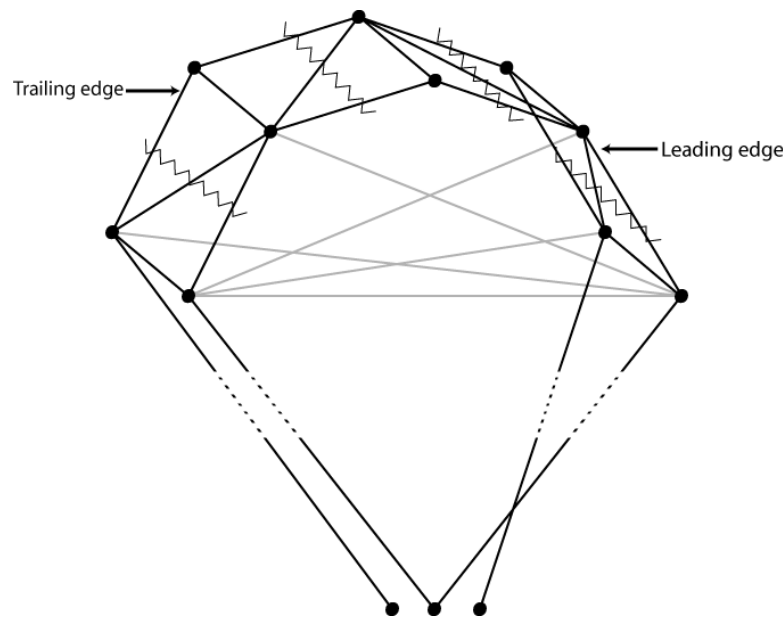


FIGURE 2-28, LUMPED MASS MODEL [51]

The aerodynamic forces are calculated in the same method as in the multi-plate model. The kite is sliced at four places as marked by the zigzag lines from the leading to trailing edge. The aerodynamic force on a section of canopy depends on its angle of attack and the apparent wind velocity to which it is subjected.

The motivation for this type of model was to provide a framework, which allows explicit consideration of variation in the kite configuration in terms of kite shape, bridle setup, and physical properties of the kite such as relative rigidity and mass of kite components. Specific anticipated defects can then be introduced to the system and the adequacy of the controllers' reaction assessed.

Difficulty with this model is that such a particle system easily become unstable. Especially since high forces and relatively small masses are simulated. Therefore the use of constraints has to be done with care. The lumped parameter model uses a relatively small time step of 0.004 to avoid numerical instability.

2.6.7 MULTI BODY MODEL

A more complex kite model was developed by Breukels [46]. He wanted to simulate the flexibility of the kite realistically without going to complex FEM-fluid-structure interaction. The choice was made to use the principles of multi-body dynamics to simulate a kite structure and its dynamic behaviour. Multi-body dynamics describes the motions of an assembly of rigid and constrained bodies. The different rigid bodies are connected with springs, dampers and hinges. A kite simulation toolbox was developed with the multi-body dynamics software package MSC-Adams. The toolbox consists of three elements or building blocks of which different kite configurations can be assembled. The building blocks are cables, inflatable beams and foils. An aerodynamic force model was developed, based on CFD calculations.

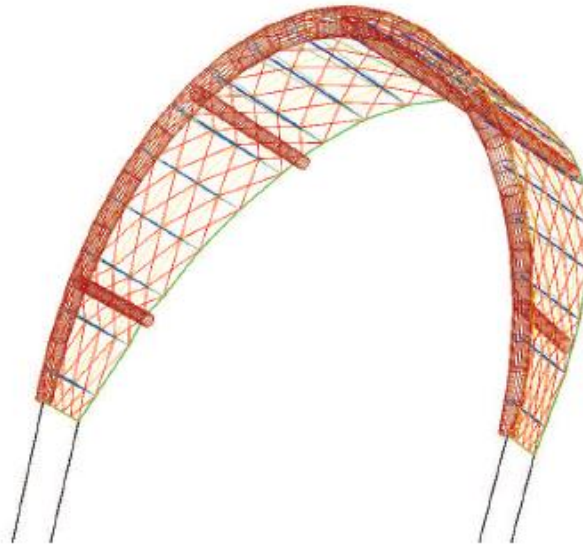


FIGURE 2-29, KITE IN MSC ADAMS [46]

Like stated before the accuracy of the model greatly depends on the correct parameters for all elements. In the multi-body model many parameters have to be found. Breukels did extensive research to find all parameters. The model could be used for design purposes and advance kite research. In Breukels thesis the model is used for the research into cornering of the kite and stability analysis. The simulation times for such a complex model increase rapidly. In the kite model shown above there are 400 degrees of freedom. The simulation is found to run around 10-100x slower than real time.

A disadvantage for this approach is that many artificial parameters are used. In addition it is difficult to implement a new kite. Each kite has to be individually build up from the building blocks. For example the new kite has a curved tip and a bridle. Both elements are not implemented yet in the kite toolbox.

2.6.8 FEM MODEL

At present kite models based on finite element method are being developed at the TU Delft. In a FEM model the kite is divided into multiple elements. In contrast to the multi-body model the elements are not rigid but deformable. The deformation of the elements is determined by the material properties of the kite, so instead of fitting parameters to a multi-body model the deformation of the kite is realistically determined by inserting structural properties in a FEM model. Schwoll [52] modelled a kite with aid of the FEM software of MADYMO. MADYMO has been developed for the car industry and is widely used for car crash analysis. Especially they are known for their airbag simulation. By coupling a CFD model to the FEM model they are able to simulate an airbag inflation realistically. Schwoll was able to insert the kite into the FEM software however multiple problems still have to be solved. Especially the kite seems to be far too stiff. This is probably due to local defects in the kite which are inadequately simulated. Further research is needed. Bosch [53] as well developed a FEM kite model. Bosch managed to couple the FEM model to the aerodynamic model of Breukels. The model still has to be validated and the aerodynamic force model has to be improved. The model currently runs 10-20 times real time but could be improved.

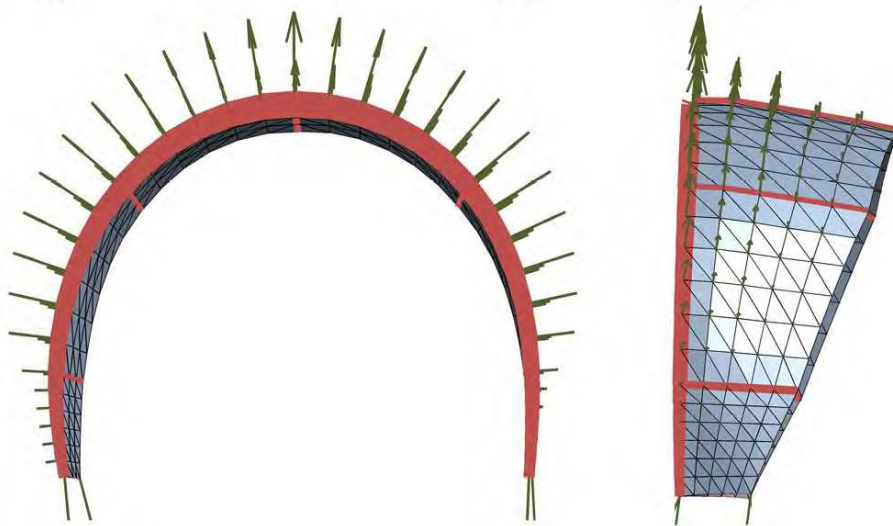


FIGURE 2-30, FEM MODEL [53]

2.6.9 AERODYNAMIC FORCES MODEL

All models described use an model to calculate the aerodynamic forces. The aerodynamic forces and moments depend on the pressure distribution around the kite. To calculate the resultant aerodynamic forces and moments often the theory of aerodynamic derivatives is used. Background of these models can be found in aircraft literature where aerodynamic derivatives are widely used for modelling the dynamics of aircrafts. Reason for the use of aerodynamic derivatives is the fact that the forces could be calculated computational efficiently. The derivation of these coefficients is for example explained by Mulder [54]. Analytic, point mass, rigid body, semi rigid body, multi plate and lumped mass models all use models based on the theory of aerodynamic derivatives.

The derivation of aerodynamic coefficients starts by defining the states where the aerodynamic forces and moments depend on. This is based on experience or a dynamic analysis. Obviously the number of states determines the maximum number of aerodynamic derivatives and therefore indirect also the complexity of the aerodynamic model. Generally more complex models have more advanced aerodynamic force models. Most point mass models have a fixed lift and drag coefficient while rigid body models have aerodynamic models based on the angle of attack, sideslip angle, rotations speed and steer input.

For the multibody and FEM kite models the pressure distribution over the kite is needed. The only aerodynamic model available is the model developed by Breukels [46]. Based on CFD calculations a model is developed that determines the force distribution based on the local angle of attack and position on the kite.

The model of Breukels still has its limitations. New aerodynamic force models are being developed. Ideally a CFD program would be coupled to a FEM model. However, this is currently not possible since the meshing has to be done manually and CFD programs are very computer intensive. A simpler aerodynamic force model is needed. Carqueij [55] developed a new, computationally light algorithm, which determines the aerodynamic loading on a kite. The model couples a Vortex Lattice Method with 2D airfoil data iteratively and takes into account the effects of airfoil thickness and the effects of viscosity. The computational time of the new coupled algorithm is approximately 400 times faster than a CFD simulation. Carqueij establish that the agreement between his aerodynamic model and the CFD results is excellent for cases where the flow remains attached over the kite.

Currently two master students at the TU Delft are researching the possibilities of using the method of Carqueij and other computer efficient methods to generate a fast aerodynamic force model.

2.6.10 SUMMARIZATION

Looking at the kite models described some conclusions can be made. First of all it could be said that the field of kite modelling has taken a tremendous flight over the last 8 years. Except the visionary paper of Loyd of 1980 there was no real basis (and interest) for kite modelling. In the past 8 years many attempts have been undertaken to model a kite realistically and computer efficiently. The requirements of the model depend on the application and therefore different kinds of models are designed. From simple analytic models to complex FEM-CFD models. From this literature study it can be concluded that almost all models have their shortcomings. Simulating a deformable structure that interacts with air proved to be challenging for many research groups. A couple of general remarks on kite modelling can be made:

First of all there is the trade-off between the numbers of degrees of freedom and the simulation speed. More degrees of freedom are able to simulate the deformation of a kite, however will also result in slower simulation. Especially due to the high aerodynamic forces and low weight of the kite the differential equations become stiff resulting in small time steps and slow simulations. This trade-off resulted basically in two kinds of kite models: the kite models which do not simulate the deformation of the kite (analytic, point mass, rigid body) and the ones who do (multi plate/lumped mass, Multibody, FEM). The first category is faster but the question is if the deformation can be omitted. The models often try to superimpose the effects of the deformation in the aerodynamic force model. The second category simulates the deformation but can be slow and non-physic parameters have to be fitted to simulate the structure (except for the FEM model). Ideally the number of degrees of freedom is exactly sufficient to simulate all important displacement modes of the kite and neglects the rest. This could be accomplished by reducing a multi-Body model or FEM model. However, a validated FEM model is currently not available and improvements in the multibody model are needed.

A second remark is the trade-off in the aerodynamic force model. The simple models, analytic, point, rigid, use aerodynamic forces model based on aerodynamic coefficients. These parameters have to be found and the question is on which state variables they depend and how linear they are. The number of state variables taken into account differs greatly between the models. Further the effects of the flexibility of the kite are sometimes incorporated in the aerodynamic force model. The more complex models, multibody, FEM, simulate the flexibility of the kite themselves so in theory a simpler aerodynamic force model is needed. The only model currently available for the complex models is the aerodynamic force model developed by Breukels.

On the next page a short overview is made of all kite models.

Point Mass	<p>DOF 2-3</p> <p>Advantage Fast to solve</p> <p>Neutral Orientation is coupled to the wind reference frame</p> <p>Disadvantage No attitude dynamics Not reliable in low v_{App} conditions. Limited aerodynamic model Deformation of kite not modelled</p>
Rigid Body	<p>DOF 6</p> <p>Advantage Fast to solve Attitude dynamics Could apply theory developed in aircraft literature</p> <p>Disadvantage Deformation of kite not modelled Very stiff differential equations</p>
Multi-plate / Lumped mass	<p>DOF +/- 30</p> <p>Advantage Simulates partly the deformation of the kite Attitude dynamics</p> <p>Disadvantage Use of non-physical hinge and spring forces Difficult to stabilize, extra constraints are used or unstable. Very stiff differential equations</p>
Multibody	<p>DOF +/- 400</p> <p>Advantage Simulates the deformation of the kite Attitude dynamics Extensive aerodynamic model</p> <p>Disadvantage Use of non-physical hinge and spring forces Time consuming to construct a kite Slow</p>
FEM	<p>DOF +/- 400 - 30000</p> <p>Advantage Simulates the deformation of the kite Attitude dynamics Extensive aerodynamic model Internal stresses are immediately known</p> <p>Disadvantage Slow Meshing difficulties</p>

2.7 VALIDATION OF KITE MODELS

Validation is the process of determining the degree to which a model, and their associated data are accurate representations of the real world from the perspective of the intended use. Without correct validation of the developed model the correctness and accuracy is unknown. From all models described in this literature study above only a few are partly validated. Main reason for the limited validation of the kite models is the difficulties in measuring all states of the kite system in test flights. All kite models depend on the wind speed at the height of the kite which cannot be measured. Most often the wind speed is based on the wind speed on the ground corrected with a wind shear model. Small error in the wind speed easily results in big errors since the forces depend to the square of the wind speed. In addition the actual position and orientation of the kite proves to be difficult to measure. GPS and IMU sensors have measurement errors and sometimes loose 'fix' especially in high dynamic movements (see also 5.9). Finally the deformation of the kite should be measured to be able to validate the advanced kite models. The dynamic measurement of the deformation of the kite is difficult.

Dadd [56], Weillenmann [57] and Fagiano [58] all partly validated their model with test data. Dadd compared two different models, the analytic model and point mass model with each other and with test data (see Figure 2-31 and Figure 2-32). The measured forces and velocities are compared with the modelled values. Dadd uses the measured position of the kite as input for his model. As a result only the aerodynamic force model is tested. The results show a general agreement between the measured and predicted data however for some parts the differences are substantial. Also the time showed is very short.

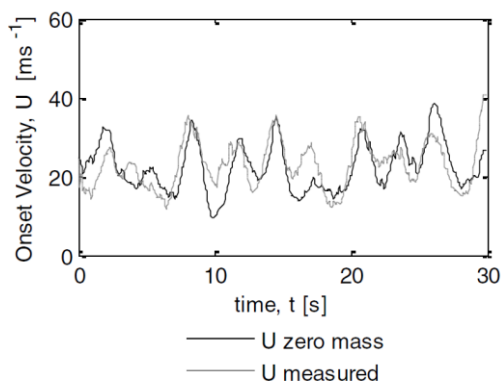


FIGURE 2-31, COMPARISON OF KITE VELOCITY [56]

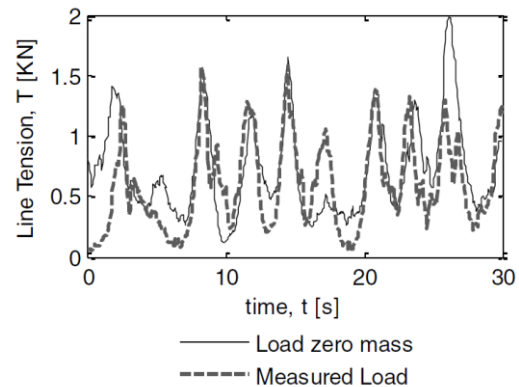


FIGURE 2-32, COMPARISON OF LINE TENSION [56]

Fagiano and Weillenmann uses the same approach for point mass models. Fagiano compares forces and power and Weillenmann forces and accelerations (Figure 2-33 and Figure 2-34). Further Weillenmann attempted to simulate the point mass model with the same steer input and initial condition as reality and compare the position of the kite for a short period (Figure 2-35). In general the forces comparison shows general agreement. Weillenmann observed that the differences are especially found during sharp turns which is explainable by the limited modelling of turning in the point mass models. When Weillenmann tried to simulate the model with the same steer input the model gave out the same results for 3-4 sec after which they deviate.

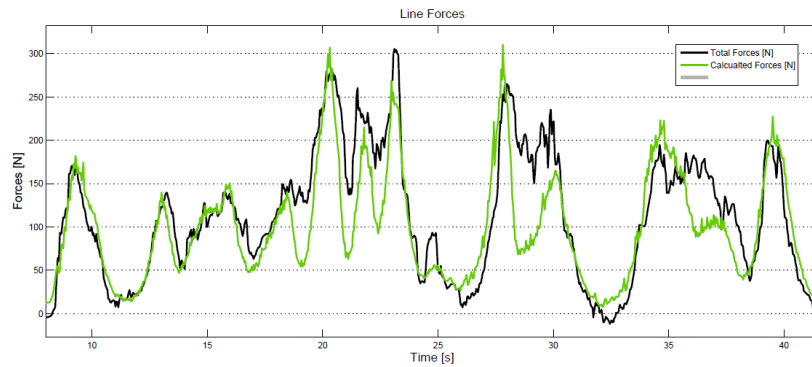


FIGURE 2-33, COMPARISON OF FORCES, WIND SPEED = 6M/S CL = 0,6 AND CD=0.16, WEILENMANN [57]

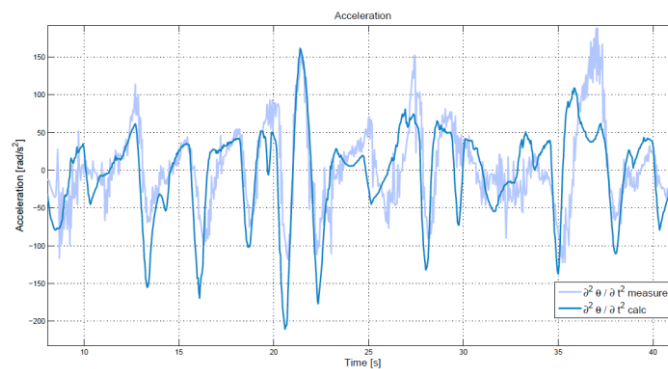


FIGURE 2-34, COMPARISON OF ACCELERATIONS, WIND SPEED = 6M/S CL = 0,6 AND CD=0.16, WEILENMANN [57]

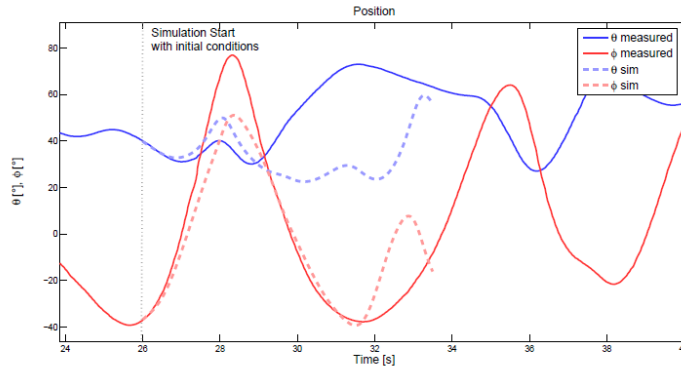


FIGURE 2-35, COMPARISON OF POSITION, WIND SPEED = 6M/S CL = 0,6 AND CD=0.16, WEILENMANN [57]

Breukels chose a different approach for model validation. First the individual components of the multibody model were validated. The cable elements were compared with a pendulum and wave propagation was investigated. The beam elements were compared with a test setup. And the aerodynamic force model was compared with 2d sail data and a 3d wind tunnel test of the kite plane. The cable and beam element proved good agreement with reality however the aerodynamic model showed some discrepancy. Especially the shape proved to be difficult to predict. After all components were validated the complete multibody model was assessed. A steer input was given in reality and in the model from a predefined initial condition after which the forces and velocities were compared. Only 2.5 sec of comparison is shown. There is a general agreement but errors can be found, even in 2,5 sec.

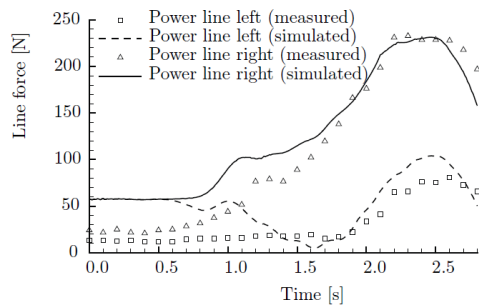


FIGURE 2-36, COMPARISON OF LINE FORCES [46]

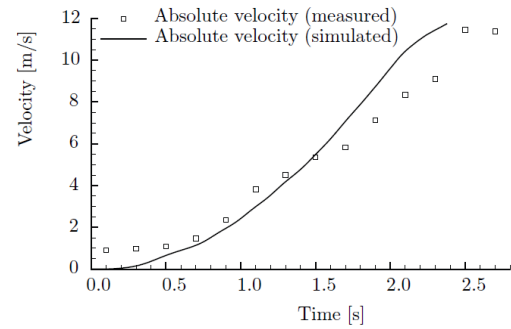


FIGURE 2-37, COMPARISON OF VELOCITY [46]

Several other models are validated by comparing the model to the multibody model of Breukels. Since all states are known in the multibody model the comparison is easier and in general a model could be validated by comparing it to a more advanced model. However the limited validation of the multibody model is questioning this approach.

2.8 TETHER MODELS IN LITERATURE

When simulating a kite power system the tether has to be modelled. There is still some debate about to which extent the cables influence the kite. Nevertheless it is clear that cables become an important factor if the tether becomes longer and thicker [39]. Sweeping a long tether through the air results in drag forces slowing the kite down and also the weight of the tether influences the dynamics. In the various models presented in this literature study different assumptions and modelling choices have been made. This chapter gives a small overview of the different modelling options for the tether.

2.8.1 CONSTRAINT MODEL AND SPRING-DAMPER MODEL

The most simple way to model a tether is by a constraint. The constraint fixes the kite to a certain distance from the ground station. Multiple point mass models use a constraint to model the tether. This approach is computationally cheap to simulate however dynamic effects of the cable mass and sag are neglected. Some models estimate the drag over the tether and add the drag force to the kite. This can be done by estimating the average wind speed and integrating the drag over the tether length.

Alternative to the constraint models the tether could also be modelled as spring damper. In this way the elongation of the tether due to the kite forces is modelled but still the inertia and sag effect of the kite are neglected.

2.8.2 DISCRETISED POINT MASS MODEL

To include the sag and inertia effects of the tether a discretised point mass model was proposed by various authors [59-61]. A discretised point mass model simulates the tether by multiple point masses which are connected by springs. Each point mass represents a section of the tether. The tether drag is simulated by exerting a drag force on all point masses. The drag force is calculated by integrating the drag over the tether segment.

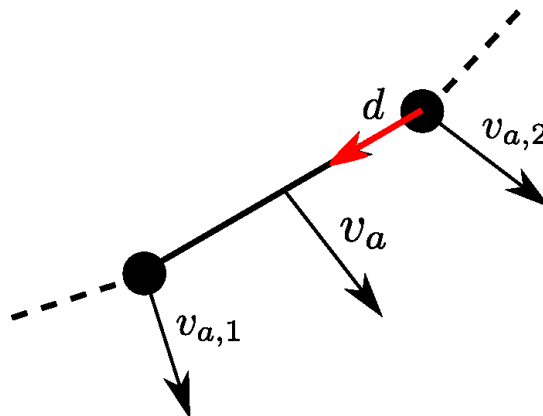


FIGURE 2-38, POINT MASS TETHER MODEL [43]

To simulate the reeling of the cable elements are added or subtracted at the ground. The cable elements could be simulated in two methods. Baayen [43] and Santel [61] simulates the cable elements by spring-dampers. The disadvantage of this approach is that the springs will have a high stiffness which results in a slow simulation. Williams [59] identifies this problem and simulates the elements with constraints instead of spring damper. By this approach the fast tether dynamics are neglected while the slow aerodynamic damping is still included.

2.9 TABLE OF KITE MODELS

Group	Author	Year	Model type	Steering	Aerodynamic forces model	Tether model	Use	Notes	Based on	Verification	Ref
KU Leuven	Diehl	2001	Point mass	Rolling Lift vector	Constant	Constraint	Nonlinear predictive control	No reel-in or out,	-	No	[40, 41]
	Houska	2007	Point mass	Rolling lift vector	Variable $C_L(\alpha)$ and $C_D(\alpha)$, Constant $C_{D,T}$	Spring-damper with drag	Optimal path finding	Control, Test with two kites on one tether. Determination of Betz factors	Diehl	No	[62, 63]
	Houska	2009	Rigid body	Steer input influences aerodynamic force model resulting in a rotating moments	Variable $C_x, C_y, C_z, C_p, C_q, C_r$ (depending on steer input, gravity vector, angle of attack, sideslip angle and rotation rates)	Constraint	-	C++ Program included. Possible to add Jellyfish Oscillations.	Diehl	No	[48]
TU Delft	Ockels	2001	Point mass	No steering,	Constant $C_L, C_D, C_{D,T}$	No	Show of concept	Concept Laddermill	-	Comparison of three models	[10]
	Williams	2006 2007	Point mass	Rolling lift vector	Variable $C_L(\alpha)$ and $C_D(\alpha)$	Point masses	Optimal path finding, control, stability	Also towing case	-	No	[64, 65]
	Williams	2007	Point mass			Inelastic point masses			-	No	[59]
	Williams	2007	Multi-plate	Forces on the plates deform the kite	Variable $C_x(\alpha), C_z(\alpha)$ aerodynamic damping in the form of C_p, C_q, C_r	Spring	Control		-	No, model comparison	[49, 50]
	Williams	2008	Overview, Point, Rigid, Multi-plate,		Point mass-> $C_L(\alpha), C_D(\alpha)$, Rigid body-> C_x, C_y, C_z ,	Constraint	Overview of development	First test data.	-	No	[44]

Group	Author	Year	Model type	Steering	Aerodynamic forces model	Tether model	Use	Notes	Based on	Verification	Ref
	Terink	2009	Semi rigid body	Changing C_L of rudder and elevator	Forces & Moments calculated based on sum of different parts based on local angle of attack.	Constraint	Stability research and control	Smart reduction of DOF, Combination of yaw and roll.	-	Model comparison, Comparison of modes	[16]
	De Groot	2010	Rigid body	Steer input influences aerodynamic force model	Variable C_x, C_y, C_z C_p, C_q, C_r depend on steer input, angle of attack, sideslip angle and rotation rates.	Spring damper	Control			Comparison with model of Breukels, MSC Adams	[45]
	Breukels	2011	Multi-body	Forces on the kite deform the kite	Local lift and drag forces and moment due local angle of attack, wind velocity and position on kite.	Multi-body	Adams Simulation toolbox, prove of cornering, Simulation			Validation of individual components, Comparison of forces and velocity	[46]
	Baayen	2011	Point mass	Applying of a side force (same as rolling lift vector)	Variable $C_L(\alpha), C_D(\alpha), C_S(P_s)$,	Point masses	Control		Diehl	Comparison with model of de Groot	[43, 60]
	Bosch	2012	FEM model	Forces on the kite deform the kite	Local lift and drag forces and moment due local angle of attack, wind velocity.	Constraint	Prove of modelling concept	Aerodynamic force model needs improving	Breukels		
Cranfield University	Hobbs	1986	Point mass		Constant C_L, C_D	Quasi static kite line	Kite study	Theoretic information about CL of kites Line data		No	[66]
Southampton	Dadd Hudson Shenoi	2010	Analytic, Point mass	No steering	Variable $C_L(\alpha), C_D(\alpha)$, $C_{D,T}$	No	Comparison of model with experiments		Welli-come	Yes	[56, 67]

Group	Author	Year	Model type	Steering	Aerodynamic forces model	Tether model	Use	Notes	Based on	Verification	Ref
Sussex University	Furey	2008	Lumped mass	Forces on the kite deform the kite	Lift and drag forces and due local angle of attack and wind velocity.	No	Control			No	[51, 68]
ETH Zurich, Fachhochschule Nordwestschweiz	Weilenmann Tischhauser	2007	Point mass	Rolling lift vector	Variable $C_L(\alpha), C_D(\alpha)$	Spring	Control of kite, Validation	No reel in or out, in appendix an extensive rigid body model.	Diehl	Compare forces, accelerations, steerinput with result	[57]
	Marchand	2011	Point mass	Rolling lift vector	Variable $C_L(\alpha), C_D(\alpha)$	Spring	Assessment of system	Groundstation and state machine included	Diehl	Comparison of power and tetherlength	[69]
Research Institute of Mechanical Engineering, Rusia	Argatov Rautakorpi Silvennoinen	2009	Analytic	-	Constant $C_L, C_D, C_{D,T}$	-	Power estimation	Analytic formula for power estimation	-	No	[35, 36, 38, 39]
Italie Politecnico di torino	Canale, Fagiano Ippolito Milanese	2009	Point mass	Rolling lift vector	Variable $C_L(\alpha), C_D(\alpha), C_{D,T}$ based on CFD analysis	Spring-Damper	Control		Diehl	Yes, Comparison of power	[58] 50]
Universidada Técnica de Lisboa	Carqueija	2010	Point mass	Changing aerodynamic coefficients	C_x, C_y, C_z based on Vortex latex method	Point mass		Good references about cable assumptions, Use look up table based on VLM to get C_x, C_y, C_z		No,	[55, 70]
Norwegian University of Science and Technology	Knappskog	2011	Semi-Rigid Body	Changing aerodynamic coefficients	Variable $C_L(\alpha), C_D(\alpha), C_s(P_s)$ and C_z , depending on angle of attack, steer input and rotation rates.	Constraint	Control	Smart reduction of DOF,		No	[47]

TABLE 5, OVERVIEW MODELS

3 THESIS GOAL AND APPROACH

3.1 GOAL

As stated in the introduction the goal of this thesis report is:

“To develop a real-time kite model which is able to simulate a pumping kite system realistically and is validated”

A simple, real-time kite model is of great interest for multiple reasons. The model shall be used at the ASSET group, for:

- Kite control design
- Performance optimization and evaluation
- Offline system test
- Kite pilot training

From these applications and the literature study the following requirements can be formulated:

- The model should capture the general dynamics of the kite power system.
- The model should run real time. This means that the time to calculate a simulation step is smaller than the simulation step itself. The time needed for a simulation step also depends on the computational power. Therefore a normal desktop computer available at the TU Delft is used as a reference².
- Essential is the validation of the model. The validity of the model should be assessed with the aid of the measurement data.
- The groundstation does not have to be simulated in great detail. Assumed is that the ground station is able to deliver either a certain force or a certain reeling speed.
- Due to the different application the model should be easy to adapt and implemented in a simple and flexible environment.

3.2 APPROACH

In the literature study it is found that multiple models are available. The main flaw of these models is that they are very limited validated. The performance of these models is therefore unknown. To reach the goal of developing a new simple real time model which is validated it would be ineffective to start over again. At the kite power group at the TU Delft there is a 20kW prototype available which has gathered a large amount of measurement data over the past two years. With the data the current models could be evaluated and validated.

This thesis will commence by analysing the available measurement data. An extensive data analysis and system identification will be made. The general forces and moments acting on the kite system are studied for basic understanding and as a first reference for the kite models. Secondly the existing pumping kite models will be evaluated based on the literature study and the data analysis and system identification. Besides the kite models also the different tether model will be evaluated. Finally the model is developed and compared with measurement data as validation.

² Intel Duo Core processor E4400 (@2.00 GHZ) and 2GB RA.M

4 REFERENCE FRAMES AND DEFINITIONS

A reference frame defines the position and orientation of a point, body, force or moment in space. In this section the reference frames used in this theses are defined. In this thesis the reference frames defined by Jehle [71] will be used. These frames are currently the standard at the ASSET kite group. Addition frames are added for modelling. The following reference frames will be used:

4.1 TABLE OF REFERENCE FRAMES

Reference frames	Abbrev.	Origin	Definition X	Definition Y	Definition Z
Earth-Xsens frame	EX	Tether exit point $\mathbf{0}$	North	(East)	\perp to ground
Earth-Groundstation frame	EG	Tether exit point $\mathbf{0}$	$+\mathbf{x}_{EX}$	$(-\mathbf{y}_{EX} = \text{West})$	$-\mathbf{z}_{EX}$
Wind frame	W	Tether exit point $\mathbf{0}$	Downwind	(\otimes)	$+\mathbf{z}_{EG}$
Small Earth frame	SE	$\mathbf{P} \in M$	(Small-North)	$\mathbf{z}_w \times \mathbf{p}^{0P}$	$-\mathbf{p}^{0P}$
Kite sensor	KS	IMU	Main strut	Left to right wingtip	(\otimes)
Kite frame	K	Kite \mathbf{CG}	Main chord line	Left to right wingtip	(\otimes)
Local frame	L	Kite \mathbf{CG}	(Small-North)	$\mathbf{z}_w \times \mathbf{p}^{0P}$	$-\mathbf{p}^{0P}$
Local tether	LT	Kite \mathbf{CG}	$\mathbf{x}_{LT} = \mathbf{z}_{LT} \times \mathbf{y}_{LT}$	$\mathbf{y}_{LT} = \mathbf{z}_{LT} \times \mathbf{z}_{EG}$	$\mathbf{p}^{m_1 m_2}$
Body frame	B	Kite \mathbf{CG}	Symmetry plane \mathbf{xz}_B	(\otimes)	$-\mathbf{p}^{0P}$
Apparent Wind frame	AW	Kite \mathbf{CG}	\mathbf{v}_{app}	(\otimes)	Symmetry plane \mathbf{xz}_B

TABLE 6, ORIGINS AND DEFINITIONS OF REFERENCE FRAMES

See Appendix C: for an overview of all reference frames. In Appendix D: the rotation matrices are stated and Appendix E: contains a small Matlab program to plot all reference frames. Figure 4-1 and Figure 4-2 show the frames.

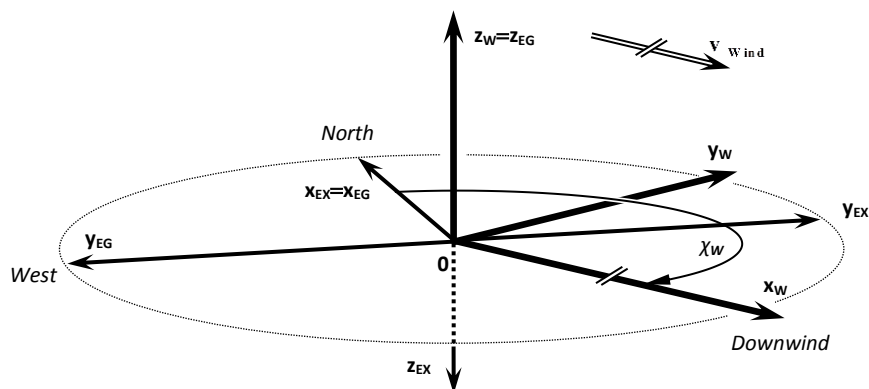


FIGURE 4-1, ILLUSTRATION OF THE THREE REFERENCE FRAMES EX, EG AND W

4.2 EARTH FIXED FRAMES

Two earth fixed reference frames are used. The EX and EG frame. Both frames have their origin at the tether exit point and their x axis in direction of North. In the EX frame the z axis is pointed in the ground and the EG frame has its z axis up. So all axis are parallel only the direction differs. The EX frame is defined according to the standard Earth fixed frame used in avionics and is a local North, East, Down (NED) coordinates system. When calculating Euler angles the EX frame is used. The EX frame is also used as a inertial frame of reference. The influence of the rotating earth is neglected in this thesis. The EG frame is mainly used as an intermediate step to the wind reference frame W . The W frame is defined by rotating EG frame around the z_{EG} axis.

4.3 KITE FIXED REFERENCE FRAMES

The kite frame K is used to describe the orientation of the kite. The x axis is along the main chord line and points forward. The y axis points from the left to right wingtip and the z axis is pointing down. The small earth frame SE is used as 'intermediate' reference frame between the earth frames and the kite frame. The small earth frame is the tangential frame to a unit sphere with the x axis pointing north and z axis pointing to the origin of the sphere and is used to calculate the azimuth and elevation angles and is used for control. Additionally two extra reference frames are used for modelling. A local frame L and the body frame B . Both are displayed in Figure 6-2. The local frame L is identical to the small earth frame SE only the origin lies at the CG of the kite. Finally a body reference frame is used for kite modelling. The body frame originated from the assumption that the kite is constraint in two directions and is defined by rotating the local frame L around its z axis.

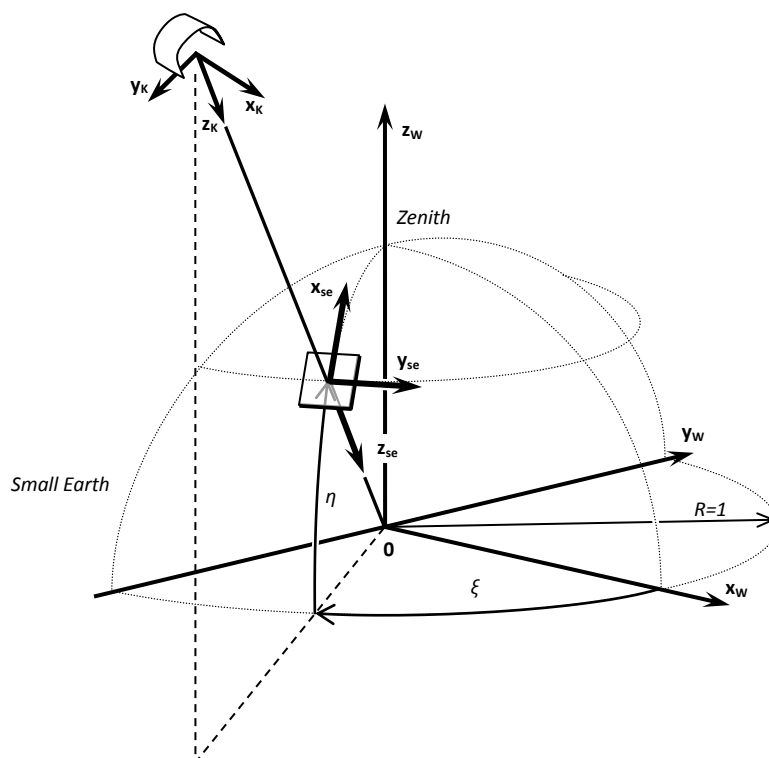


FIGURE 4-2, REFERENCE FRAMES W, K AND SE [71]

4.4 STEERING AND POWER VALUES

The position of the steering and power motors in the control pod are measured by analogue potentiometers. Since the neutral position of these motors differs from test to test the readings have to be converted to comparable standard. The output is a value between 0 and 4095. The absolute values P^{abs} are converted into a relative steering/power-values with a range of $\pm 100\%$ resp. 0–100% as follows:

$$P_S(P_S^{abs}) = \left(2 \cdot \frac{P_S^{abs} - P_S^{\min}}{P_S^{\max} - P_S^{\min}} - 1 \right) \cdot 100\% \quad (4-1)$$

for the steering value and

$$P_P(P_P^{abs}) = \left(\frac{P_P^{abs} - P_P^{\min}}{P_P^{\max} - P_P^{\min}} \right) \cdot 100\% \quad (4-2)$$

for the relative power setting, respectively. The relative power setting is defined from 0–100%, as there is no neutral position. 0% power setting would result in a fully depowered, slack kite, while 100% represent the highest possible angle of attack. P^{\max} (P^{\min}) refer to the maximal (minimal) potentiometer values from the ADC (nominally 4095 resp. 0).

5 DATA ANALYSIS AND SYSTEM IDENTIFICATION

To get a better understanding of the system first a general data analysis is performed. The data analysis consists of multiple parts. First the trajectory and velocities of the kite are shown after which the general forces and moments on the system during generation and retraction phase are studied. With the forces known the general performance of the kite power system can be evaluated. Secondly the orientation of the kite is studied. Especially the straight tether assumption is studied and the relation between steering and orientation. Thirdly the wind shear model is evaluated and the apparent wind speed is investigated. Finally the aerodynamic performance of the kite is studied.

5.1 DATA SELECTION

The wind speed and the trajectory has a big influence on the performance and characteristic of the system. Therefore six data sets have been selected from six different test days with different wind speeds. During test days a variety of tests are performed. In this thesis it was chosen to only select parts of the day with continuous power cycles, ideally flown with an autopilot. The autopilot used is the '2Lap' autopilot developed by Jehle [71]. For comparison also one data set of the Hydra kite is displayed. Due to the large amount of data the data analysis only shows the results of the most illustrative dataset. With the developed software tools (see section 5.11) the additional data can be examined.

Data set	Date	Kite	Wind speed [m/s]	Time [min]	Number of cycles	Control with autopilot	Pitot available	Velocity correct	Trimble GPS	Weight Kite [kg]
1	22-5-2012	Mutiny	2.8	22	12	Yes	No	Yes	Yes	25
2	20-1-2011	Mutiny	4.4	26	11	No	No	Yes	No	21
3	22-9-2011	Mutiny	6.6	42	25	No	Yes	No	No	21
4	31-5-2012	Mutiny	7.4	26	20	Yes	Yes (not calibrated)	Yes	Yes	25
5	23-6-2011	Mutiny	8.0	31	20	No	Yes	No	No	21
6	23-6-2012	Hydra	10	29	15	Yes	No	Yes	Yes	18

TABLE 7, SELECTED DATASETS

5.2 POSITIONS AND VELOCITIES

Currently a figure of eight pattern is flown during the generation phase. This pattern has the advantage that both turns are downward. A kite will turn much faster downward then upwards because the gravity force will accelerate the kite during the turn. In addition the tether is not wound. The figure of 8 pattern results in a fairly constant tether tension. Other patterns are possible and optimized trajectories are studied. The figure of 8 trajectory is defined by three parameters (see Figure 5-1). During the datasets the following parameters are used in general $A_\eta = 10^\circ$, $A_\xi = 10^\circ$ and $\eta_0 = 25^\circ$.

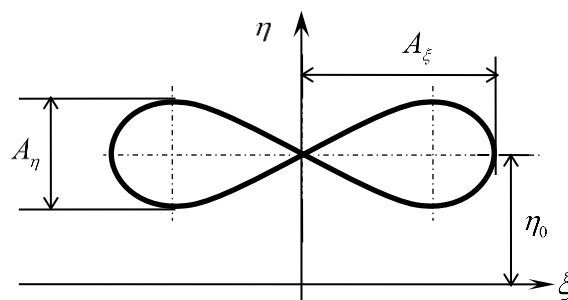


FIGURE 5-1, PARAMETERS FIGURE 8

In reality the path is not perfectly tracked and the kite is 'parked' at zenith position during the retraction phase. The trajectory of the kite during a cycles is shown in Figure 5-2 and in Figure 5-3 the kite velocities during these cycles is shown in Figure 5-4.

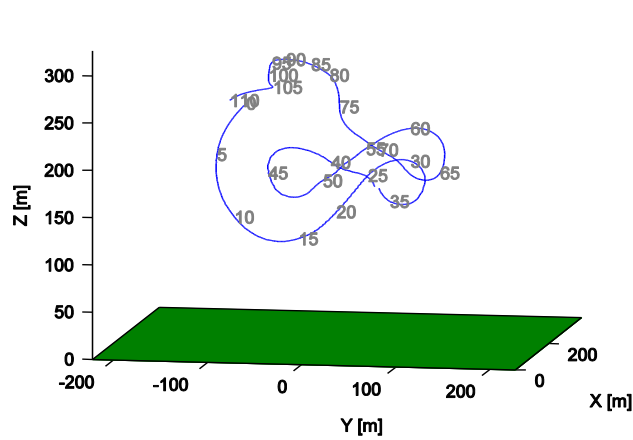


FIGURE 5-2, FRONT VIEW OF PATH FLOWN

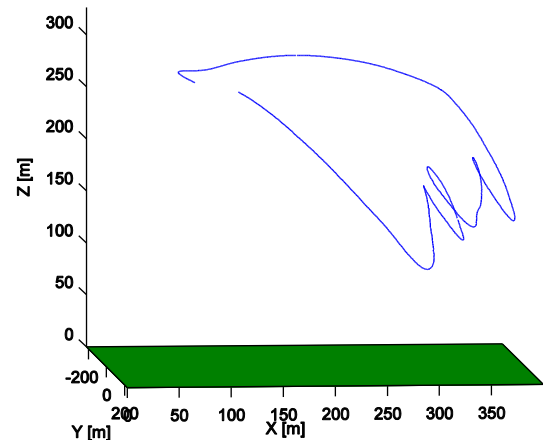


FIGURE 5-3, SIDE VIEW OF PATH FLOWN

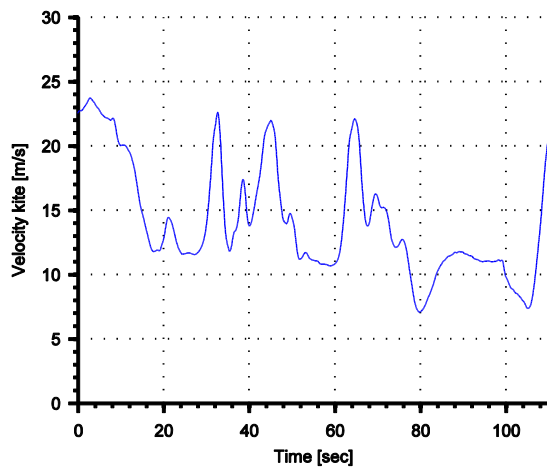


FIGURE 5-4, VELOCITY OF KITE, DATASET 1

In the velocity plot of the kite, Figure 5-4, the effect of the outer downward turns on the velocity is easily seen at sec 32, 45 and 64. During the turns the velocity increases due to gravitational forces.

5.3 FORCES

At the kite three forces are acting. The aerodynamic forces, the tether force and the gravitational force. For basic understanding the magnitudes of these forces are determined and plotted during 15 min of flight. The forces are determined based on a force equilibrium which is possible since the acceleration of the kite is measured. This force equilibrium requires that all three force vectors are determined in the kite reference frame K .

The tether forces F_{Tether} is measured at the groundstation. The force is expressed in the kite reference frame by:

$$\mathbf{F}_{Tether} = F_{Tether, Measured} \mathbf{p}^{0P} \quad (5-1)$$

As a result the tether force is along the vector \mathbf{p}^{0P} which is the vector from the groundstation to the kite. Note that a straight tether is assumed, this assumption is further explored in 5.5.

The gravitational forces \mathbf{F}_{Gra} is calculated with:

$$\mathbf{F}_{\text{Gra}} = m_{\text{kite}} \mathbf{g} \quad (5-2)$$

Now Newton's 2nd Law states:

$$m_{\text{kite}} (\mathbf{a})_K = (\mathbf{F}_{\text{Aer}})_K + (\mathbf{F}_{\text{Tether}})_K + (\mathbf{F}_{\text{Gra}})_K \quad (5-3)$$

The acceleration is measured by the X-Sens sensor at the kite. Which leaves only the aerodynamic force \mathbf{F}_{Aer} as unknown.

In Figure 5-5 the forces are plotted during 15 min of flight. The flight consist out of regular 'figure of 8' flight during the generation phase and parking at zenith during the retraction phase. The effect of the inertia of the kite, the $m_{\text{kite}} (\mathbf{a})_K$ term, is also plotted.

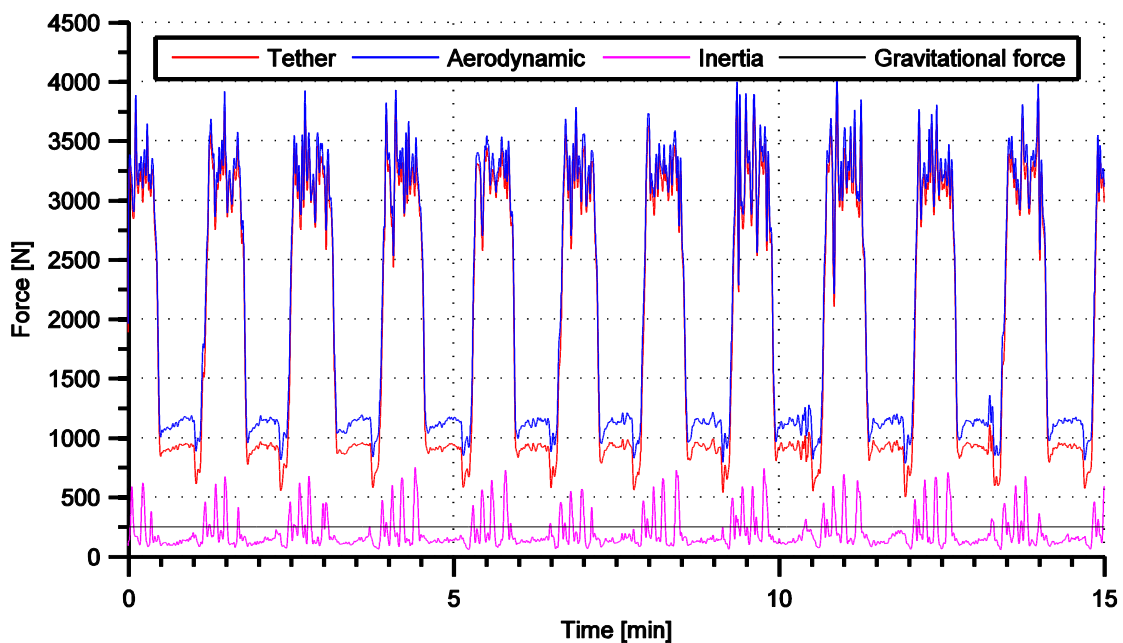


FIGURE 5-5, FORCES DURING POWER CYCLES, DATASET 4

From the plot can be seen that the inertia and weight forces of the kite are relatively small (<10% of total forces) during the generation phase. The tether force is almost equal to the aerodynamic force. During the retraction phase the forces become smaller and the inertia and weight forces play a more important role in the dynamics of the system. Further can be seen that the groundstation is currently force controlled. The winch controller tries to have a constant force in the tether. The force is currently set around 3000N to 4000N because higher loads will damage the ground station or the kite. When the forces become too high the reeling out speed is increased which results in a lower apparent wind speed and forces. Due to this force constraint the system is currently not running at the theoretical optimized reeling speed for power production.

To investigate the forces in the kite reference frame the accelerations in the kite frame are shown in Figure 5-6 during four cycles. The grey background indicates the generation phase while the white background indicates the retraction phase.

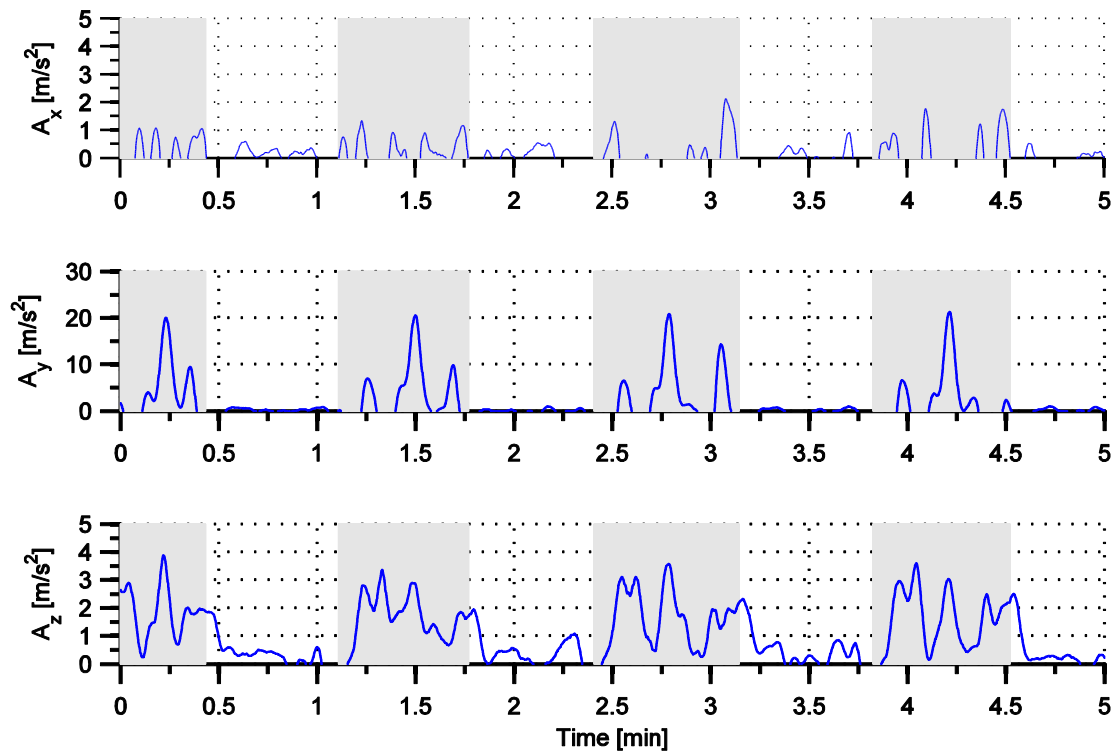


FIGURE 5-6, ACCELERATIONS IN KITE REFERENCE FRAME, DATASET 4

It can be seen that almost all accelerations are in the \mathbf{y}_K direction. This is explained by realizing that the kite is constrained by the tether in \mathbf{z}_K direction. The accelerations in \mathbf{z}_K direction are mainly due to the changes in the reeling speed which are fairly smooth. The accelerations in \mathbf{x}_K direction are also fairly constant. Apparently the kite is flying with a relatively constant speed and effects of changing wind (for instance turbulence) does not have a large influence on the acceleration of the kite. The main accelerations are in \mathbf{y}_K direction due to the steering of the kite. The kite fly's a figure eight pattern in the air, the curved trajectory results in relative large centrifugal accelerations. The acceleration measured in the \mathbf{y}_K direction are directly linked to the speed and radius of the curve. Currently the figure of eight has a radius of around 50m, together with the velocities of 25m/s this results in accelerations in the order of 0 to 3G with local peaks of 5G. During the retraction phase the accelerations are much smaller.

5.4 POWER, ENERGY AND REELING SPEED

With the forces known the general performance of the kite power system can be evaluated. Main parameters are the power and the energy production. On the next page the power, energy production and reeling speeds are plotted over time for one dataset (Figure 5-7). The reeling speeds are shown since they show the effect of the force controlled groundstation and give an indication of the reeling speeds.

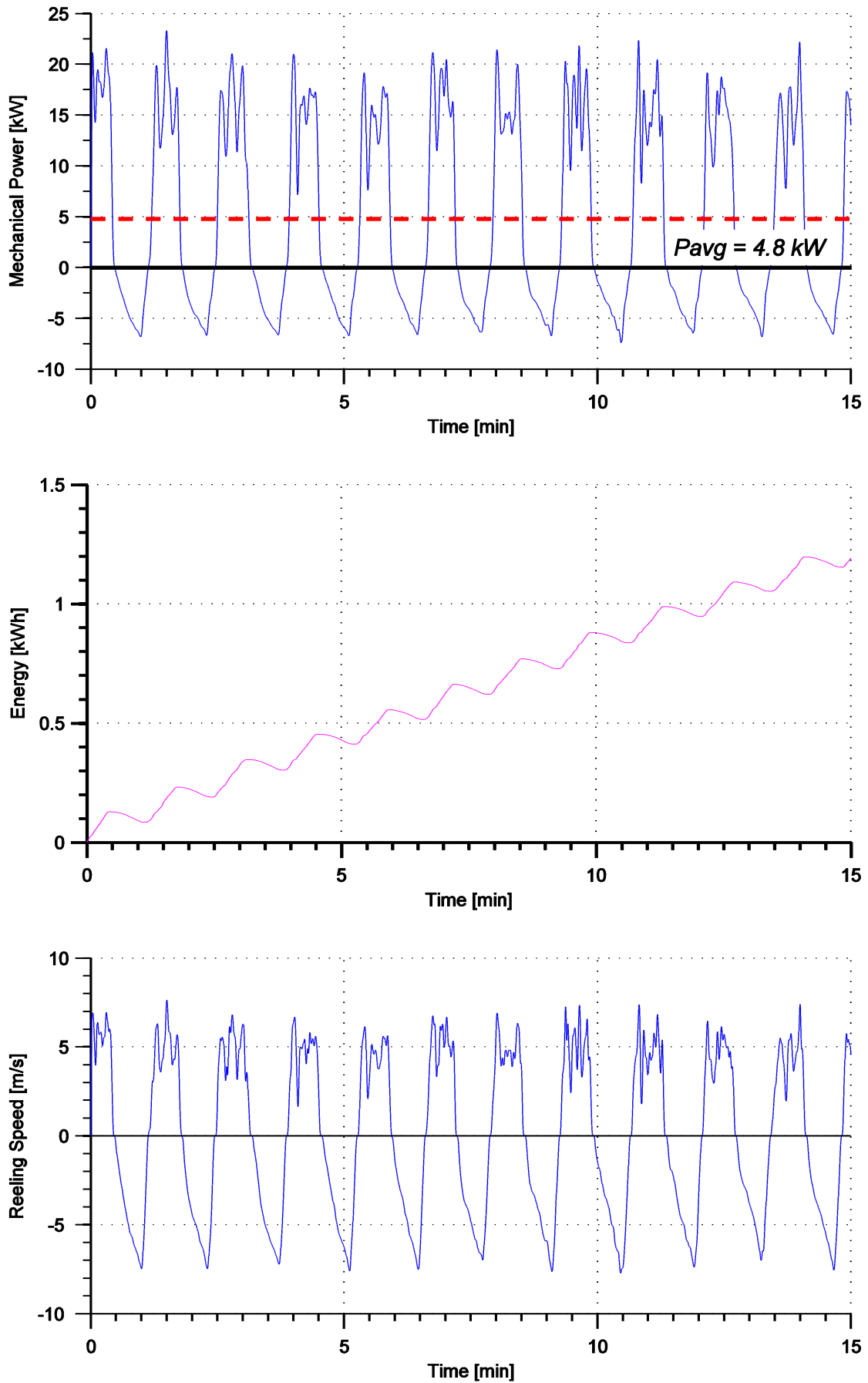


FIGURE 5-7, POWER, ENERGY AND REELING SPEED, DATASET 4

In Figure 5-7 the general appearance of the power, energy production and reeling speeds is shown. During these cycles an average power of 4.8kW is produced. During the generation phase the power is a factor 2 to 3 higher. The reeling speed is fluctuating during the generation phase. This is, as stated before, due to the force control of the winch which limits the force to 3000-4000N. Table 8 shows the key numbers of this and the other datasets (see Table 7 for overview of the datasets).

Dataset	Wind speed (at 6 m height) [m/s]	Average power [kW]	Average cycle time [min]	Average reeling-out speed [m/s]	Average reeling-in speed [m/s]	Average power generation phase [kW]	Average power retraction phase [kW]
1	2.8	1.79	1.83	1.66	4.01	4.06	2.81
2	4.4	2.37	2.60	2.07	3.75	5.46	2.33
3	6.6	4.44	1.68	3.62	4.22	11.3	3.10
4	7.4	4.80	1.40	4.30	4.77	15.1	3.84
5	8.0	5.19	1.55	4.24	5.57	14.1	5.90
6 (hydra)	10	5.75	1.93	4.20	5.46	13.8	4.07

TABLE 8, AVERAGE PERFORMANCE DATA

In the table is shown that the average power increases with wind up to a certain limit. Further it is noticed that the reel in speed remains fairly constant while the reel out speed increases with increasing wind. This is due to the force limit of the system. With higher wind speeds the winch reels out faster in order to decrease the apparent wind and, as a result, the force. During the retraction phase the tether force is controlled in such a manner to keep a minimal tension over the tether. Currently this minimal value is set at 800-1000N to guarantee controllability over the kite.

It should be noticed that the cycles of the different datasets are flown with different settings of the autopilot and winch controller. Also the wind profiles differ from day to day. As a result the data of Table 8 should be analysed with care. Nevertheless it gives an indication of the current capabilities of the system

5.5 ORIENTATION OF THE KITE RELATIVE TO THE TETHER

In kite models generally assumptions are made for the orientation of the kite. Multiple models assume the kite to be constraint in two directions and leave only the rotate around the tether as degree of freedom. Additional multiple models assume the tether to be straight. Since the position and orientation of the kite are measured in the prototype these assumptions could be investigated by plotting the angles $\omega^{SE,K}$ between the SE and K reference frame. The angle $\phi^{SE,K}$ can be seen as the roll relative to the tether and $\theta^{SE,K}$ as the pitch relative to the tether. When an angle is measured the cause could be twofold. Or the tether is sagged or the kite is rotating relative to the tether end point.

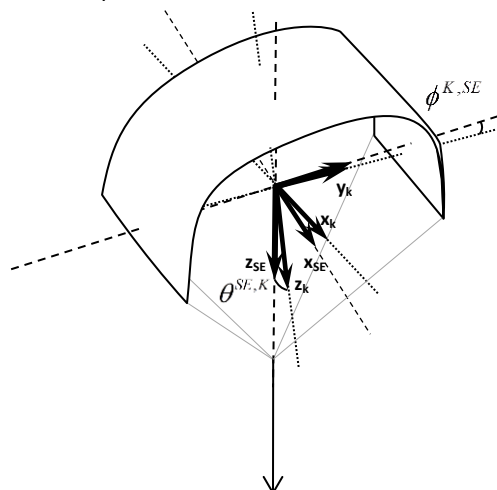


FIGURE 5-8, REFERENCE FRAMES SE AND K

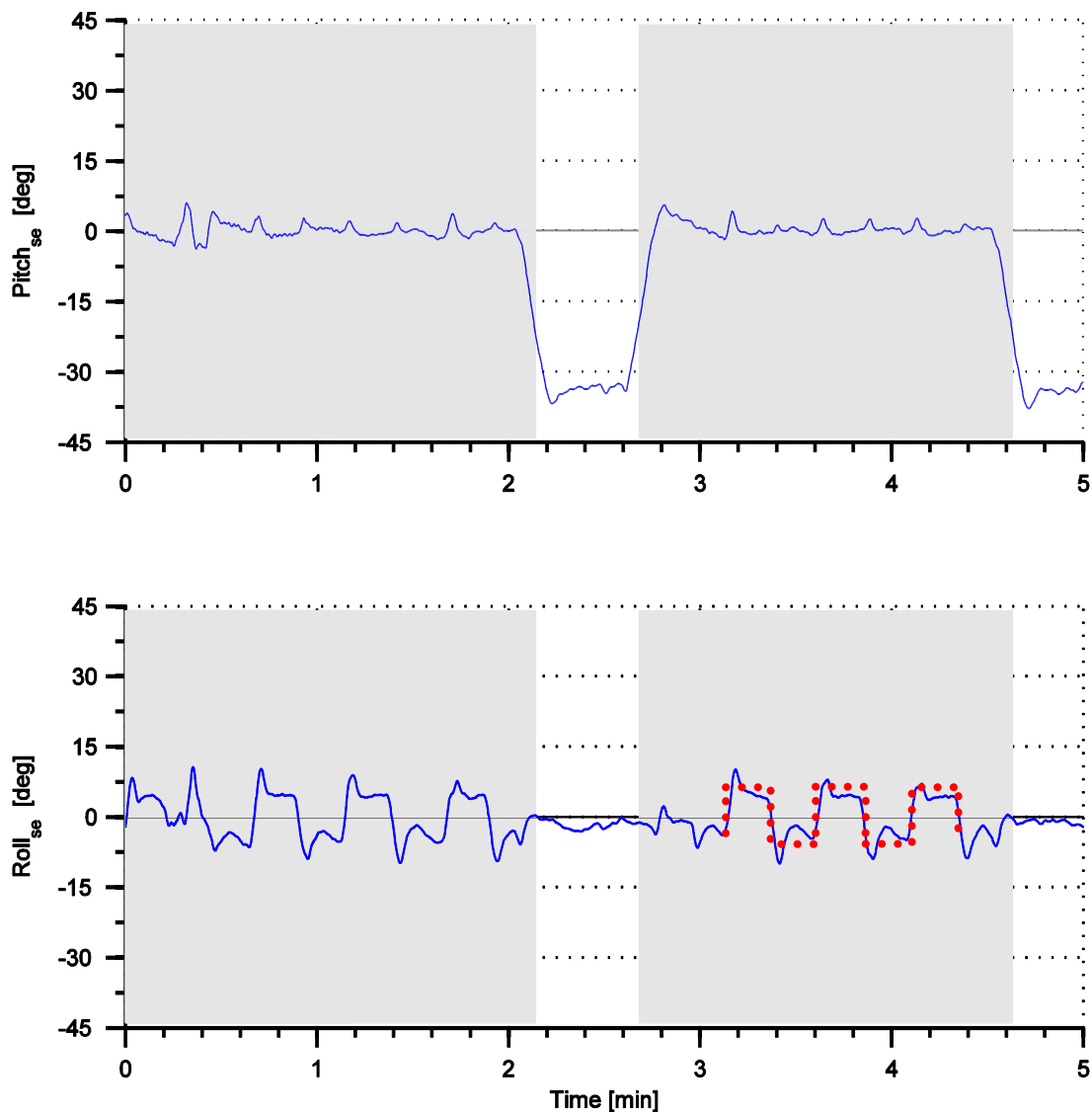
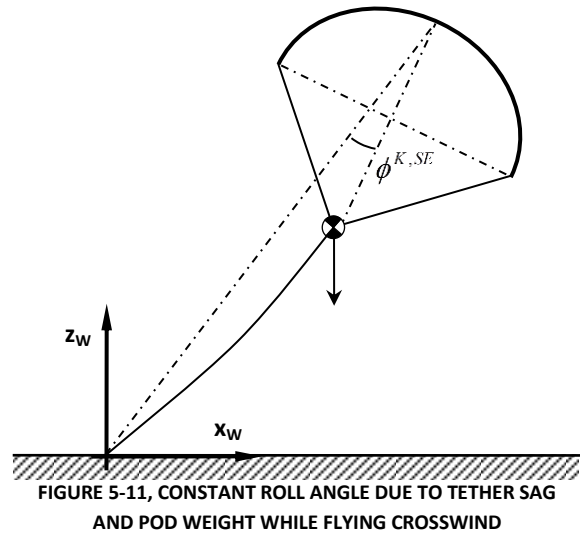
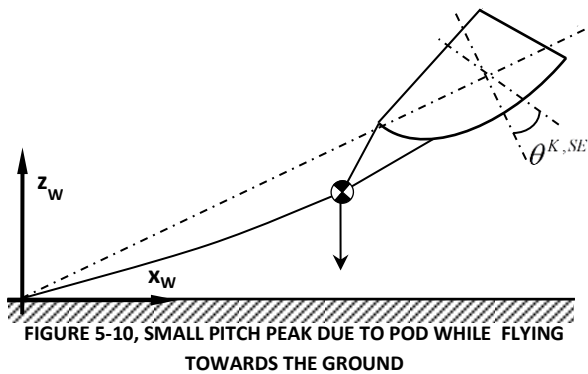


FIGURE 5-9, 'PITCH AND ROLL' ANGLES BETWEEN SE AND K FRAME, DATA 14-6-2012, AVERAGE WIND = 3.9 M/S

In Figure 5-9 the angles are plotted. The pitch angle clearly shows the effect of the bridle, during the retraction phase (white background) the kite is depowered. From the data it is seen that the kite is rotated approximately 35 degrees. This pitch angle decreases the angle of attack of the kite and consequently the lift coefficient. Further the pitch angle is fairly constant. A small periodic pattern can be seen. Around 3 or 4 times during one generation phase the pitch angle has a small peak of approximately 7 degrees. In the roll angle the same peaks could be seen. However after a peak the sign of the angle changes, creating a square wave pattern (see the red dots in Figure 5-9). In video analysis of the test flight it is seen that the cause is due to the pod and tether dynamics. These small peaks align perfectly with the outer turns of the figure eight. During the outer turn the kite flies downwards for a short time. Normally the kite is pulling the pod and tether along however during the outer turns the pod is suddenly free to accelerate in the direction of the ground and pulls the kite for a short time. During this time the pitch of the kite relative to the tether is shortly increased (see Figure 5-10). The square wave pattern in the roll angle is explained by the weight of the pod and the cable sag. Depending on the direction the kite is always 'rolled' inwards (see Figure 5-11).



Overall the effects described are fairly small. During the generation phase the pitch angle varies only 5 degrees and the roll angle has peaks up to 15 degrees after a turn but most of the time the angles are between -7.5 and 7.5 degrees.

To explore the influence of stronger wind and to study the pod dynamics more up close the angles are shown from a date with higher winds speeds and where uploops and downloops were flown in succession.

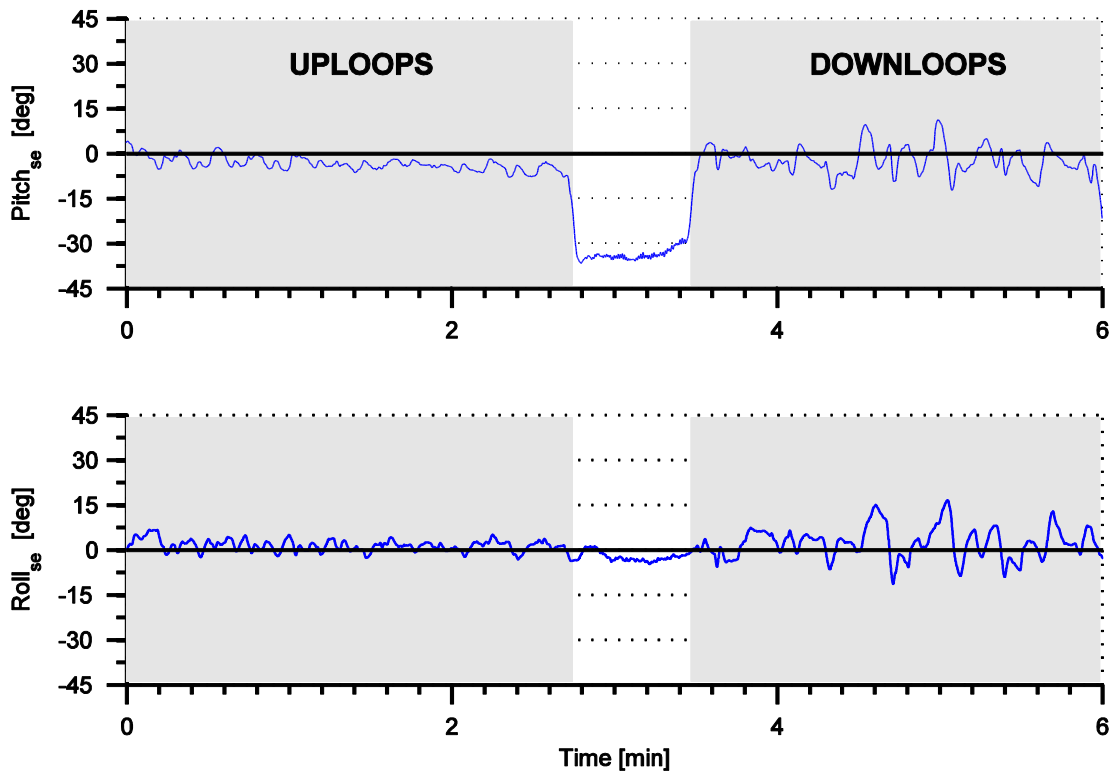


FIGURE 5-12, 'PITCH AND ROLL' ANGLES BETWEEN SE AND K FRAME, 23-6-2012, AVG. WIND = 9.4 M/S, WITH HYDRA KITE

As expected a clear difference is seen between uploops and downloops. During downloops large pitch and roll peaks are found due to the pod which is falling to the ground in the outer turns. When uploops are flown the pod is dragged along and no peaks are found. Further an interesting decreasing trend is found in the uploop pitch angle. This is clearly the effect of cable sag, a longer cable result in a smaller pitch angle. The angles measured are all quite small and stay within 15 degrees. It should be noticed that the X-Sens Mti-G sensor is

used to determine the orientation of the kite. During high wind conditions the X-Sens Mti-G sensor seems to produce faulty position data (see section 5.9). The repeating patterns indicate a correct measurement of the angles however this is not checked.

Summarising the following is found: based on the measurements the assumption that the kite is constraint in two rotational directions is largely valid. Only small angles of the kite relative to the tether were found. The angles which are measured are most likely due to tether sag en pod dynamics. Both effects will have a small effect on the overall performance. When simulating a kite system especially the effect of the pod is possibly worth taking into account.

5.6 STEERING OF THE KITE

In the previous paragraph it was noticed that the kite is largely constrained in $\phi^{K,SE}$ and $\theta^{K,SE}$ direction. This leaves one orientation, the rotation around the tether determined by $\psi^{K,SE}$. This angle determines the direction of the kite. For the system identification the relation between the rotation around the tether and the steer input was of great interest. The kite steers due to the changing aerodynamic forces. Since a steer input, via a change in line length, affects the aerodynamic forces it is expected that there is a relation between the steer input and the rotational acceleration. However during the system identification the rotation rates $\omega^{EX,K}$, measured by the IMU sensor in the kite, were plotted against the steer input during the generation phase:

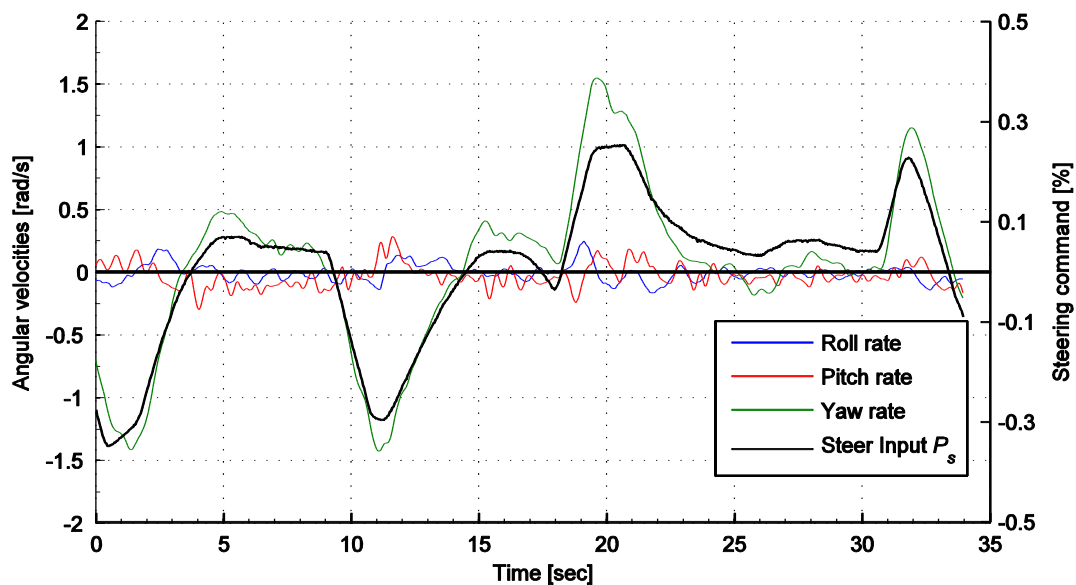


FIGURE 5-13, ANGULAR VELOCITIES VS. STEERING COMMAND DURING GENERATION PHASE

Figure 5-13 shows the rotation rates together with the steer input. From the figure a clear relation became clear between the steer input and the yaw rate r while the pitch and roll rates q and p remain almost zero. This is remarkable since it was expected that the rate *acceleration* are proportionally depending on aerodynamic forces and moments introduced by a steering input. The found relation between yaw rate r and steer input is not fully linear as at higher steering deflections the rates increase disproportionately. In addition, especially in wide cross-wind manoeuvres a bias of the steering setting off zero can be observed. That is, even though no yaw rate is measured (the kite is flying straight), there is a non-zero steering input present. During the retraction phase a similar relation is found however the steer inputs are much larger.

5.6.1 MOMENT EQUILIBRIUM DURING STEERING

To investigate the relation between the yaw rate and steer input and to explain the non-linearity the forces in xy_k plane during a steer input were drawn.

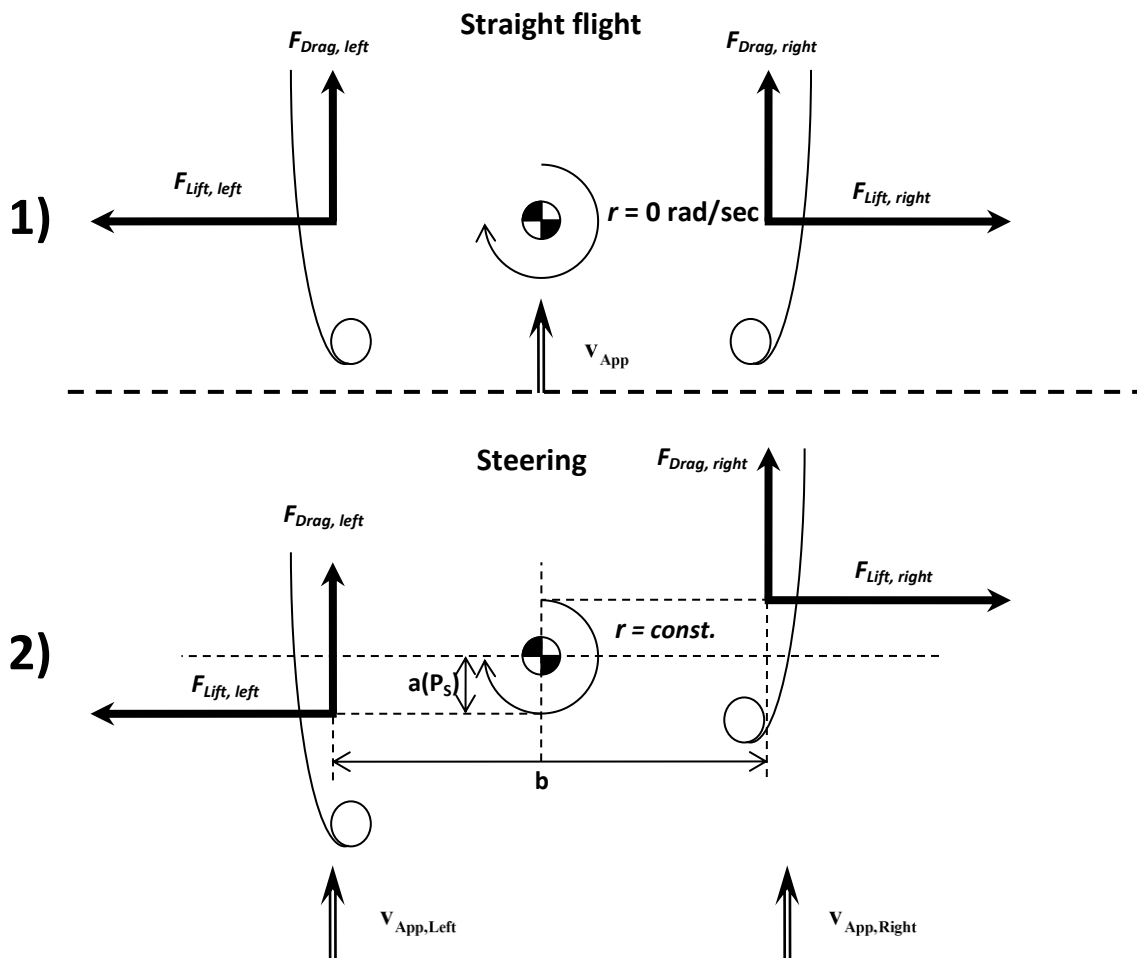


FIGURE 5-14, FORCES DURING STEERING

Figure 5-14 shows the moments acting on a kite. In straight flight the lift forces and drag forces on both wingtip are equal and cancel each other out. As a result no moment or rotations are found. When starting a turn around the left wingtip (left in the front view of the kite) the line attached to the back of the left wingtip is pulled. As a result the left wingtip moves forward relative to the other. This is simply because the kite is flexible and the shorter line length results in a different equilibrium position of the kite. The difference in the position of the wingtip during cornering has also been found in the models of Breukels [46] and Bosch [53] and can be seen in flight videos. Additional to the movement also the angles of attack change at the wingtips due to the steer input. The left wingtip gets a higher angle of attack due to the increased line tension on the back line. As a result the lift force will increase. The opposite holds for the right wingtip. This effect is not taken into account in the estimation below but is found in the models of Breukels [46] and Bosch [53].

The difference in position and lift force relative to the center of gravity of the kite now results in a moment which causes a rotational acceleration. To study the phenomena an estimation of the moments is made:

$$\sum M = I\alpha$$

$$\sum M = a(P_s)F_{Lift, left} + a(P_s)F_{Lift, right} + \frac{1}{2}bF_{Drag, left} - \frac{1}{2}bF_{Drag, right} = \mathcal{Y}\dot{\alpha} \quad (5-4)$$

The inertia term, $I\alpha$, can be neglected since it is much smaller than the moments acting on the kite. For the present kite, the Mutiny V2 kite, the inertia tensor, I , around the \mathbf{z}_k has a value of $63,64 \text{ kg/m}^3$ and maximum rotational accelerations of 4 rad/s are measured. This would result in a maximum inertia moment of $\pm 240 \text{ Nm}$ which is negligible compared with the aerodynamic force moments which are in the order of $1000\text{--}2000 \text{ Nm}$. By neglecting the inertia term this simple estimation is performed on a quasi-static basis. The distance $a(P_s)$ is a function of the steer input. In this analysis a linear relation is assumed between steer input and the distance.

The lift and drag forces are calculated with the following formulas. Note that the apparent wind speed has to be corrected for the rotation speed of the kite.

$$\begin{aligned} F_{Lift,Left} &= \frac{\rho_{air} A_{side} C_L}{2} v_{App,Left}^2 \\ F_{Drag,Left} &= \frac{\rho_{air} A_{side} C_D}{2} v_{App,Left}^2 \\ v_{App,Left} &= v_{App} - \frac{1}{2} br \\ v_{App,Right} &= v_{App} + \frac{1}{2} br \end{aligned} \quad (5-5)$$

This results in the following formula:

$$\sum M = 2a(P_s) \frac{\rho_{air} A_{side} C_L}{2} \left(v_{App}^2 + \left(\frac{1}{2} br \right)^2 \right) - 2 \frac{1}{2} b \frac{\rho_{air} A_{side} C_D}{2} (br v_{App}) = 0 \quad (5-6)$$

The measured rotational rate is shown in Figure 5-13 and is between -1.5 and 1.5 rad/sec . The span b of the Mutiny V2 kite is 7.0 m and as a result term $\left(\frac{1}{2} br \right)^2$ (order 0-30) can be neglected compared to the v_{App}^2 (order 400-500). After simplification this results in the following formula for the yaw rate r .

$$r \approx \frac{2}{b^2} \frac{C_L}{C_D} a(P_s) v_{App} \quad (5-7)$$

This formula shows several important findings. First of all it explains why the steer input is linked to the rotation rates instead of the rotation acceleration and secondary it shows that the rotation rate will almost certainly depend on the apparent wind speed. Before looking at all consequences of this formula first the influence of side slip and gravity is studied and the formula is checked with the test data.

5.6.2 EFFECT OF SIDE SLIP AND GRAVITY

To study the effect of gravity on the flight a kite is pictured which is flying crosswind. The gravity force is now acting in $-y_k$ direction.

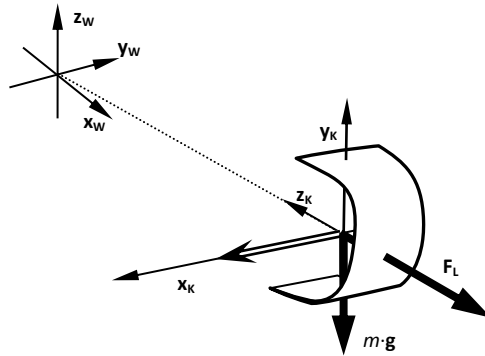


FIGURE 5-15, KITE FLYING CROSSWIND

Figure 5-16 shows the forces acting in the xy_k plane. The gravity vector shown in the drawing is the gravity vector projected on the xy_k plane. The forces acting on the kite in the left figure are not in equilibrium and due to the gravitational force the kite will start to accelerate down resulting in a velocity in $-y_k$ direction. This lateral movement is called side slip since the kite is not flying in the direction it faces. As a consequence of the velocity in $-y_k$ direction the apparent wind will turn in respect to the kite with an angle β .

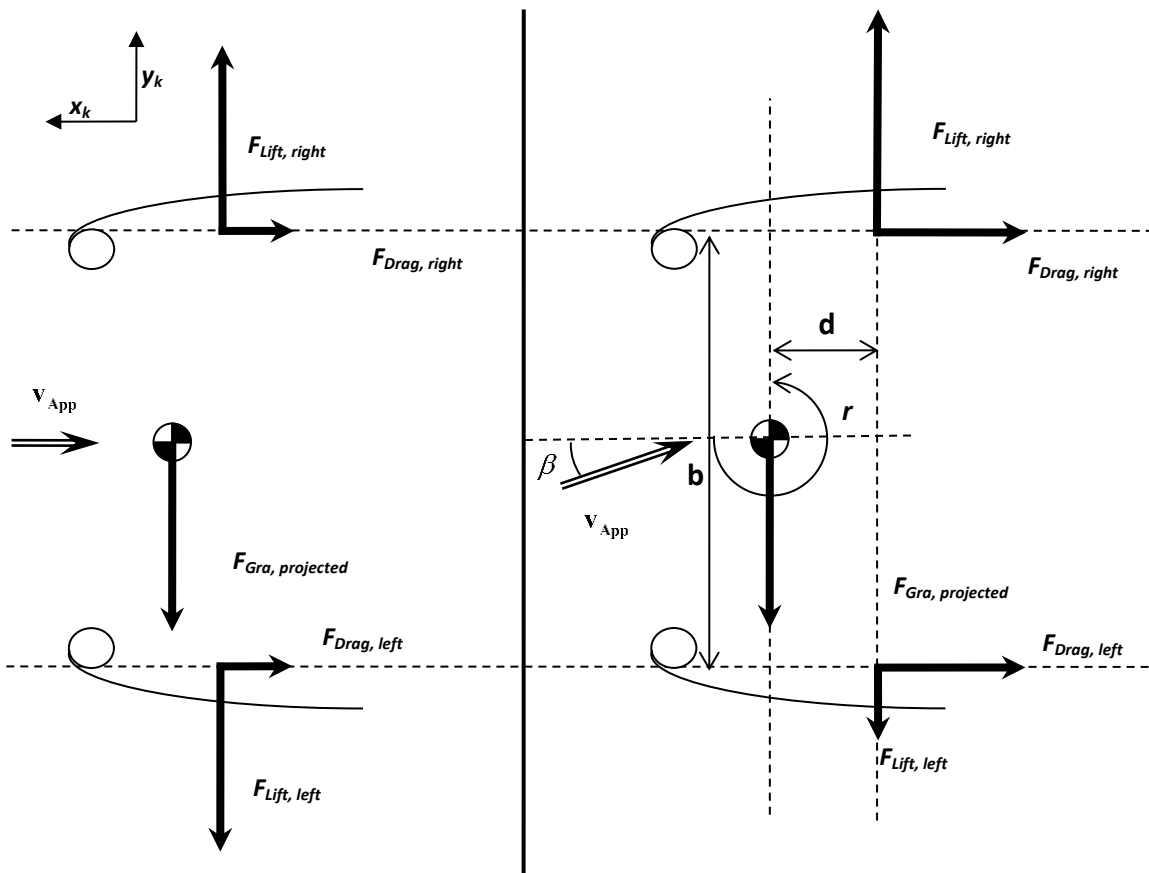


FIGURE 5-16, ROTATION DUE TO THE WEIGHT OF THE KITE

Due to the change in apparent wind speed both wingtips now have a different angle of attack. The angle of attack increases on the right wingtip while it decreases on the left. Since the lift force increases with the angle of attack the situation on the right of Figure 5-16 is attained. In the drawing is shown how the change in lift force counteract the gravitational forces due to the difference in angle β . Since there is a difference in lift force a rotating moment is formed which causes an angular acceleration of the kite in the direction of the apparent wind. This angular acceleration is damped by the difference in airspeed on the left and right wingtip previously described in section 5.6.1 and a constant rotation rate is established. Currently there is no relation available describing the lift coefficient of the kite wingtips depending on the angle of attack. Therefore only the phenomena is described. Summarizing a side slip angle results in a rotation of the kite in the direction of the apparent wind. The gravity force on the kite results in such a side slip angle when the kite is flying crosswind.

5.6.3 DATA FIT OF ROTATION RATE

Based on the analysis described above the following relation for the yaw rate r based on the steer input and orientation was proposed.

$$r(P_S) = c_1 v_{App} P_S + c_2 \cos(\angle\{\mathbf{g}, \mathbf{y}_K\}) \quad (5-8)$$

The term $\cos(\cdot)$ takes the angle between gravity and the kite's lateral direction (\mathbf{y}_K) into account and is defined by:

$$\cos(\angle\{\mathbf{g}, \mathbf{y}_K\}) = \frac{\mathbf{g}_w^T \mathbf{T}_K \mathbf{y}_K}{\|\mathbf{g}\|} = [0 \ 0 \ 1]_w \mathbf{T}_K \begin{bmatrix} 0 \\ 1 \\ 0 \end{bmatrix} = \cos(\theta_0) \sin(\phi_0) \quad (5-9)$$

In the thesis of Jehle [71] and the paper of Erhard and Strauch [72] a identical relation is proposed.

It was chosen to use a term depending on the gravity vector instead of the side slip angle β . This is due to the fact that the gravity vector is evaluated more precise and easier than the side slip angle (which needs estimation of \mathbf{v}_{App}) and as explained in the previous section the side slip angle β mainly depends on the gravity vector so the relations are similar. The relation (5-8) is fitted to the measurement data. The parameters c_1 and c_2 are determined by a least square curve fit. The results of the data and the fit are plotted in Figure 5-17 with the following coefficients $c_1 = 0.207$ and $c_2 = 0.257$

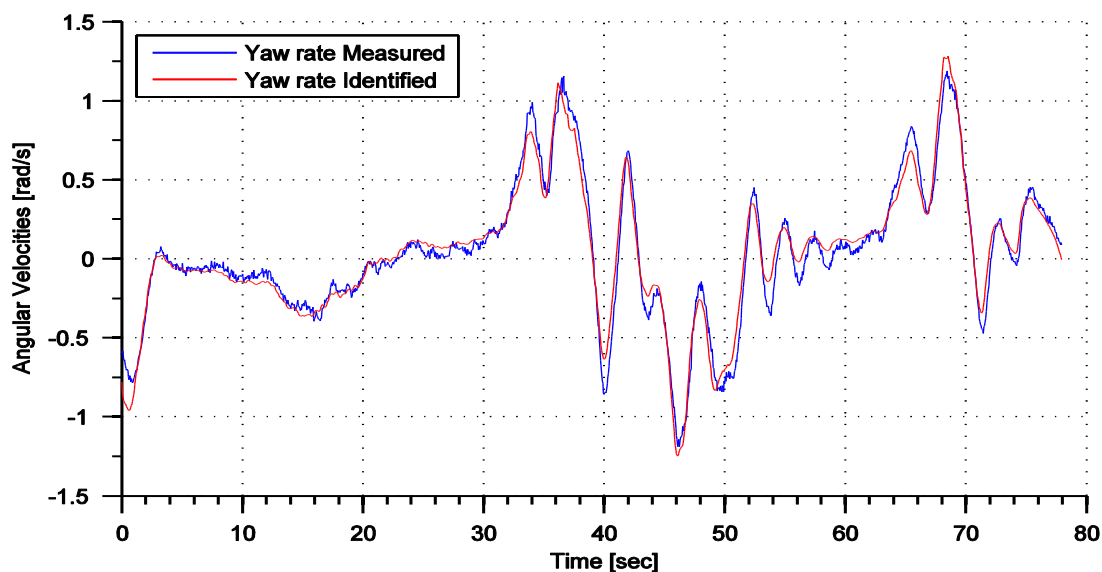


FIGURE 5-17, FIT YAW RATE, $c_1 = 0.207$ AND $c_2 = 0.257$, DATASET 1

The fit shows surprisingly good agreement with the measured data. This relation is very useful in modelling and controller design. It links the rotation rate around the tether to the steer input. Since the rotation around the tether is the main degree of freedom controlling the kite a reliable simple formula describing this relation is practical. The physical phenomena behind the relation were described beforehand. Worth mentioning is that this relation is only valid during powered flight. When the kite is depowered (pitched) a similar relation is found only the fitted coefficients are lower, as a result larger steer inputs are needed for the same rotation rate. This could already be expected when looking at formula (5-7), during depowered flight the glide ratio is lower which result in lower rotation rates. To check the simplistic quasi static analysis the values are compared with the values found with the curve fitting. Formula (5-7) is filled with the following kite parameters: $C_L/C_D = 5$, $b = 7$ and $a(P_s) = P_s$ and a value of 0.20 is found which is close to the value found in the fit. The relation $a(P_s) = P_s$ describes the relation between the steer input and the relative position of the left and right wingtip and define that 20% steer input results in a 40cm offset between the left and right wingtip. The real relation is still unknown, but the direct matching of the values supports the analysis.

Additionally an identification with the side slip angle β is done to check the analysis of section 5.6.2 is correct.

$$r(P_s) = c_1 v_{App} P_s + c_3 \beta \quad (5-10)$$

The parameters c_1 and c_2 are determined by a least square curve fit. The fit is slightly worse than (5-8) but still accurate. The results of the data and the fit are plotted in Figure 5-18 with the following coefficients $c_1 = 0.207$ and $c_3 = -1.152$.

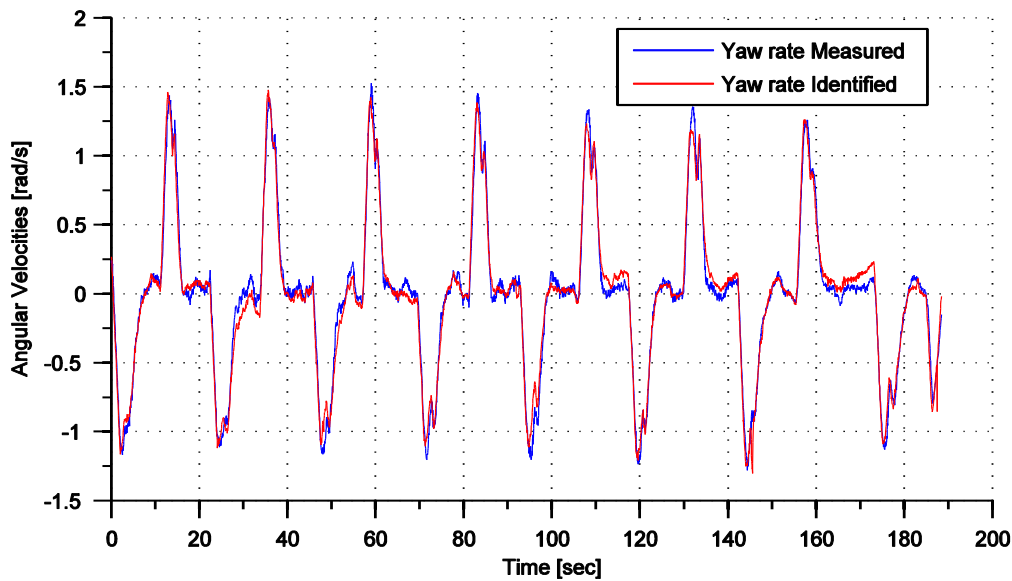


FIGURE 5-18, FIT YAW RATE, $c_1 = 0.232$ AND $c_3 = -1.152$, DATA 14-6-2012

Since the found relation (5-7) corresponds with the test data it is worth to study the relation a little more in-depth.

$$r \approx \frac{2}{b^2} \frac{C_L}{C_D} a(P_s) v_{App} \quad (5-7)$$

The relation tells us that a kite turns faster if it's flying faster or if the kites wingtips has a higher glide ratio. Further a more flexible kite will results in higher $a(P_s)$ which increases turning. On the other hand the kite's turning speed declines with the square of the width of the kite. This is an important finding. When the size of the kite increases both $a(P_s)$ and b will most likely increase linear. As a result bigger kites will turn slower. This could also be intuitively derived by looking at the apparent wind at the kite tips. Currently both tips have almost the same apparent wind speed with only small differences. However when the width of the kite is increased the difference in apparent wind speed becomes bigger. The outside tip will reach a maximum speed depending on the lift over drag ratio while the inside tip could theoretically only stand still.

In the derivation of the relation two terms were neglected which start to play a role when the kite becomes bigger. Therefore no statements can be made for very large kites but what has to be kept in mind is that larger kites most likely have a different turning behaviour then the relative small kites currently used.

5.7 APPARENT WIND SPEED MODEL

In this paragraph the modelling of the apparent wind speed vector is examined. Kite models need the apparent wind speed vector which is calculated with the wind speed vector and the kite velocity vector. Since the wind speed increases with height the local wind speed vector has to be estimated with a wind shear model. In this thesis the log law wind profile is used which is defined by [8]:

$$\mathbf{v}_{Wind}(z) = \mathbf{v}_{ref} \frac{\ln\left(\frac{z}{z_0}\right)}{\ln\left(\frac{z_{ref}}{z_0}\right)} \quad (2-1)$$

Where z is the altitude, \mathbf{v}_{ref} is the measured wind speed. z_{ref} is the height of the wind speed sensor which is currently 6m and z_0 is the surface roughness length. The apparent wind speed is calculated with:

$$\mathbf{v}_{App} = \mathbf{v}_{Wind} - \mathbf{v}_{Kite} \quad (2-4)$$

The correct estimation of the apparent wind speed is important in the system identification and validation of the models. Since in the current prototype the apparent wind speed is measured by a pitot tube the calculated value could be compared with the measured one. But beforehand the surface roughness length of the log law has to be found. The coefficient z_0 is fitted with a least square fitting algorithm to the data. Figure 5-19 shows the pitot measurement and the calculated apparent wind speed with and without wind shear model.

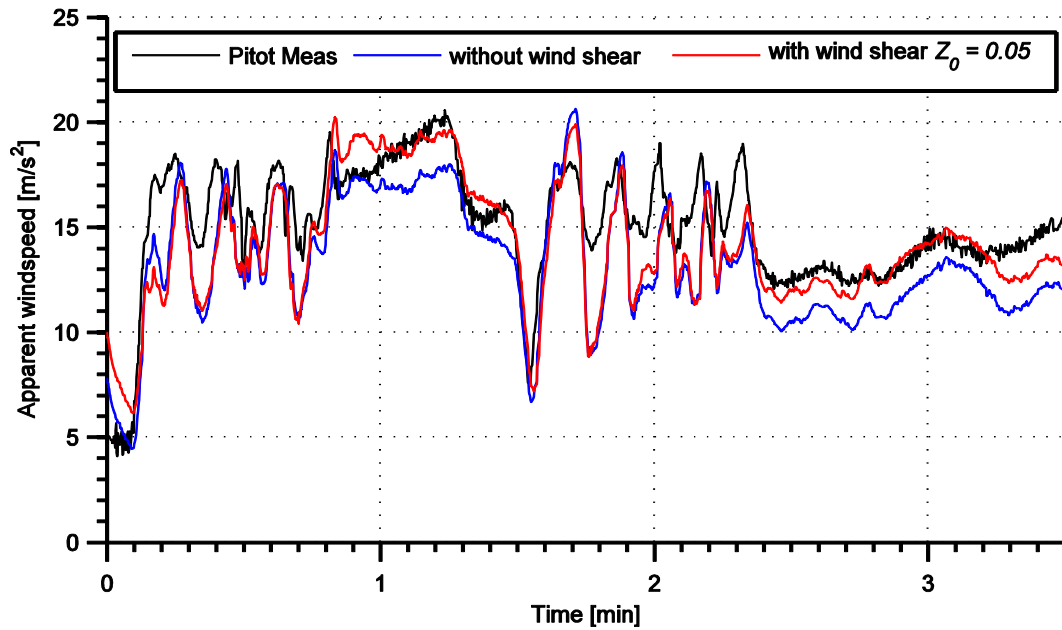


FIGURE 5-19, FITTED SURFACE ROUGHNESS LENGTH, TEST DATA FROM 20-2-2012

For this data a coefficient z_0 of 0.05 is found. The calculated apparent wind speed and the measured value have the same pattern however could deviate up to 10%. The same fitting procedure has also been performed on other test days, it was noticed that the fitted roughness coefficients changes each test day and even during test days. Apparently quite different wind profiles are possible.

To check whether the measurements of the pitot tube are correct the data is compared to the square root of the tether force in Figure 5-20. Additionally the calculated apparent wind speed (this day with a fitted roughness coefficient z_0 of 1) is plotted.

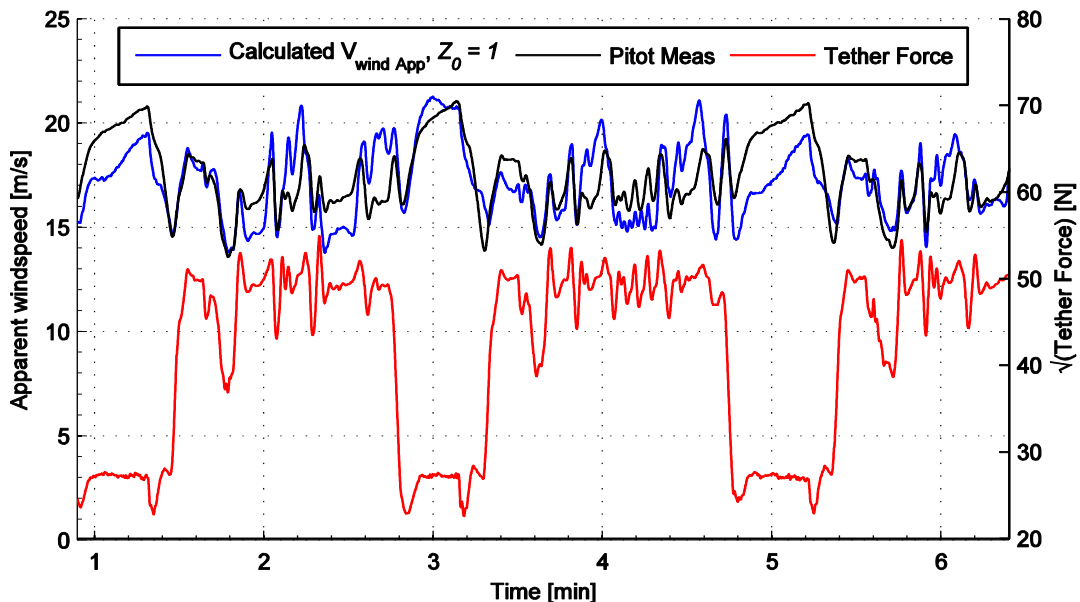


FIGURE 5-20, PITOT MEASUREMENT DATASET 1

In the figure the force measurement shows more resemblance with the pitot measurements, indicating a correct measurement of the pitot tube and errors in the estimated apparent windspeed. The calculated apparent wind speed deviates from the measured values, errors in the order of 1-4 m/s are found.

5.8 ANGLE OF ATTACK AND SIDE SLIP ANGLE

In the previous section the apparent wind speed is calculated. With the orientation of the kite and the apparent wind speed the angle of attack and side slip angle of the kite could be calculated. The angle of attack and side slip angle are plotted in Figure 5-21.

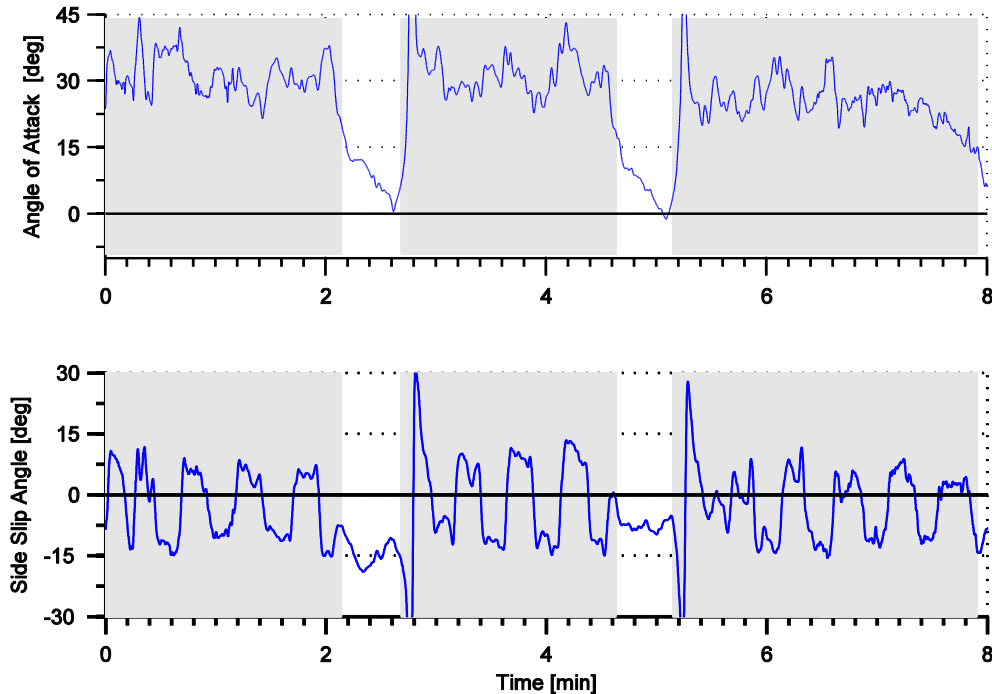


FIGURE 5-21, ANGLE OF ATTACK AND SIDE SLIP ANGLE, DATASET 4

The angle of attack graph shows a fluctuating pattern between 30-40 degrees during the generation phase. During the retraction phase the angle of attack is reduced to 0-10 degrees. It should be noticed that the angle of attack depends on the definition of the chord line. Currently the chord line is not defined and the measured angles depend on the mounting of the X-Sense sensor. Consequently, the measured angles of attack will shift up or down depending on your chord line definition. Nevertheless the line shows differences of 30 degrees between powered and depowered flight.

The plot of the side slip angle clearly shows the effect of gravity. As explained before the side slip angle is needed to overcome the gravity effect on the kite. Since the kite is flying in two directions the measured angle switches each turn.

5.9 GPS ACCURACY

In the current prototype GPS sensors are used to determine the position. Till February 2012 the X-Sens Mti-G was used. When analysing the data sometimes unrealistic values were found, especially during high wind conditions and highly dynamic manoeuvres. First of all the GPS-fix is lost when accelerations exceed 4G. But also with GPS fix faulty data was found. It was noticed that the velocity vector is not aligned to the track during fast corners. The velocity vector starts to turn inwards before the turn starts [71]. In February 2012 a new GPS sensor, the Trimble GPS sensor BX982 with AV34 antenna was tested to see if these problems could be solved. The evaluation of the GPS sensors is difficult because the location of the sensor is unknown. The only test available which does not depend on GPS data is to compare the length of the cable to the distance between the ground station position and GPS sensor position. The tether length is measured by integrating the rotations of the winch of the groundstation. Figure 5-22 shows the results.

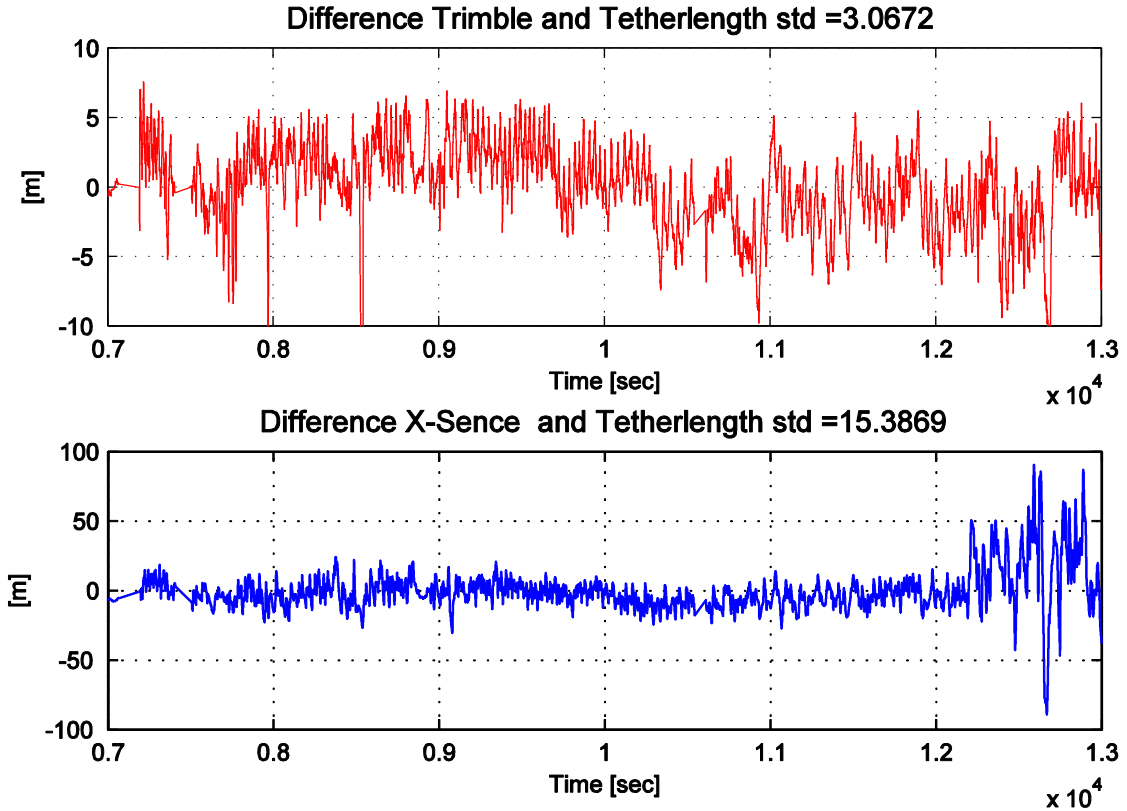


FIGURE 5-22, COMPARISON GPS LINE LENGTH WITH MEASURED LINE LENGTH, 24-4-2012

The Trimble GPS line length is almost always within 10m of the actual value and has a standard deviation of 3m. When taken into account that the tether length also changes due to sagging of the cable and elongation the similarity between the lengths are above expectations and indicates the Trimble GPS gives an accurate location. The X-Sens sensor resulted in bigger differences. The X-Sens especially seems to lose track near the end of the test. Deviations of 50m are measured. During this period slightly higher accelerations were measured.

The performance of the Trimble was additionally evaluated at a day with high wind conditions (since high wind conditions generally cause higher accelerations). The data is shown in Figure 5-23 and the path and velocity vectors are plotted in a frond view in Figure 5-24.

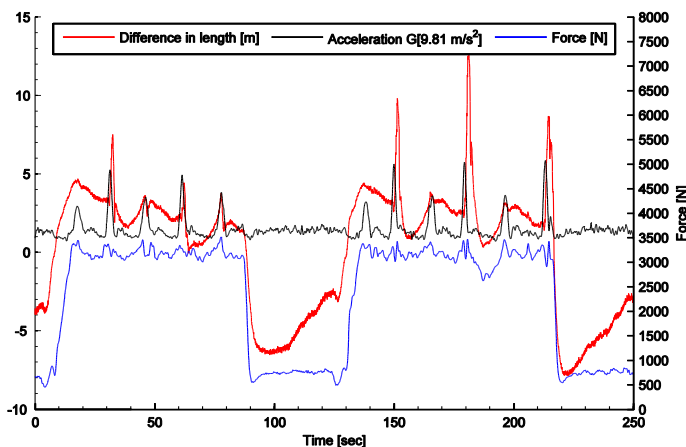


FIGURE 5-23, COMPARISON GPS LINE LENGTH WITH MEASURED LINE LENGTH, DATASET 6

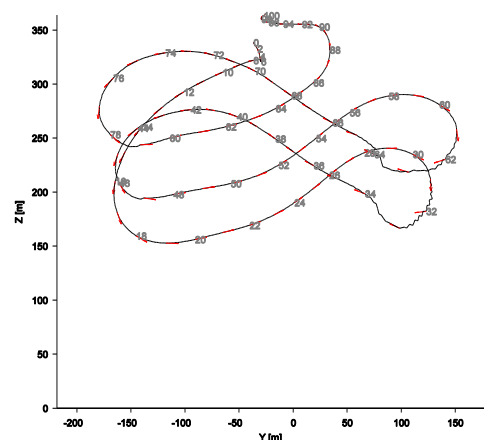


FIGURE 5-24, PATH AND VELOCITY VECTOR MEASURED BY TRIMBLE GPS

Multiple important phenomena show up. First of all the accuracy of the GPS is really remarkable. When there is a good fix the effects of tether sag and tether elongation can be found in the GPS data. To start with the tether sag, during the generation phase a decreasing slope is found in the difference in length. This is due to the fact that the cable reels out and longer cable will sag more. Secondly the small variations in difference in length are identical to the force in the tether measured at the groundstation. So with the GPS sensor even the elongation of the tether is measured.

However, during high accelerations, i.e. fast turns, the Trimble GPS sensor sometimes loses its accuracy. This is clearly shown at sec 32 and 60. During and after a high acceleration the accuracy is 'only' 10m. This is still within the specifications of the Trimble however not as good as before. In Figure 5-24 the path and velocity vectors are plotted. Important is that during the high acceleration turns the velocity vector gets significantly off. This is really problematic for the autopilot and the correct calculation of the apparent wind speed and should be kept into mind when evaluating the data.

5.10 AERODYNAMIC COEFFICIENTS

LIFT AND DRAG COEFFICIENT

To model the aerodynamic forces reliably the lift and drag curves of the kite are needed. The curves of the present kite are currently unknown. The most reliable method to determine these curves is with the aid of wind tunnel testing. However this is very expensive and it is unlikely that each kite will be evaluated in a wind tunnel. Another way to determine the parameters is with the aid of a CFD program but this still is an expensive and time consuming process. Moreover the complex fluid-structure interaction has first to be further investigated before reliable CFD data is available. Fortunately there are other ways to determine the aerodynamic parameters. In the paragraph 2.6.1 the well-known crosswind motion law (2-5) was described. This relation couples the glide ration to the crosswind velocity of the kite, the reel speed and the wind speed. This relation is derived only for flying perfectly downwind. Argatov has extended this relation to cover all cases. Worth mentioning is that in the derivation still the inertia forces are neglected. The derivation and the complete formula can be found in reference [73], when assuming that $v_{\parallel Wind} \ll v_{cross}$ the following simplified relation is deduced.

$$v_{cross} = (v_{\parallel Wind} - v_L) \left(\frac{L}{D} \right) \quad (5-11)$$

Note that $v_{cross} = proj_{xy_{SE}} \mathbf{v}_{App}$, which means the apparent wind speed projected on the tangential plane (= xy_{SE}) and $v_{\parallel Wind} = \mathbf{v}_{Wind} \cdot \mathbf{p}^{OP}$ is the wind speed in the direction of the tether. To get a first approximation of the aerodynamic coefficients the glide ratio is calculated and plotted during a figure of 8. For this derivation the apparent wind speed is calculated with the aid of a wind shear model (see 5.7).

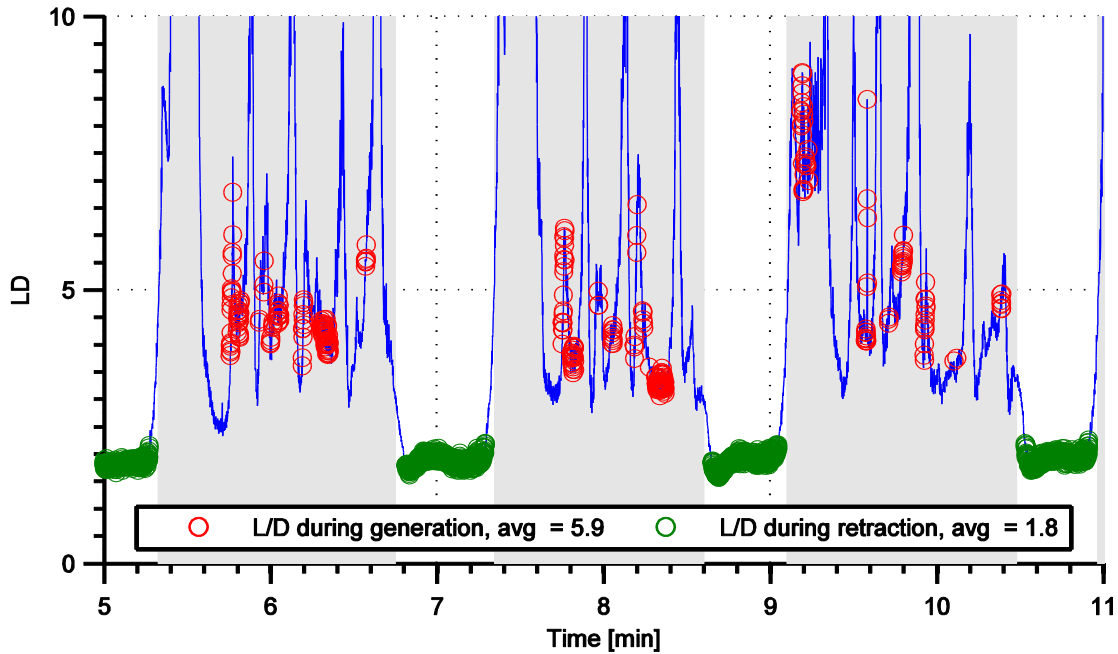


FIGURE 5-25, CALCULATED LD DURING CYCLES

In Figure 5-25 the calculated glide ratio is plotted, a highly fluctuating pattern is shown during the generation phase. Apparently the inertia and weight effects have a large influence on the values. To exclude some of the inertia effects data points during straight flight are selected, the red circles indicate data points without steer input. It can be seen that on average there is glide ratio of 5.9 during power. During the retraction phase a nice constant glide ratio is realized. On average a glide ratio of 1.8 is found.

In Figure 5-26 the calculated glide ratio is plotted against the calculated angle of attack.

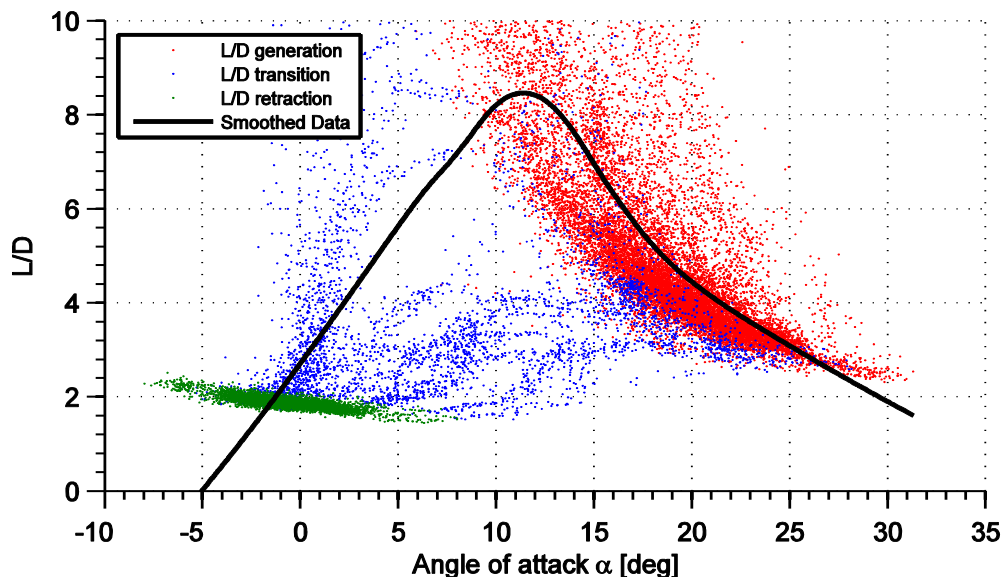


FIGURE 5-26, GLIDE RATIO VERSUS ANGLE OF ATTACK

During the generation phase the kite is mostly flying at angles of attack of 15-25 degrees with a glide ratio around 5. During retraction phase the angle of attack is reduced to 0 degrees with a glide ratio of 2. A glide ratio versus angle of attack curve is deduced by smoothing the data with a 'weighted linear least squares and a 2nd degree polynomial model'.

To simulate the kite the aerodynamic coefficients are still needed. The aerodynamic coefficients could be approximated by using the measured aerodynamic force and the calculated angle of attack of the apparent wind speed. First of all the aerodynamic force has to be calculated with the method described in section 5.3:

$$(\mathbf{F}_{\text{Aer}})_K = m_{\text{kite}}(\mathbf{a})_K - (\mathbf{F}_{\text{T}})_K - (\mathbf{F}_{\text{Gra}})_K \quad (5-12)$$

The resultant aerodynamic force coefficient C_R is calculated by dividing the aerodynamic force by the velocity head:

$$C_R = \frac{|\mathbf{F}_{\text{Aer}}|}{0.5\rho_{\text{air}}A_{\text{kite}}|\mathbf{v}_{\text{App}}|^2} \quad (5-13)$$

For all data points the force coefficient is plotted against the angle of attack resulting in the following plot:

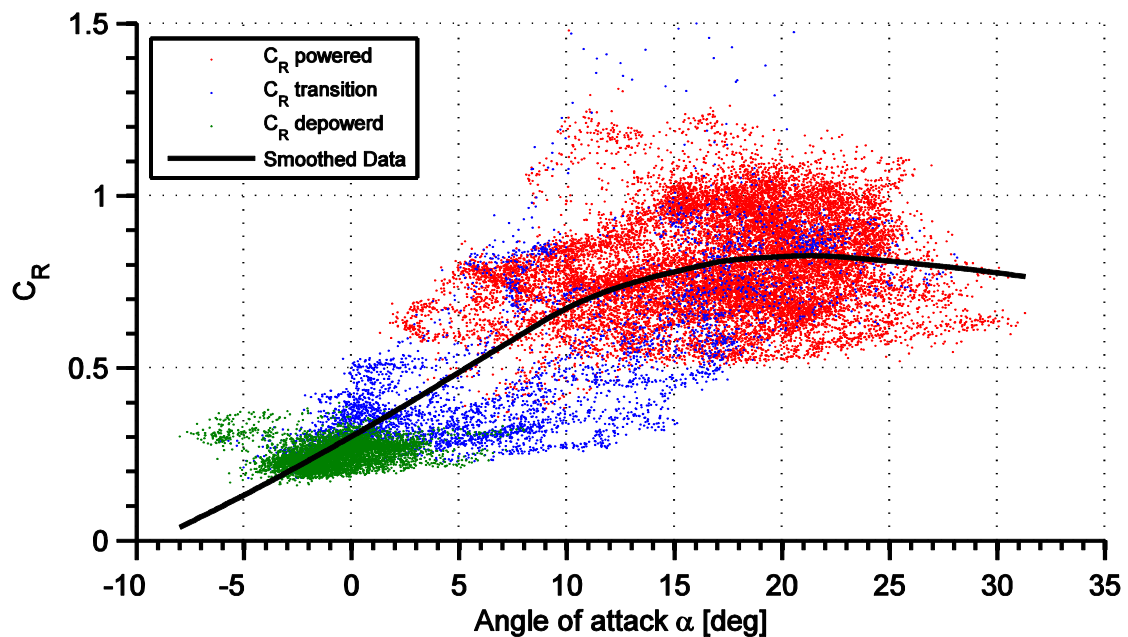


FIGURE 5-27, RESULTANT FORCE COEFFICIENT VERSUS ALPHA

A C_R versus angle of attack curve is deduced by smoothing the data with a 'weighted linear least squares method'. Since the glide ratio and aerodynamic force coefficient curves are known an approximation for the $C_L(\alpha)$ and $C_D(\alpha)$ curve can be derived by combining these two graphs.

$$\begin{aligned} C_R^2 &= \sqrt{C_L^2 + C_D^2} \\ C_D &= \frac{C_R}{\sqrt{\left(\frac{C_L}{C_D}\right)^2 + 1}} \\ C_L &= \frac{C_L}{C_D} C_D \end{aligned} \quad (5-14)$$

This results in the following $C_L(\alpha)$ and $C_D(\alpha)$ curve (Figure 5-28).

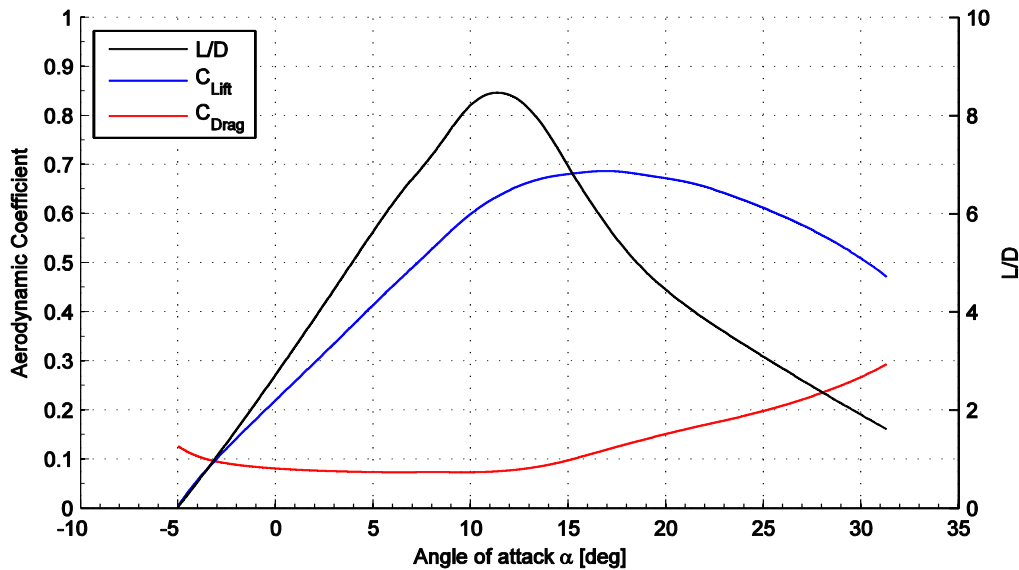


FIGURE 5-28, CL, CD VS. ALPHA CURVE

SIDE FORCE COEFFICIENT

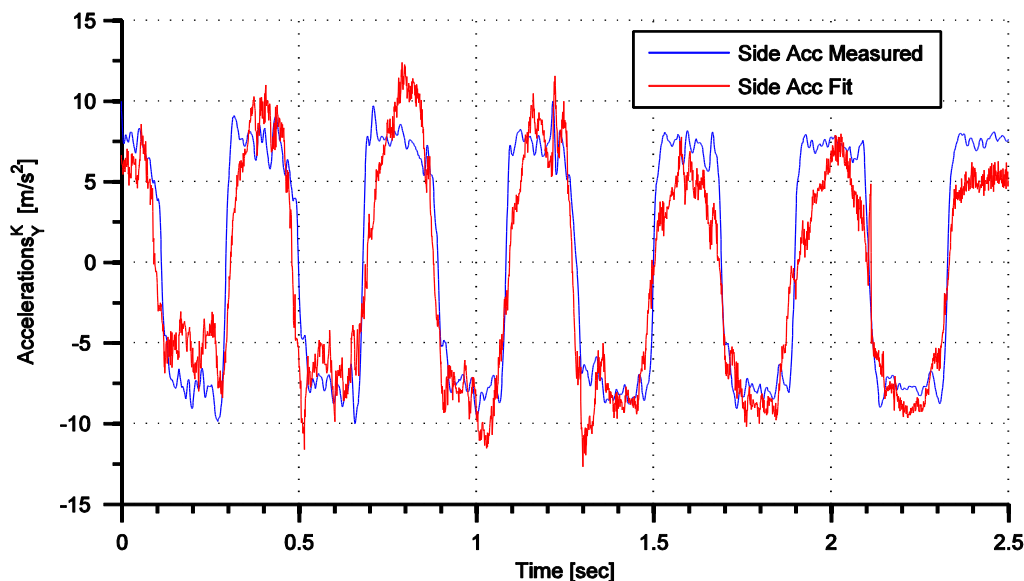
Besides the lift and drag force also a side force is acting on the kite. Without a side force the kite would just fly in a straight line. In various kite papers [43, 45, 47, 48, 59] a linear relation between side force and side slip angle is proposed. This relation could also be found by looking at Figure 5-16. A side slip angle will result in a different angle of attack at the left and right wingtip, as a result a side force is formed in the opposite direction of the side slip. To check the relation and to find the aerodynamic coefficient the following relation was proposed and fitted with a linear least square algorithm to measurement data.

$$F_{Side} = m_{kite} (\mathbf{a}_y)_K = \frac{1}{2} \rho_{air} A_{side} |\mathbf{v}_{App}|^2 C_S (\beta)$$

$$C_S (\beta) = c_4 \beta \quad (5-15)$$

$$c_4 = \frac{m_{kite} (\mathbf{a}_y)_K}{\frac{1}{2} \rho_{air} A_{side} |\mathbf{v}_{App}|^2 \beta}$$

Where $(\mathbf{a}_y)_K$ is the acceleration in the kite y_K axis direction. The data and the fit are plotted in Figure 5-29 with the coefficients $c_4 = 0.8$

FIGURE 5-29, FITTED SIDE SLIP COEFFICIENT $C_4=0.8$

5.11 DEVELOPED SOFTWARE TO ANALYSE DATA

The data produced by the system sensors are saved in txt log files. During the writing of this thesis all software has been reprogrammed in a C++ environment. As a result different log files formats were created during the different test days. To easily read in the different old and new log files a read in routine in Matlab ('dataread.m') was developed in cooperation with Jehle [71]. The routine is able to read in all data correctly and stores all data into a structure 'Data' where all data points from each sensor are saved with their own time stamp. During the read in routine the data is not resampled or changed. The structure does not offer a practical way to analyse the results. The structure contains a lot of data and not always all sensors are active. Therefore another GUI, 'Select_Resample.m', is developed which is able to select parts of the imported data. This GUI is also able to resample all data. Finally the GUI sends the selected data to another plotting GUI, 'LogAnalyzer.m'.

The plotting GUI is able to plot the kite and the sensor data. The graphical display of the kite makes it easier to analyse all data. With a slider box the log files can be replayed.

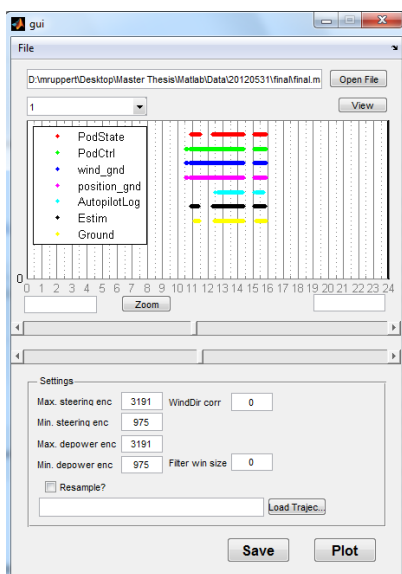


FIGURE 5-30, SELECT AND RESAMPLE GUI

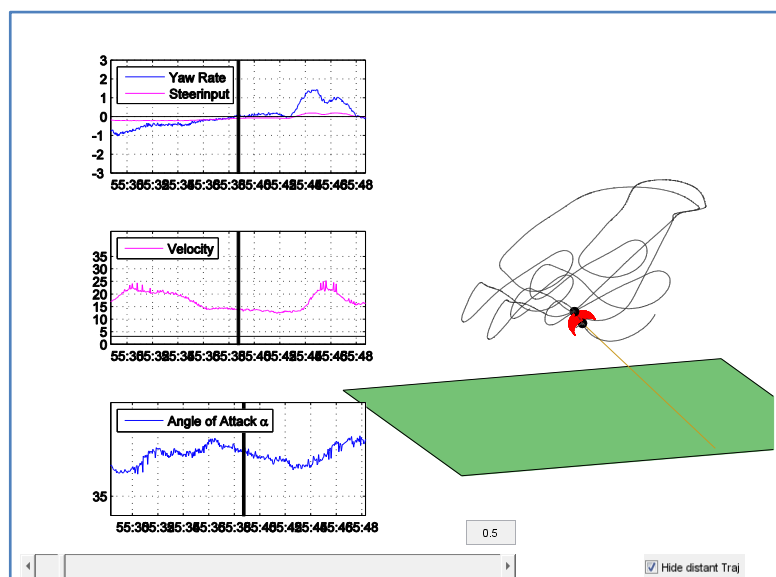


FIGURE 5-31, LOGANALYZER

6 KITE MODEL

In the data analysis and system identification the general dynamics of the system have been described. Goal of this thesis is the development of a simple real time validated kite model. With the new understanding of the system the models discussed in the literature study can be re-evaluated and an informed choice can be made for the intended model after which this model is described.

6.1 MODEL OPTIONS

One of the main requirements is that the model has to be able to run in real time. In the literature study it was found that only the analytic, point mass and semi rigid body kite models are candidates for real time modelling. If a complete rigid body kite model can run real time depends on the implementation. With the knowledge of the system identification the possibilities are assessed.

Analytic kite models model the kite on a quasi-static basis and therefore neglect the inertia of the kite, in the system identification the effects of inertia could however be seen clearly. Especially in section 5.10 where the aerodynamic performance of the kite was assessed. In Figure 5-25 the glide ratio was calculated on a quasi-static manner, the result was unrealistically fluctuating during the generation phase. Analytic models are useful for system performance evaluation over long periods (> 10 cycles), where forces could be averaged over longer periods. For controller design and system optimizations the inertia effects have to be taken into account and therefore analytic models are inadequate.

Point mass models are relatively simple models which take the inertia effects into account. The point mass models are based on three assumptions. The first assumption is that the kite aligns itself immediately to the apparent wind speed. As a result the orientation of the kite is coupled to the wind reference frame. The steering is induced by applying a side force. The second assumption is that the tether is straight and the kite is constraint in two directions (roll and pitch) by the tether. Last assumption is that the kite has a constant angle of attack. In the system identification these assumptions were evaluated. To start with the third assumption, the angle of attack was plotted in Figure 5-21 and clearly a fluctuating pattern can be seen. Indicating a false assumption. This could however easily be solved by using a variable angle of attack which is already implemented in some point mass models (see Table 5). The straight tether assumption and the orientation of the kite have been assessed in section 5.5. It was established that the kite is indeed constrained in two directions. The effect of tether sag and pod dynamics are also examined, an angle relative to the straight tether in the order of 0 - 10 degrees is found. This is a fairly small angle and a straight tether assumption seems valid. Worth mentioning is that during downward turns the pitch angle is increased due to the pod dynamics (see Figure 5-10), as a result the angle of attack will increase. This effect will probably influence the system. The last assumption is that the kite is always aligned with the apparent wind. In section 5.8 became clear that the kite occasionally flies with significant side slip and drift angles due to steer inputs and the gravitational forces. Especially during the retraction phase, offsets can be found. Therefore this assumption is not valid. Besides that a direct coupling between the apparent wind and the orientation of the kite makes it impossible to study the orientation dynamics.

Rigid body models are able to model the orientation dynamics however as stated before the kite is largely constraint in two directions. When these rotations are modelled dynamically the resultant differential equations would be very stiff compromising the ability to do real time modelling. This has been noticed before in the literature study.

To solve the problems with the stiff differential equations in rigid body models and to include attitude dynamics a semi rigid body model is proposed. A semi-rigid body model could be seen as an extended point mass model with one rotational degree of freedom or a rigid body model where two rotational degrees of freedom have been substituted by analytic relations. The data analysis showed this approach is promising. The

kite is largely constrained in two directions and there is a relation between the last rotational degree of freedom and the steer input. The straight tether assumption seems valid however the effects of the dynamics of the tether drag and control pod weight could be taken into account. Based on the analysis it is chosen to develop and validate a semi-rigid body kite model. This model approach seems most promising to result in a realistic and real time kite model. Still the question is if a straight tether assumption is valid. During turns the pitch is increased due to the weight of the pod. This could be simulated by a discretised point mass tether model. To evaluate the effect of a tether model an optional discretised tether model is included. The tether model is elaborated in chapter 7.

6.2 SEMI RIGID BODY KITE MODEL

6.2.1 DYNAMIC EQUATIONS

The semi rigid body model which is developed and validated in this thesis is based on the work of Knappskog [47]. Because of its crucial importance for the whole thesis the model is elaborated and some changes are implemented. The semi-rigid body model can be seen as a point mass kite model with one additional degree of freedom, the rotation around the tether. Therefore the starting point is the kinematics of a point mass in spherical coordinates. This has already been elaborated in multiple kite power publications [40, 63, 74] but is also repeated here for understanding. The Euler-Lagrange equation is used to derive the model.

The earth-groundstation reference frame, EG , will be used as the inertial frame and is shown in Figure 4-1. The effect of the rotating earth can be neglected as already stated by Jehle [71]. The generator is placed at the origin. The kite is at position $\mathbf{P} \in \mathbb{R}^3$ with a straight cable of length $r > 0$ to the generator. The wind $\mathbf{v}_{\text{Wind}} \in \mathbb{R}^3$ is blowing with an angle $\chi_w \in [0^\circ \ 360^\circ]$ in respect to \mathbf{x}_{EG} . Note that we explicitly do not use the wind reference frame, W , as inertial frame since we want to be able to model changes in wind direction.

The kite is modelled with the spherical coordinates $q := (r, \vartheta, \eta)^T$, where r is the length of the cable, $\eta \in [0^\circ \ 180^\circ]$ is the angle between the cable and $(\mathbf{xy})_{EG}$ plane and $\vartheta \in [0^\circ \ 360^\circ]$ is the angle between the projection of the cable onto the horizontal plane and \mathbf{x}_{EG} . Note that $\vartheta = \chi_w + \xi$. Further should be noticed that these spherical coordinates are not the 'standard' (r, ϕ, θ) and are different than the one used in the various kite modelling papers. They correspond to the reference frames used in the ASSET kite group.

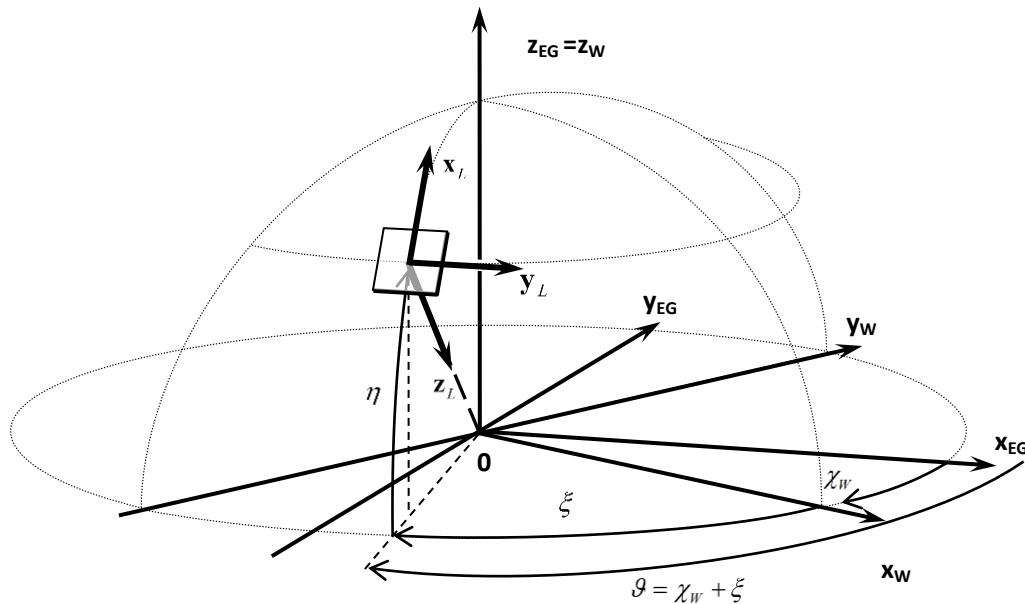


FIGURE 6-1, LOCAL REFERENCE FRAME L AND SPHERICAL COORDINATES

The following rotation matrix is used to transform from the inertial frame EG to the local orthogonal frame L (see Appendix D):

$${}^L\mathbf{T}_{EG} = {}^L\mathbf{T}_W {}^W\mathbf{T}_{EG} = \begin{bmatrix} -s\eta c\vartheta & s\vartheta s\eta & c\eta \\ s\vartheta & c\vartheta & 0 \\ -c\eta c\vartheta & s\vartheta c\eta & -s\eta \end{bmatrix} \quad (6-1)$$

$$(\mathbf{x}_L, \mathbf{y}_L, \mathbf{z}_L) := {}^L\mathbf{T}_{EG} (\mathbf{x}_{EG}, \mathbf{y}_{EG}, \mathbf{z}_{EG})$$

The velocity of the kite with respect to the new orthonormal basis vector $(\mathbf{x}_L, \mathbf{y}_L, \mathbf{z}_L)$ is

$$\dot{\mathbf{p}} = -\dot{r}\mathbf{z}_L - r \cos(\eta)\dot{\vartheta}\mathbf{y}_L + r\dot{\eta}\mathbf{x}_L \quad (6-2)$$

To derive the kite's equations of motion the Lagrangian formalism is used.

$$\frac{d}{dt} \left(\frac{\partial \mathcal{L}}{\partial \dot{q}_i} \right) - \frac{\partial \mathcal{L}}{\partial q_i} = Q \quad (6-3)$$

with $\mathcal{L} := T_{kin} - U$ being the Lagrangian and $Q \in \mathbb{R}^3$ is the generalized force. First the formulas for the kinetic energy T_{kin} and the potential energy U are derived. The kinetic energy has two components, the kinetic energy of the kite and the tether, and is defined by:

$$\begin{aligned} T_{tether} &= \int_0^l \frac{1}{2} m_{tether} |\dot{\mathbf{s}}\mathbf{p}|^2 ds = \frac{1}{6} m_{tether} |\dot{\mathbf{p}}|^2 \\ T_{kite} &= \frac{1}{2} m_{kite} |\dot{\mathbf{p}}|^2 \\ T_{tether} + T_{kite} &= \frac{1}{2} \left(m_{kite} + \frac{m_{tether}}{3} \right) |\dot{\mathbf{p}}|^2 = \frac{m}{2} \left(\dot{r}^2 + r^2 \cos^2(\eta) \dot{\vartheta}^2 + r^2 \dot{\eta}^2 \right) \end{aligned} \quad (6-4)$$

Where $m = m_{kite} + \frac{m_{tether}}{3}$ and represents the effective inertial mass. The potential energy is defined by

$$\begin{aligned} U_{kite} &= (m_{kite} - \Omega \rho_{air}) gh = mgr \sin(\eta) \\ U_{tether} &= m_{tether} g \frac{h}{2} = -\bar{m} gr \sin(\eta) \\ U_{kite} + U_{tether} &= - \left(m_{kite} + \frac{m_{tether}}{2} \right) gr \sin(\eta) = -(\bar{m}) gr \sin(\eta) \end{aligned} \quad (6-5)$$

Here Ω is the volume of the kite and $\bar{m} = m_{kite} + \frac{m_{tether}}{2} - \Omega \rho_{air}$ which represents the effective gravitational mass. The different between \bar{m} and m is the fact that the air inside the kite has to be taken into account when evaluating the inertia while the air does not add to the gravitational force. The potential energy in the tether is neglected due to the small effect, see the paper of Hoeska [63] for a derivation with the potential energy of the tether taken into account. Combining (6-3) with (6-4) and (6-5) results in the following equation of motion.

$$\ddot{q} = S^{-1} \frac{(\mathbf{F})_L}{m} - a \quad (6-6)$$

The complete derivation of this formula is found in multiple papers, for example the work of Hoeska [63].

In formula (6-6) S is a scaling matrix:

$$S = \begin{bmatrix} 0 & 0 & r \\ 0 & -r \cos(\eta) & 0 \\ -1 & 0 & 0 \end{bmatrix} \quad (6-7)$$

a is a pseudo acceleration which becomes negligibly small for long cables:

$$a = \begin{bmatrix} -r \cos^2(\eta) \dot{\vartheta}^2 - r \dot{\eta}^2 \\ -2 \tan(\eta) \dot{\vartheta} \dot{\eta} + 2 \frac{\dot{r}}{r} \dot{\vartheta} \\ \sin(\eta) \cos(\eta) \dot{\vartheta}^2 + 2 \frac{\dot{r}}{r} \dot{\eta} \end{bmatrix} \quad (6-8)$$

And $(\mathbf{F})_L$ is the sum of the forces acting on the kite in L reference frame. The forces are the aerodynamic force of the kite, the gravity force and the force of the tether which consists out of two parts. The ‘constraining’ force and the force due to the drag of the cable in the air:

$$(\mathbf{F})_L = (\mathbf{F}_{\text{Aer}})_L + (\mathbf{F}_{\text{Gra}})_L + (\mathbf{F}_{\text{Tether}})_L + (\mathbf{F}_{\text{Tether drag}})_L \quad (6-9)$$

Until this point the derivation describes an ordinary point mass in spherical coordinates $q := (r, \vartheta, \eta)^T$. In most point mass kite models the derivation continues by defining the aerodynamic forces depending on the apparent wind vector, the tether vector and a pseudo control. Note that the point mass does not have an orientation, and as a result the forces are defined in the local reference frame L .

Our goal is a semi-rigid body model, therefore the orientation of the kite is defined by two constraints and one rotational degree of freedom. The constraints fix the kite orthogonal to the tether. The rotation around the tether is the new dynamic state. In addition the pitching of the kite is modelled by varying one constrain. The angle between the tether and the chord line (the pitch angle $\theta^{L,B}$) is directly coupling to the ‘power setting’ P_p . The pitch angle is not a dynamic variable but an analytic relation between the power setting en pitch angle.

Let’s define a body fixed reference frame B , note that it was explicitly chosen to name it ‘body’ to prevent confusion with the kite reference frame K used in the system identification (although they both represent the kite and are almost identical). The body fixed reference frame B is defined by rotating the local reference frame L with a ‘pitch’ angle $\theta^{L,B}(P_p)$ around the \mathbf{y}_L axis and a ‘yaw’ angle $\psi^{L,B}$ around the tether, the \mathbf{z}_L axis. Figure 6-2 shows the orientation of the new body fixed reference frame B and the angle $\psi^{L,B}$. The rotation angle $\psi^{L,B}$ is the new added degree of freedom. The pitch angle $\theta^{L,B}(P_p)$ is only an analytic relation and does not add any dynamics. As a result of the constraints the \mathbf{y}_L axis will always lie in the tangential plane and is orthogonal to the tether which means that the kite always flies with a zero roll relative to the tether. The following rotation matrix is used to transform from the local frame L to the body frame B (see Appendix D):

$${}^B \mathbf{T}_L = \mathbf{T}_Y(\theta^{L,B}(P_p)) \mathbf{T}_Z(\psi^{L,B}) = \begin{bmatrix} c\theta^{L,B} c\psi^{L,B} & c\theta^{L,B} s\psi^{L,B} & 0 & -s\theta^{L,B} \\ -s\psi^{L,B} & c\psi^{L,B} & 0 & 0 \\ s\theta^{L,B} c\psi^{L,B} & s\theta^{L,B} s\psi^{L,B} & c\theta^{L,B} & 0 \end{bmatrix} \quad (6-10)$$

The dynamics of the angle $\psi^{L,B}$ can be determined in two ways. Most consistent would be to use Newton's second law for rotations:

$$\ddot{\psi}^{L,B} = \frac{M_z}{I_{zz}} \quad (6-11)$$

Where M_z is the sum of all moments around the z_B axis and I_{zz} is the mass moment of inertia around the z_B axis. Another option is to use the relation between yaw rate r and steer input which was found in the system identification (section 5.6.3). This would result in a quasi-static approach. In section 6.2.4 both implementations are described.

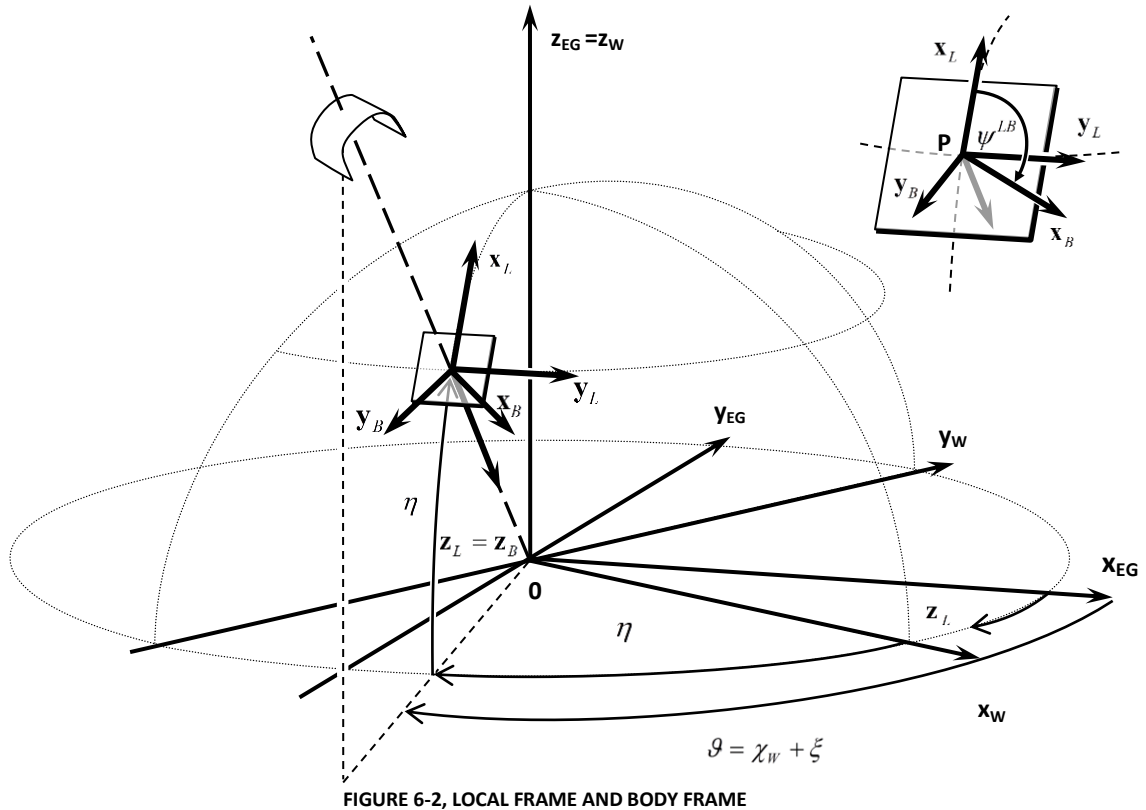


FIGURE 6-2, LOCAL FRAME AND BODY FRAME

As a result the model can be stated as:

$$\begin{pmatrix} \ddot{r} \\ \ddot{\theta} \\ \ddot{\eta} \\ \ddot{\psi}^{L,B} \end{pmatrix} = \begin{pmatrix} \left(S^{-1} \frac{(\mathbf{F})_L}{m} - a \right)_1 \\ \left(S^{-1} \frac{(\mathbf{F})_L}{m} - a \right)_2 \\ \left(S^{-1} \frac{(\mathbf{F})_L}{m} - a \right)_3 \\ \frac{M_z}{I_{zz}} \end{pmatrix} \quad (6-12)$$

For understanding and convenience the model is described in state space.

$$\begin{aligned} \dot{\mathbf{X}}(t) &= f(t, \mathbf{X}(t), \mathbf{U}(t)) \\ \mathbf{Y}(t) &= h(t, \mathbf{X}(t), \mathbf{U}(t)) \end{aligned} \quad (6-13)$$

First the state vector and input vector are defined:

$$\mathbf{X}(t) = \begin{pmatrix} r \\ \vartheta \\ \eta \\ \dot{r} \\ \dot{\vartheta} \\ \dot{\eta} \\ \psi \\ \dot{\psi} \end{pmatrix}, \mathbf{U}(t) = \begin{pmatrix} \mathbf{v}_{\text{Wind}} \\ P_s \\ P_p \\ r_{\text{ref}} / \dot{r} / \ddot{r} \end{pmatrix} \quad (6-14)$$

As a result the system is defined as:

$$\dot{\mathbf{X}}(t) = \begin{pmatrix} \dot{r} \\ \dot{\vartheta} \\ \dot{\eta} \\ \ddot{r} \\ \ddot{\vartheta} \\ \ddot{\eta} \\ \dot{\psi} \\ \dot{\psi} \end{pmatrix} = \begin{pmatrix} X_4 \\ X_5 \\ X_6 \\ \left(S^{-1} \frac{(\mathbf{F})_L}{m} - a \right)_1 \\ \left(S^{-1} \frac{(\mathbf{F})_L}{m} - a \right)_2 \\ \left(S^{-1} \frac{(\mathbf{F})_L}{m} - a \right)_3 \\ X_8 \\ \frac{M_z}{I_{zz}} \end{pmatrix} = f(t, \mathbf{X}(t), \mathbf{U}(t)) \quad (6-15)$$

6.2.2 AERODYNAMIC ANGLES

Before the forces on the kite are defined it is convenient to first define the aerodynamic angles, the angle of attack α and the sideslip angle β . The apparent wind vector is given by:

$$\begin{aligned} (\mathbf{v}_{\text{App}})_B &= (\mathbf{v}_{\text{Wind}})_B - (\dot{\mathbf{p}})_B \\ (\mathbf{v}_{\text{App}})_B &= {}_B \mathbf{T}_{EG} (\mathbf{v}_{\text{Wind}})_{EG} - {}_B \mathbf{T}_L (\dot{\mathbf{p}})_L \end{aligned} \quad (6-16)$$

$$(\mathbf{v}_{\text{App}})_B = {}_B \mathbf{T}_L {}_L \mathbf{T}_{EG} (\mathbf{v}_{\text{Wind}})_{EG} - {}_B \mathbf{T}_L \begin{pmatrix} r\dot{\eta} \\ -r \cos(\eta)\dot{\vartheta} \\ -\dot{r} \end{pmatrix} = \begin{pmatrix} (v_{\text{App}}^x)_B \\ (v_{\text{App}}^y)_B \\ (v_{\text{App}}^z)_B \end{pmatrix}$$

Rotation matrix ${}_L \mathbf{T}_{EG}$ is defined in (6-1) and rotation matrix ${}_B \mathbf{T}_L$ is defined in (6-10). The angle of attack and sideslip angle could now be calculated with:

$$\begin{aligned} \alpha &= \arctan \left(\frac{-(v_{\text{App}}^z)_B}{-(v_{\text{App}}^x)_B} \right) \\ \beta &= \arcsin \left(\frac{-(v_{\text{App}}^y)_B}{|\mathbf{v}_{\text{App}}|} \right) \end{aligned} \quad (6-17)$$

The aerodynamic forces are expressed in the apparent wind reference frame AW . Since the aerodynamic angles are known the rotation matrix from AW to B frame can be defined (see Appendix D):

$${}_{AW}\mathbf{T}_B = \mathbf{T}_Y(\pi)\mathbf{T}_Z(\beta)\mathbf{T}_Y(-\alpha) = \begin{bmatrix} -c\alpha c\beta & s\beta & -s\alpha c\beta \\ c\alpha s\beta & c\beta & s\alpha s\beta \\ s\alpha & 0 & -c\alpha \end{bmatrix} \quad (6-18)$$

6.2.3 FORCES

The forces acting on the kite, $(\mathbf{F})_L$, have to be defined. As stated in (6-9) there are four forces:

$$(\mathbf{F})_L = (\mathbf{F}_{Aer})_L + (\mathbf{F}_{Gra})_L + (\mathbf{F}_{Tether})_L + (\mathbf{F}_{Tether\ drag})_L \quad (6-9)$$

GRAVITATIONAL FORCE

The gravity force \mathbf{F}_{Gra} is defined as:

$$(\mathbf{F}_{Gra})_L = \bar{m}(\mathbf{g})_L = \bar{m}g \begin{pmatrix} \cos \eta \\ 0 \\ -\sin \eta \end{pmatrix} \quad (6-19)$$

Note that the effective gravitational mass $\bar{m} = m_{kite} + \frac{m_{cable}}{2} - \Omega\rho_{air}$ is used.

TETHER DRAG FORCE

Since the tether is swept through the air when the kite is flying drag forces arise at the tether. These drag forces on the tether result in a force at the kite which is slowing down the kite. The calculation of the drag forces is difficult since all cable parts have different apparent wind speeds. Most accurate would be the incorporation of a tether model, but this is computational intensive. For a start a straight tether is assumed, in chapter 7 the use of a point mass tether model is evaluated. The straight tether assumption makes modelling easier. The drag forces on the kite off a straight tether can be estimated with the following formula [63]:

$$(\mathbf{F}_{Tether\ drag})_L = \frac{1}{8} \rho_{air} C_{\perp D, T} r d_T |\mathbf{v}_{App}| (\mathbf{v}_{App})_L \quad (6-20)$$

AERODYNAMIC FORCE

On the kite aerodynamic forces are acting. Based on aerodynamic theory the forces can be split into three components in the apparent wind reference frame.

$$(\mathbf{F}_{\text{Aer}})_{\text{AW}} = \begin{pmatrix} F_D \\ F_S \\ F_L \end{pmatrix} = \frac{1}{2} \rho_{\text{air}} A_{\text{kite}} |\mathbf{v}_{\text{App}}|^2 \begin{pmatrix} C_D \\ \frac{A_{\text{side}}}{A_{\text{kite}}} C_S \\ C_L \end{pmatrix} \quad (6-21)$$

The aerodynamic coefficients have been studied in the system identification. The lift coefficient C_L and the drag coefficients C_D are functions of the angle of attack α . In section 5.10 an experimental lift and drag curve is deduced which will be used. The side force coefficient C_S is a function of the sideslip angle β . With the aerodynamic coefficients defined the aerodynamic force can be calculated. The aerodynamic force is defined in the apparent wind frame and has to be rotated to the local frame. Combining (6-10) and (6-18) gives:

$$(\mathbf{F}_{\text{Aer}})_L = {}_L \mathbf{T}_B {}_B \mathbf{T}_{\text{AW}} (\mathbf{F}_{\text{Aer}})_{\text{AW}} = {}_L \mathbf{T}_B {}_B \mathbf{T}_{\text{AW}} \left(\frac{1}{2} \rho_{\text{air}} A_{\text{kite}} |\mathbf{v}_{\text{App}}|^2 \begin{pmatrix} C_D(\alpha) \\ \frac{A_{\text{side}}}{A_{\text{kite}}} C_S(\beta) \\ C_L(\alpha) \end{pmatrix} \right) \quad (6-22)$$

TETHER FORCE

The tether force can be modelled in three ways, by a constraint, as a spring damper or as a discretised particle system. The last option is researched in chapter 7. The other two options have both their own advantages. When the tether is modelled as a constraint the relative stiff differential equations of the tether are eliminated and unrealistic vibrations are prevented. However in reality the cable will play an important role in the damping of turbulence and the damping term will dissipate a part of the generated energy. Since the implementation is rather straightforward both options are implemented and the user can decide based on their needs.

When the tether is modelled as a constraint the tether force is determined in the following way:

$$\begin{aligned} \ddot{\mathbf{q}} &= S^{-1} \frac{(\mathbf{F})_L}{m} - a \\ (\mathbf{F})_L &= \begin{pmatrix} F^x \\ F^y \\ F^z \end{pmatrix}_L = (\mathbf{F}_{\text{Aer}})_L + (\mathbf{F}_{\text{Gra}})_L + (\mathbf{F}_{\text{Tether}})_L + (\mathbf{F}_{\text{Tether drag}})_L \\ \ddot{r} &= \frac{-(F^z)_L}{m} + r \cos^2(\eta) \dot{\eta}^2 + r \dot{\eta}^2 \\ (F^z)_L &= -m\ddot{r} + mr \cos^2(\eta) \dot{\eta}^2 + mr \dot{\eta}^2 \\ F_{\text{Tether}} &= (F_{\text{Tether}}^z)_L = -m\ddot{r} + mr \cos^2(\eta) \dot{\eta}^2 + mr \dot{\eta}^2 - (F_{\text{Tether drag}}^z)_L - (F_{\text{Aer}}^z)_L - (F_{\text{Gra}}^z)_L \end{aligned} \quad (6-23)$$

Basically this formula expresses that the force in the tether consist of the inertia forces and the centrifugal forces of the mass and the radial component of the external forces. When the tether is modelled as a spring the force is determined by:

$$(\mathbf{F}_{\text{Tether}})_L = \frac{E_r A_r}{r_{\text{ref}}} (r - r_{\text{ref}}) - \frac{c_0}{r_{\text{ref}}} \dot{r} \quad (6-24)$$

Where r_{ref} is the unstretched tether length which is determined by integrating the reeling speed. The term

$$\frac{E_r A_r}{r_{\text{ref}}} = \frac{k_0}{r_{\text{ref}}} = k \text{ is the spring constant and } \frac{c_0}{r_{\text{ref}}} = c \text{ is the damping constant of the tether.}$$

6.2.4 ROTATION OF THE KITE

For the kite model a relation is needed which describes the rotation of the kite around the tether. The rotations around the tether have been studied in section 5.6. A good empirical relation, equation (5-10), has been found between the yaw rate $\dot{\psi}^{L,B}$, steer input and side slip angle (or gravity vector). The relations between the yaw rate, steer input and side slip angle originates from the fact that the inertia term has a negligible effect on the system, therefore a quasi-static relation was found. For the semi-rigid body model there are now two options to model the rotations. The first option is to use the empirical relation (5-10) to define $\dot{\psi}^{L,B}$ based on the steer input and side slip angle.

$$\dot{\psi}^{L,B} = c_1 v_{App} P_s + c_3 \beta \quad (6-25)$$

An advantage of this approach is that a simple relation describes the rotation of the kite. The rotational accelerations are not modelled and therefore this option is computational efficient. In addition the relation showed a good fit. Disadvantage of this approach is the fact that the full rotational dynamics are not simulated. And the relation depends on empirical coefficients.

When the full rotational dynamics are of interest the rotations could be described by Newton's second law for rotations:

$$\ddot{\psi}^{LB} = \frac{M_z}{I_{zz}} \quad (6-26)$$

Where M_z is the sum of all moments around the \mathbf{z}_B axis and I_{zz} is the mass moment of inertia around the \mathbf{z}_B axis. In section 5.6 the moments acting on a kite have been estimated and described. Recapitulating there are four phenomena causing moments around the \mathbf{z}_B axis. First of all steer input causes the kite to twist (one wingtip moves forward) creating a moment around the \mathbf{z}_B axis. Secondly a side slip angle causes a difference in force resulting in a rotating moments. Thirdly there is a damping moment, when the kite starts to turn a difference in apparent wind speed is experienced at the left and right tip. As a result a damping moment is formed. Finally there is a moment due to the fact that the center of gravity often does not lie on the axis of rotation. Therefore the gravitational force will cause a (small) moment. In Table 9 an impression and estimation of the moments is shown.

Based on aerodynamic theory the aerodynamic moments are described in the following form:

$$M_z = \frac{1}{2} \rho_{air} A_{kite} b |\mathbf{v}_{App}|^2 C_Z \quad (6-27)$$

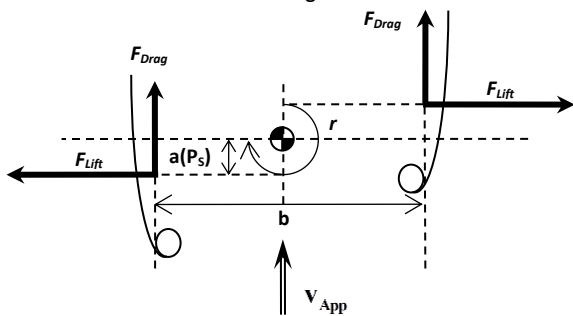
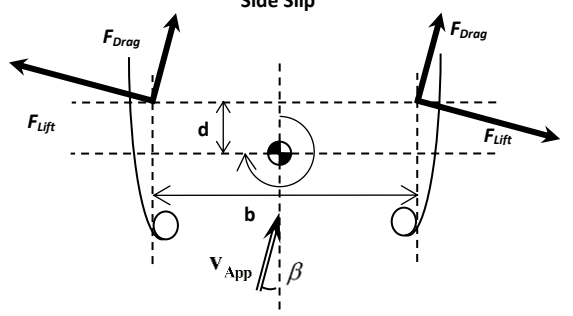
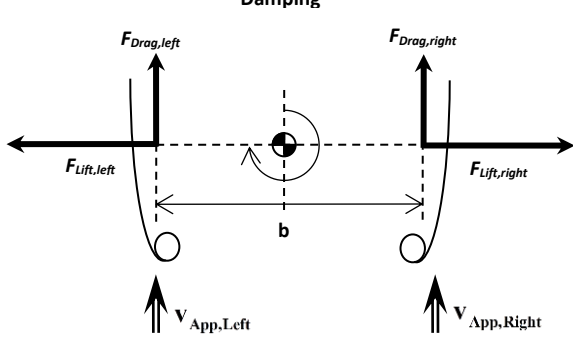
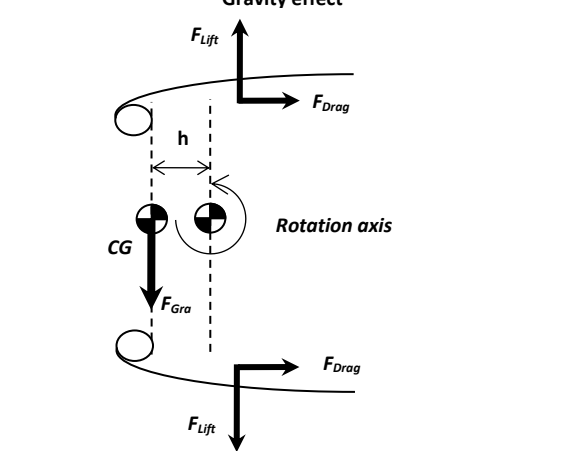
Illustration	Moment Equations
<p style="text-align: center;">Steering</p> 	$M_{Steer} = a(P_s)(\mathbf{F}_{Lift,left} + \mathbf{F}_{Lift,right}) + \frac{1}{2} b (\mathbf{F}_{Drag,left} - \mathbf{F}_{Drag,right})$ $M_{Steer} = 2a(P_s) \mathbf{F}_{Lift} = a(P_s) \rho_{air} A_{side} \mathbf{v}_{App} ^2$ $C_{Z_{a(P_s)}} \approx \frac{M_{Steer}}{\frac{1}{2} \rho_{air} A_{kite} b \mathbf{v}_{App} ^2} = 2 \frac{A_{side}}{A_{kite}} \frac{1}{b} a(P_s)$
<p style="text-align: center;">Side Slip</p> 	$M_{SideSlip} = d \cos(\beta)(\mathbf{F}_{Lift,right} - \mathbf{F}_{Lift,left}) + d \sin(\beta)(\mathbf{F}_{Drag,left} + \mathbf{F}_{Drag,right}) \dots$ $+ \frac{1}{2} b \cos(\beta)(\mathbf{F}_{Drag,left} - \mathbf{F}_{Drag,right}) + \frac{1}{2} b \sin(\beta)(\mathbf{F}_{Lift,left} + \mathbf{F}_{Lift,right})$ $M_{SideSlip} \approx \sin(\beta)(2d \mathbf{F}_{Drag} + b \mathbf{F}_{Lift})$ $\sin(\beta) \approx \beta \text{ (for } \beta < 15^\circ \text{)}$ $M_{SideSlip} \approx \beta \frac{1}{2} \rho_{air} A_{side} \mathbf{v}_{App} ^2 (2d C_D + b C_L)$ $C_{Z_\beta} \approx \frac{M_{SideSlip}}{\frac{1}{2} \rho_{air} A_{kite} b \mathbf{v}_{App} ^2} = \left(\frac{2d}{b} C_D + C_L \right) \frac{A_{side}}{A_{kite}} \beta$
<p style="text-align: center;">Damping</p> 	$M_{Damping} = \frac{1}{2} b (\mathbf{F}_{Drag,left} - \mathbf{F}_{Drag,right})$ $\mathbf{v}_{App,Left} = \mathbf{v}_{App} - \frac{1}{2} b r$ $\mathbf{v}_{App,Right} = \mathbf{v}_{App} + \frac{1}{2} b r$ $M_{Damping} = -\frac{1}{2} \rho_{air} A_{side} C_D b^2 r \mathbf{v}_{App}$ $C_{Z_r} \approx \frac{M_{Damping}}{\frac{1}{2} \rho_{air} A_{kite} b \mathbf{v}_{App} ^2} = -C_D \frac{A_{side}}{A_{kite}} \frac{b r}{ \mathbf{v}_{App} }$
<p style="text-align: center;">Gravity effect</p> 	$M_{Gravity} = h \left(\text{proj}_{(XY)_B} \mathbf{F}_{Gra} \cdot \mathbf{y}_B \right)$ $C_{Z_d} \approx \frac{M_{Gravity}}{\frac{1}{2} \rho_{air} A_{kite} b \mathbf{v}_{App} ^2} = \frac{2h \left(\text{proj}_{(XY)_B} \mathbf{F}_{Gra} \cdot \mathbf{y}_B \right)}{\rho_{air} A_{kite} b \mathbf{v}_{App} ^2}$

TABLE 9, MOMENT AROUND TETHER

In Table 9 the components of the aerodynamic coefficient C_Z are estimated. Based on the analysis the following relation for C_Z is found:

$$\begin{aligned}
 C_Z &= C_{Z_{a(P_s)}} a(P_s) + C_{Z_\beta} \beta + C_{Z_r} \frac{br}{|\mathbf{v}_{App}|} + C_{Z_d} \frac{2(\text{proj}_{XY_B} \mathbf{F}_{Gra} \cdot \mathbf{y}_B)}{\rho_{air} A_{kite} b |\mathbf{v}_{App}|^2} \\
 C_{Z_{a(P_s)}} &\approx 2 \frac{A_{side}}{A_{kite}} \frac{1}{b} \\
 C_{Z_\beta} &\approx \left(\frac{2d}{b} C_D + C_L \right) \frac{A_{side}}{A_{kite}} \\
 C_{Z_r} &\approx -C_D \frac{A_{side}}{A_{kite}} \\
 C_{Z_d} &\approx h
 \end{aligned} \tag{6-28}$$

An identical relation for C_Z has also been described in the paper of Houska [48] en de Groot [45] supporting this analysis. However they defined the relation in an intuitive way.

The aerodynamic coefficients of (6-28) have not been fitted yet. It's doubtful if the current measurements are accurate enough to find a correct fit. Due to the limited time this analysis is postponed. The moments are nevertheless implemented in the model and the complete model is compared with test data in chapter 8. The values are estimated based on the analysis in Table 9. The following coefficients are used

$C_{Z_{a(P_s)}}$	0.032
C_{Z_β}	0.091
C_{Z_r}	-0.018
C_{Z_d}	0 (unknown)

TABLE 10, AERODYNAMIC COEFFICIENTS

The third level contains all equations to determine $\dot{\mathbf{X}}(t)$. The system is divided in three sections. The first section determines all variables and rotation matrixes needed to calculate the forces on the kite. The second section calculates the forces and moments of the kite. Finally in the third section $\dot{\mathbf{X}}(t)$ is composed out of all variables.

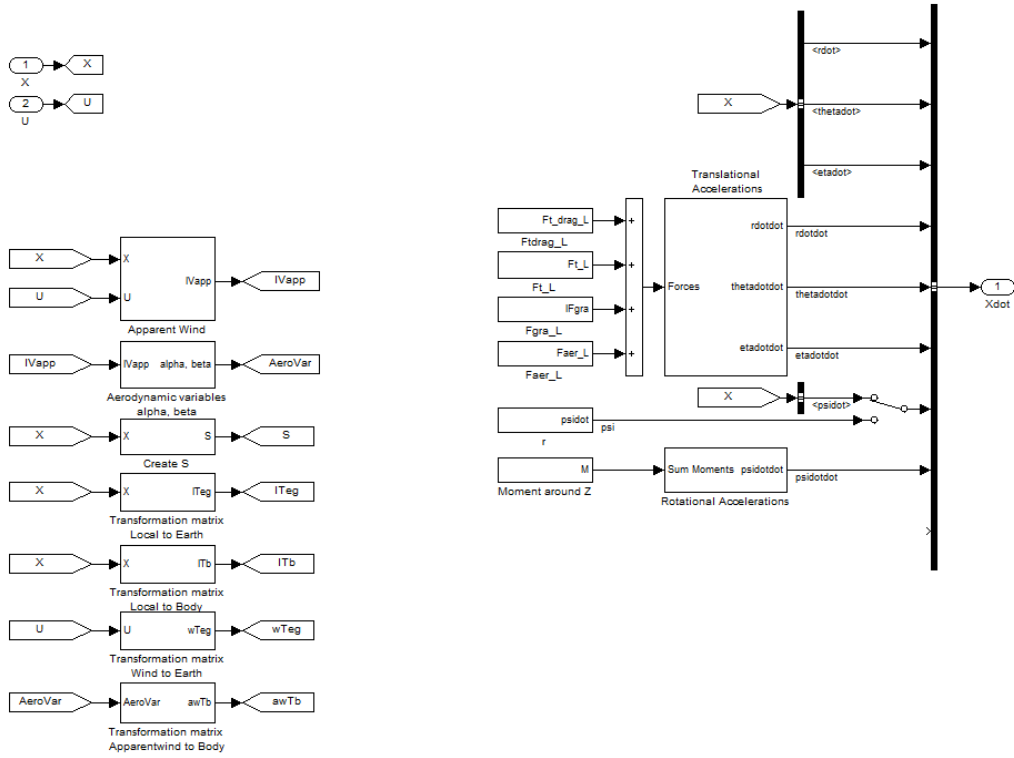


FIGURE 6-5, SYSTEM EQUATIONS

7 TETHER MODEL

In the system identification the effects of tether sag and pod dynamics were studied. In the data clearly some effects of the tether sag could be seen however both effects were quite small. Nevertheless even small changes in angle of attack could result in different aerodynamic forces. Beside that the effect of tether sag becomes bigger with longer cables and increasing wind conditions. Therefore a tether model is integrated to see whether a tether model simulates the cable sag and pod dynamics realistically. In this chapter first the different tether models described in the literature study are re-evaluated after which a tether model is elaborated and combined with the kite model.

7.1 MODEL OPTIONS

In the model described in chapter 6 the tether is modelled as a constraint or spring damper. The drag forces on the tether are estimated and added to the kite. This results in a computational efficient model however it does not simulate the dynamic behaviour of the tether. In the literature study three options are described which simulate the tether dynamically, the elastic and inelastic point mass tether models and the multi-body tether model. First of all the multi-body approach of Breukels [46] can be excluded. Breukels uses the multi-body approach mainly because he was working in the multi-body program Adams. Incorporation of a multi-body tether in Simulink would be very time consuming and would not add any information in addition to the point mass models (since a 4 mm Dyneema tether has almost no bending stiffness). This leaves two options, the elastic and inelastic point mass models. Both models have been assessed by Williams [59], he states the following advantages and disadvantages.

Elastic point mass model	Inelastic point mass model
<ul style="list-style-type: none"> + More easy and straight forward to incorporate + Equations of motion are inertially decoupled - Small time steps needed due to high stiffness of tether 	<ul style="list-style-type: none"> + Elimination of high frequency longitudinal oscillations + Reductions in simulation time - Reduction algorithms are needed to solve constraint

Williams eventually describes and uses an inelastic point mass model. He states that the performance is better than the elastic point mass model. For our kite power system model the incorporation of a inelastic point mass model would also be the most logic choice since the goal is real time modelling. There are however some practical problems: the implementation is time consuming and the reduction algorithm which Williams used in Simulink is difficult to implement. In addition an elastic point mass tether model developed by RTH Zurich [61] was available. This model was developed for numerical simulation of glider winch launches. Since the primarily goal of the tether model is to assess the need and validity of the discretised point mass tether model it was chosen to use the elastic tether model of RTH Zurich as a starting point and develop a reeling elastic point mass model.

7.2 DISCRETISED POINT MASS TETHER MODEL

7.2.1 DYNAMIC EQUATIONS

The Simulink model of RTH Zurich is based, surprisingly, on the work of Williams. However instead of inelastic rods the tether segments are modelled as springs (Hooke's law) together with a damping term. The tether model is shown in Figure 7-1.

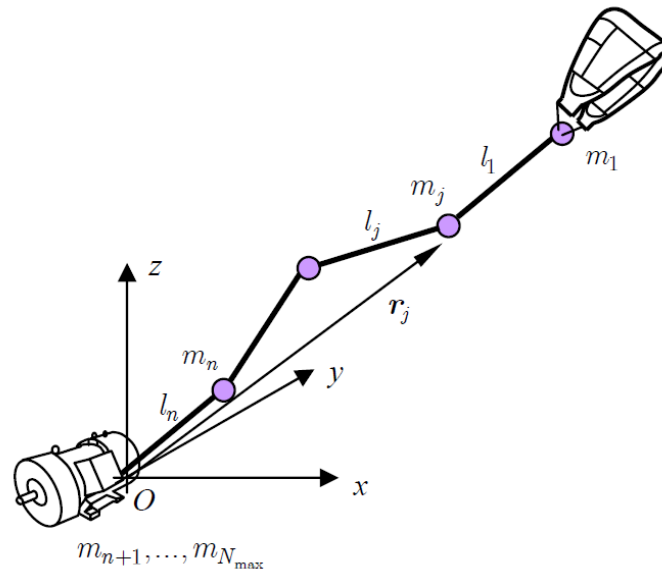


FIGURE 7-1, POINT MASS TETHER MODEL [59]

As our inertial frame the earth-groundstation reference frame, EG , will be used as shown in Figure 4-1. The generator is placed at the origin. The tether is modelled as a series of n point masses connected via spring dampers. The numbering is such that the mass 1 is the kite, mass 2 is the steering pod, which is modelled separately, and the rest of the masses are tether elements. The model is implemented in such a manner that different number of tether elements could be freely chosen. More elements results in a more accurate model however the differential equations become stiffer due to the shorter length of the springs. A balance has to be found between simulation speed and accuracy.

The masses are defined as:

$$\begin{aligned}
 m_1 &= m_{kite} \\
 m_2 &= m_{pod} + \frac{1}{2} \rho_{tether} \frac{1}{4} \pi d_T^2 l_0 \\
 m_{3-n} &= \rho_{tether} \frac{1}{4} \pi d_T^2 l_0 \\
 m_n &= \frac{1}{2} \rho_{tether} \frac{1}{4} \pi d_T^2 (l_{0,j-1} + l_{0,j})
 \end{aligned} \tag{7-1}$$

Where ρ_{tether} is the tether mass density, d the diameter and l_0 the unstretched length of the tether segments. The position vector of all masses in the inertial frame is denoted by $\mathbf{R}_j \in \mathbb{R}^3$. The equation of motion for the j th mass is determined in a straightforward manner by Newton's second law:

$$m_j \ddot{\mathbf{R}}_j = \mathbf{F}_j \tag{7-2}$$

On the masses four forces are acting which have to be defined. The tension from the tether elements after and before the mass, the aerodynamic drag and a gravity force, see Figure 7-2.

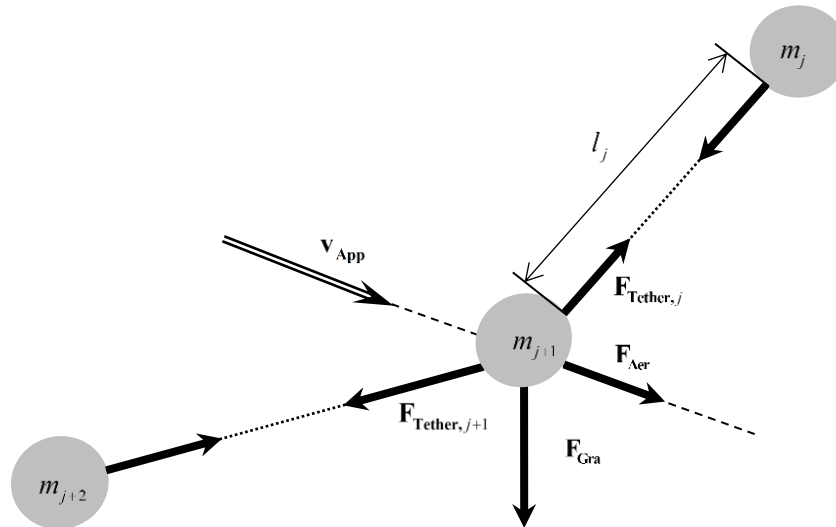


FIGURE 7-2, FORCES ACTING ON MASS

SPRING DAMPER FORCES

The tension in the tether is modelled by spring dampers.

$$F_{Tether,j} = \begin{cases} -k(l_j - l_0) - cl_j & \text{for } (l_j - l_0) \geq 0 \\ 0 & \text{for } (l_j - l_0) < 0 \end{cases} \quad (7-3)$$

Where l_j is the distance between two consecutive masses, l_0 the rest length, i.e. unstretched length, of the tether segments k is the spring constant and c is a strain-speed proportional damping constant. The direction of the $F_{Tether,j}$ is in the direction of the previous mass:

$$\mathbf{F}_{Tether,j} = F_{Tether,j} \frac{\mathbf{R}_j - \mathbf{R}_{j+1}}{|\mathbf{R}_j - \mathbf{R}_{j+1}|} = F_{Tether,j} \frac{\mathbf{r}^{j,j+1}}{|\mathbf{r}^{j,j+1}|} \quad (7-4)$$

Where $\mathbf{r}^{j,j+1}$ is the vector from mass j to mass $j+1$. The distance $l_j = |\mathbf{r}^{j,j+1}|$.

The spring constant k is defined as:

$$k = \frac{E_T A_T}{l_0} = \frac{k_0}{l_0} \quad (7-5)$$

Note that k is dependent on the tether segment length. In many papers therefore the unit spring constant k_0 is used. For the damping constant the same applies. The unit damping constant is defined as c_0 and the damping coefficient is defined as:

$$c = \frac{c_0}{l_0} \quad (7-6)$$

In section 7.3 the unit spring constant and damping constant of Dyneema are determined by experiment.

GRAVITY FORCES

The gravity force is determined by:

$$\mathbf{F}_{\text{Gra}} = m_j \mathbf{g} \quad (7-7)$$

AERODYNAMIC FORCES

The aerodynamic force is derived by splitting the force up into two components, the aerodynamic force tangential to the line and one perpendicular to it. Values of these two components are given by the following formulas [59].

$$\begin{aligned} \mathbf{F}_{\perp \text{Aer}} &= \frac{1}{2} \rho_{\text{air}} d_T l_0 C_{\perp D, T} |\mathbf{v}_{\perp \text{App}}| \mathbf{v}_{\perp \text{App}} \\ \mathbf{F}_{\parallel \text{Aer}} &= \frac{1}{2} \rho_{\text{air}} d_T l_0 C_{\parallel D, T} |\mathbf{v}_{\parallel \text{App}}| \mathbf{v}_{\parallel \text{App}} \end{aligned} \quad (7-8)$$

Where $C_{\perp D, T}$ is the normal drag coefficient of the tether and $C_{\parallel D, T}$ the friction drag coefficient. Usually $C_{\perp D, T} \gg C_{\parallel D, T}$ and the friction coefficient is neglected. The wind speeds $\mathbf{v}_{\parallel \text{App}}$ and $\mathbf{v}_{\perp \text{App}}$ are the tangential and normal component of the apparent wind relative to the tether. The apparent wind speed is obviously evaluated at the point mass which is under question.

$$\begin{aligned} \mathbf{v}_{\text{App}} &= \mathbf{v}_{\text{Wind}}(z) - \frac{\dot{\mathbf{R}}_j + \dot{\mathbf{R}}_{j+1}}{2} \\ \mathbf{v}_{\perp \text{App}} &= \mathbf{v}_{\text{App}} - (\mathbf{v}_{\text{App}} \cdot \mathbf{r}^{i, j+1}) \mathbf{r}^{i, j+1} \\ \mathbf{v}_{\parallel \text{App}} &= \mathbf{v}_{\text{App}} - \mathbf{v}_{\text{App}, \perp} \end{aligned} \quad (7-9)$$

7.2.2 TETHER REELING

In the pumping kite model the tether is continuously reeled in or out. Therefore the tether model should be able to increase or decrease its length on demand. Since the tether is discretised as lumped masses connected with spring dampers the modelling of such a various length tether model is rather difficult. Tether elements, i.e. masses, have to be added or subtracted at the winch to simulate the reeling. This should be done in a smooth manner without producing unrealistic tether oscillations. Moreover additional masses add degrees of freedom to the system. Most numerical solvers cannot handle variable length state vectors, and therefore a work around is often needed.

As a starting point for our tether model the Simulink model of the RTH Zurich is used. In Simulink it is not possible to change the size of the state vector during the simulation. Therefore the tether is discretised in a fixed number of elements to overcome this problem. When the tether segments are reeled in the masses are 'fixed' to the winch. So the length of the state vector stays constant. The reeling algorithm in the tether model of RTH Zurich was only able to simulate reeling in of tethers (since it was developed for glider winch launches). Besides that small unrealistic tether oscillations were present in the model due to programming faults. To overcome these deficiencies the following reeling procedure was implemented, based on the work of Williams [59].

REELING OUT

In general the reeling is simulated by changing the rest length l_0 of the spring which connect the last mass to the winch. By changing the length l_0 the spring length changes simulating a longer or shorter tether. However at a certain point the length becomes too big or small for realistic modelling and a mass has to be added or subtracted.

The largest challenge is modelling the reeling out of the tether. In this case a mass and spring damper element have to be added to the tether. The mass cannot be introduced at the ground because a small spring-damper length would result in a very stiff spring-damper and very small step sizes. To overcome this problem the new mass is introduced somewhere in between the mass closest to the winch and the winch. However to prevent oscillations the mass should be introduced at precisely the correct position. Also the spring rest length of the last two springs has to be set exactly right. Figure 7-3 shows the successive steps.

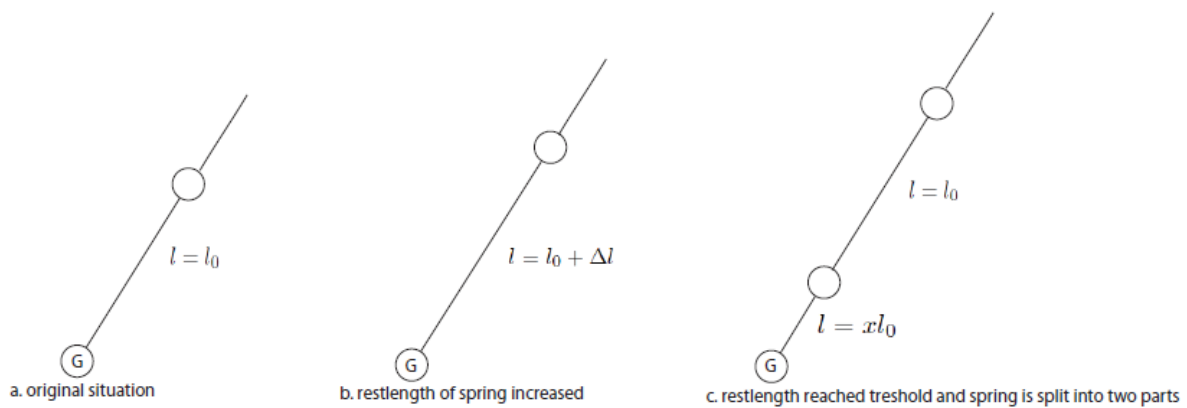


FIGURE 7-3, REELING OUT OF TETHER

First the rest length l_0 is increased depending on the reeling speed of the winch till a certain threshold length is reached $l_0 > l_{threshold}$ at which the spring is split into two parts and a new mass particle is placed in between. The spring is split in such a way that the rest length of the upper part has the original rest length l_0 and that the tether tension force on the old mass stays equal (to prevent unrealistic tether oscillations). The old mass, so to speak, must not be aware of the newly added mass. To reach this the mass is placed in between the two particles at a distance:

$$\mathbf{R}_{j+1} = \left| \mathbf{R}_j \right| \frac{1 - l_{0,j}}{l_{0,j+1} + l_{0,j}} \frac{\mathbf{R}_j}{\left| \mathbf{R}_j \right|} \quad (7-10)$$

The mass should also have an initial speed, to correctly evaluate the damping term. The speed of the new particle is defined as:

$$\dot{\mathbf{R}}_{j+1} = \dot{\mathbf{R}}_j - \mathbf{v}_L \left(1 - \frac{l_0}{l_{0,j+1}} \right) + \mathbf{v}_L \quad (7-11)$$

The length of the new spring should also be defined correctly. The tension in the new tether segment should be equal to the old segment. This is accomplished by defining

$$l_{0,j+1} = l_{0,j} - l_0 \quad (7-12)$$

Worth mentioning is that due to the change in rest length also the spring constant, damping constant and mass defined in (7-1), (7-5) and (7-6) change.

REELING IN

Reeling in is basically the reverse procedure. In

Figure 7-4 the steps are displayed.

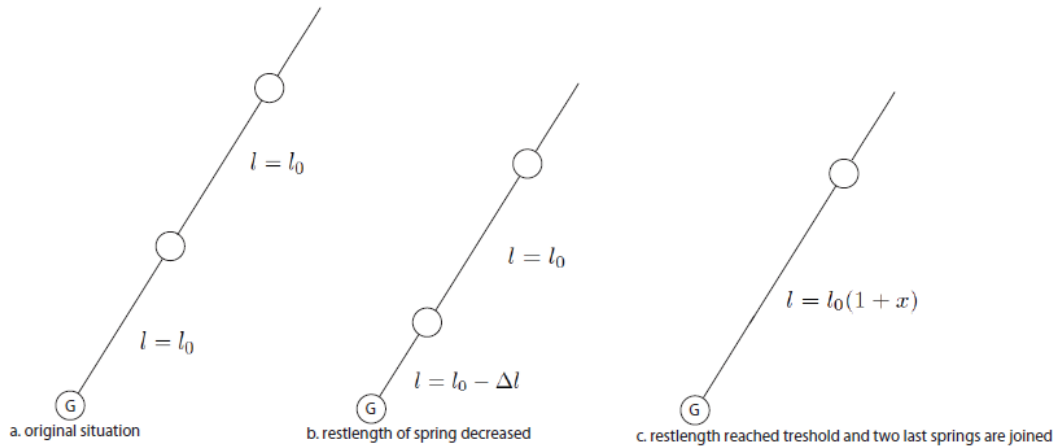


FIGURE 7-4, REELING IN OF TETHER

The rest length l_0 is decreased on the reeling speed of the winch till a certain maximum rest length is reached $l_0 < l_{\max}$. When the maximum rest length is reached the mass closest to the winch is removed, which in our case means fixed to the ground station. The rest length of the new last spring is defined in such a way that the forces on the new last mass stay the same. The rest length can be calculated with

$$l_{0,j-1} = l_{0,j} + l_{0,j-1} \quad (7-13)$$

7.3 DYNEEMA PROPERTIES

For realistic simulation the spring and damping coefficient of the Dyneema tether are needed. Currently the spring constant is deduced from the theoretical elasticity of Dyneema and the damping constant is guessed (often 10% of the elasticity). To find the spring and damping coefficient of the Dyneema tether an experiment was carried out using the method described by Hamilton [75]. The experiment is described in Appendix F: and Figure 7-5 shows the test setup. The test consists out of the linear excitation of the tether. From the frequency and the damping of the forces in the tether the unit spring and damping coefficients of Dyneema could be extracted. The test resulted in the following coefficients.

$$k_0 = 6.1462 \pm 0.0176 \times 10^5 \text{ (1}\sigma\text{) N}$$

$$c_0 = 473 \pm 23 \text{ (1}\sigma\text{) Ns}$$

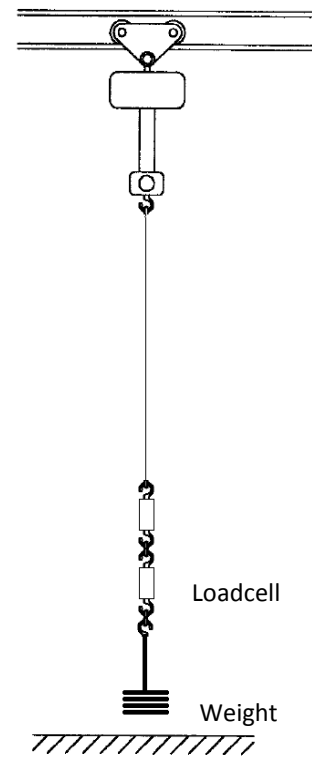


FIGURE 7-5, TEST SETUP

7.4 VALIDATION OF TETHER MODEL

To completely validate the tether model is quite difficult. To validate the tether model the shape of the tether and the apparent wind speed at the tether has to be known, ideally in a dynamic situation. This is difficult and outside the scope of this thesis. Nevertheless some simple test could be performed to check the correct implementation of the tether model and study the behaviour of tethers. Three tests were performed with the tether model. First the tether model is compared with a catenary line, secondly a cable hanging in the wind is simulated and compared finally the test described in section 7.3 is compared with reality.

CATENARY

To check the developed tether model the numerical simulated tether shape is compared to a catenary line. A 300 m tether is simulated which is composed out of 25 elements. Both ends are fixed on the x axis 300 m apart. As a result of the weight of the tether the tether will stretch and sag. At $t=0$ the tether is initiated as a straight line. Figure 7-6 shows the dynamic falling of the tether and Figure 7-7 shows the end position compared with a catenary line. The simulation is without wind. The catenary line is defined as:

$$z = a \cosh\left(\frac{x-150}{a}\right) - a \cosh\left(\frac{150}{a}\right) \quad (7-14)$$

Where

$$a = \frac{F_{tether}}{g \rho_{tether} A_T} \quad (7-15)$$

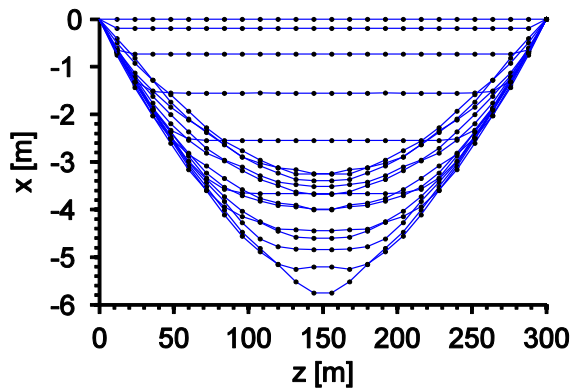


FIGURE 7-6, DYNAMIC FALLING OF THE TETHER

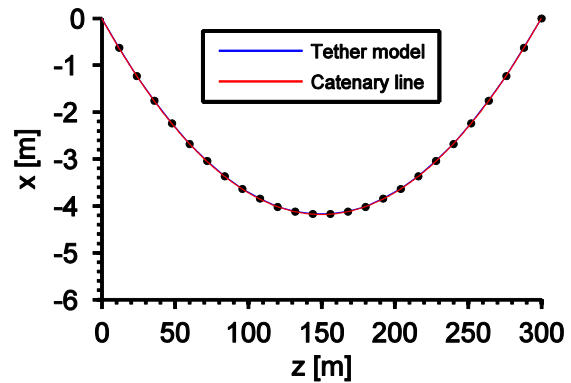


FIGURE 7-7, END POSITION AND CATENARY LINE

The plot shows that the profile of the simulated tether aligns to the catenary.

TETHER LINE INTO WIND

Secondary the same line of 300 m is vertically suspended at the top and bottom and a uniform wind of 6 m/s is blown in X direction. With this test is the effect of the wind shear is evaluated. The results are shown in Figure 7-8 and Figure 7-9.

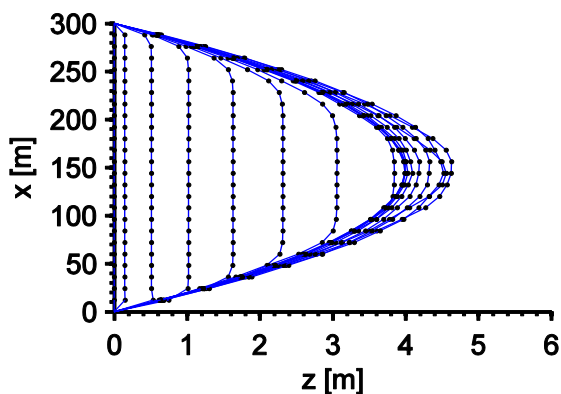


FIGURE 7-8, DYNAMIC TETHER WITH WIND

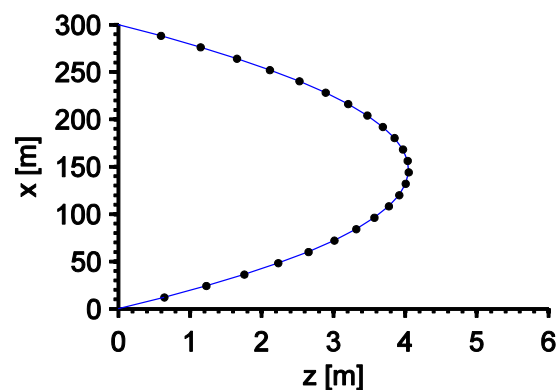


FIGURE 7-9, END POSITION OF TETHER IN WIND

The same simulation has been done by Baayen [60] and the results are identical. No test data is available of tether wind tunnel tests to validate the wind shear influence on the tether nevertheless the simulations appear realistic.

LINEAR EXCITATION

In section 7.3 an experiment was conducted to estimate the parameters of the Dyneema tether. As validation, the same experiment is performed in the discretised tether model and the results are compared. The test is very simple, no influence of tether drag, however it is still worth checking.

Identical to the test, a tether of 5.14m is composed out of 10 elements is vertically suspended. The end mass is set to 317.8kg to simulates the weight. At $t=0$ an additional mass of 10kg is added to the end mass. The forces in the spring connected to the last mass are displayed in Figure 7-10. The data of the real test are shown in Figure 7-11.

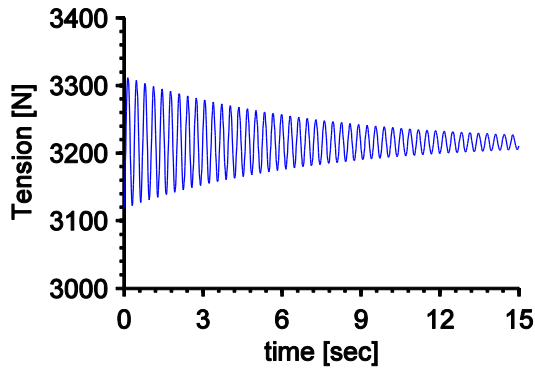


FIGURE 7-10, SIMULATION

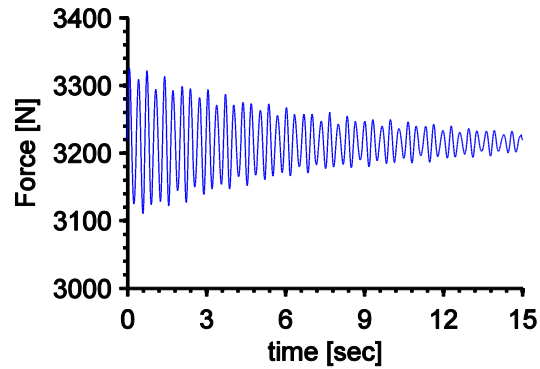


FIGURE 7-11, EXPERIMENTAL DATA

The forces are almost identical. In the real test data an secondary frequency can be seen. In Appendix F: it is explained that this is probably due to the swinging natural frequency of the weight.

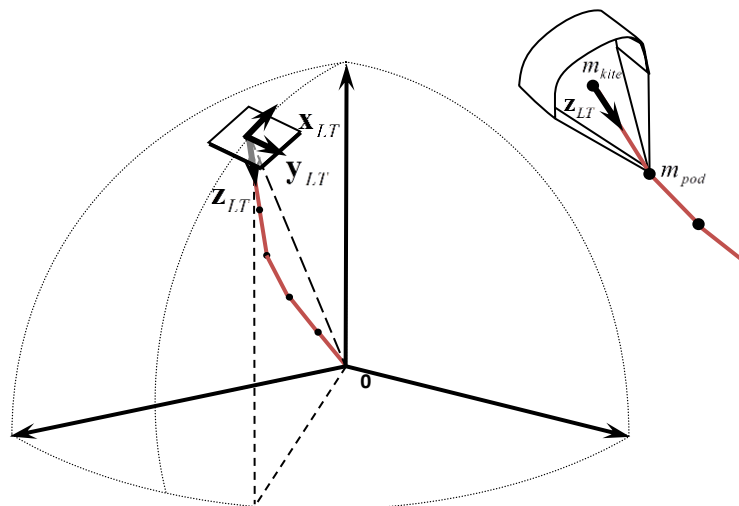
7.5 INTEGRATION WITH KITE MODEL

The kite model is coupled to the tether model. Since the kite model developed in chapter 6 is based on a point mass the linking is done by replacing the last mass of the tether by the kite, and the second last mass with the pod. Equivalent to the kite model with a straight tether the external forces act on the mass. However the orientation of the kite has to be redefined. In chapter 6 the local reference frame L was used to determine the orientation and forces of the kite. The local reference frame is the tangential plane of a unit sphere and is always normal to the tether. However due to the tether model the tether is able to sag and the local reference frame inadequate. As a result a new local reference frame has to be defined. The frame has to be normal to the tether and in addition it is beneficial to define the new x axis pointing to Small-North (see Figure 4-2) corresponding to the x_L axes. The prevent mix-up the new reference frame is called the local tether frame, LT and is constructed in the following way:

The vector $\mathbf{r}^{1,2}$ points from the last mass to the second last mass, which are the kite and pod respectively and forms the new \mathbf{z}_{LT} axes. A normal plane is constructed by:

$$\begin{aligned} \mathbf{y}_{LT} &= \mathbf{z}_{LT} \times \mathbf{z}_{EG} \\ \mathbf{x}_{LT} &= \mathbf{z}_{LT} \times \mathbf{y}_{LT} \end{aligned} \quad (7-16)$$

The frame is shown in Figure 7-12

FIGURE 7-12, LT REFERENCE FRAME

Similar to the kite model in chapter 6 a body reference frame is defined by turning the local tether frame by an angle $\psi^{LT,B}$ around the \mathbf{z}_{LT} axis.

With the local tether frame LT and the body defined the aerodynamic force could be calculated identical to the kite model in chapter 6. The gravitational force, tether force and tether drag force are already taken into account in the tether model.

7.6 IMPLEMENTATION IN SIMULINK

The tether model is implemented in the software application Simulink for simulation. To make the model as clear as possible the model is split into various subsystems which are dispersed over 3 different modelling levels. The top level and the second level are equal to the tether model. The third level contains three sections. The first section determines all variables and rotation matrixes needed to calculate the forces on the kite. The second section calculates the aerodynamic forces and moments of the kite and the third section is the FEM tether model. A separate integrator is used for the rotational dynamics of the kite.

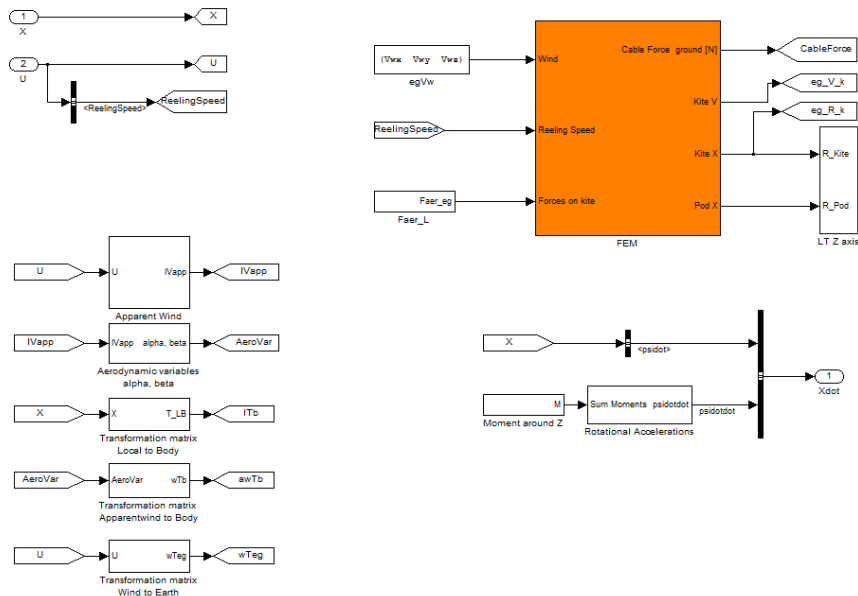


FIGURE 7-13, DISCRETIZED POINT MASS TETHER MODEL

8 RESULTS AND VALIDATION

The validation of the developed model is essential to assess the correctness and accuracy of the model. However, as already noticed in the literature study, validating of the developed model is difficult. Main difficulties lie in the fact that not all system states are measured or could be measured during test flights. The most important unknown variable remains the wind speed at the height of the kite. Measuring this wind speed is not possible. Besides that the accuracy of the IMU (X-Sence) and GPS sensors are fluctuating. Comparing the model with test data and express the accuracy of the model in numbers is therefore difficult. To overcome these difficulties the separate components of the kite model were based on an data analysis and system identification described in chapter 5 and are as a result to some extent checked. Nevertheless it is interesting to compare the complete model with test results. In this chapter the semi rigid body kite model is compared with a random cycle from a test day. The kite model is simulated with the straight spring damper tether model and the discretised point mass tether model.

The comparison is performed in the following manner, first of all the '2 lap' autopilot, a state machine and a simple winch model, were added to the developed kite models. The '2 lap' autopilot and state machine are described in the thesis of Jehle [71]. The winch model is a constant force P-controller with rate limits. This is obviously not very extensive, in the future more realistic winch model and winch controllers should be incorporated. Now is, in essence a full system model is achieved. By simulating the full system models with the same settings and wind speed as during the test day, theoretically the same results would be achieved. Due to small errors in the kite model, wind model, winch model or control algorithms the kite will eventually deviate from the test data. Nevertheless a comparison will show how long the kite model aligns with the test data. Further we could see if the model shows the same behaviour as the reel system. The comparison is more on a global basis, to see whether the model shows resemblance.

8.1 DATA SELECTION

A random cycle is selected from the test data of 14-6-2012 in order to perform the comparison. On this test date there was a low/medium wind of 4.4 m/s and the accurate Trimble GPS-sensor was available. One random cycle is picked from this day. The start of the cycle is selected at the point where the kite is in powered mode and crosses zero azimuth for the first time. The end point is in parking position at equal tether length. This way it is easy to synchronise the test data with both kite models. The parameters for the autopilot, winch controller and state machine of the selected cycle are displayed in Table 11 and used in both kite models. The wind input of the model is the wind speed measured at the ground corrected with the wind log law. The wind shear coefficient is iteratively found.

Start time (unix time)	1339694764.80 sec
Stop time (unix time)	1339694913.60 sec
Duration	148.8 sec
Average wind Speed (@6m/s)	4.4 m/s
Max tether length	400 m
Wind shear coefficient	0.05
Min tether length	270 m
Reel out force	1962 N (=200 kgf)
Reel in force	490 N (=50 kgf)
Depower pitch angle	40°
Controller settings A_η	7.5°
Controller settings A_ξ	15°
Controller settings η_0	25°
Tether length start	302 m
Tether length end	311 m

TABLE 11, PARAMETERS OF TEST DATA AND KITE MODELS, 14-6-2012

8.2 ALTERED LIFT CURVE

In the first simulations of the kite model the results were unrealistic. The kite was moving too fast and easily stalled. Most logically cause for this behaviour is an incorrect lift and drag curve. The lift and drag curves were derived in section 5.10 using the redefined crosswind law. Since the redefined crosswind law neglects inertia and weight effects, errors could easily occur. Also a incorrect estimation of the apparent wind speed could cause errors. In section 5.7 was already pointed out that estimated apparent wind speed has errors in the order of 1-4m/s. Both assumptions could easily lead to an incorrect lift and drag curves. After studying the L/D curve, Figure 5-26, it was assumed that the L/D ratio between 5 and 15 degrees was most likely estimated to high. In the future additional research is needed in the aerodynamic force model. To continue the validation of the kite model a slightly changed curve was proposed based on the data, own experience and theory. The curve shown in Figure 8-1 is used in the model.

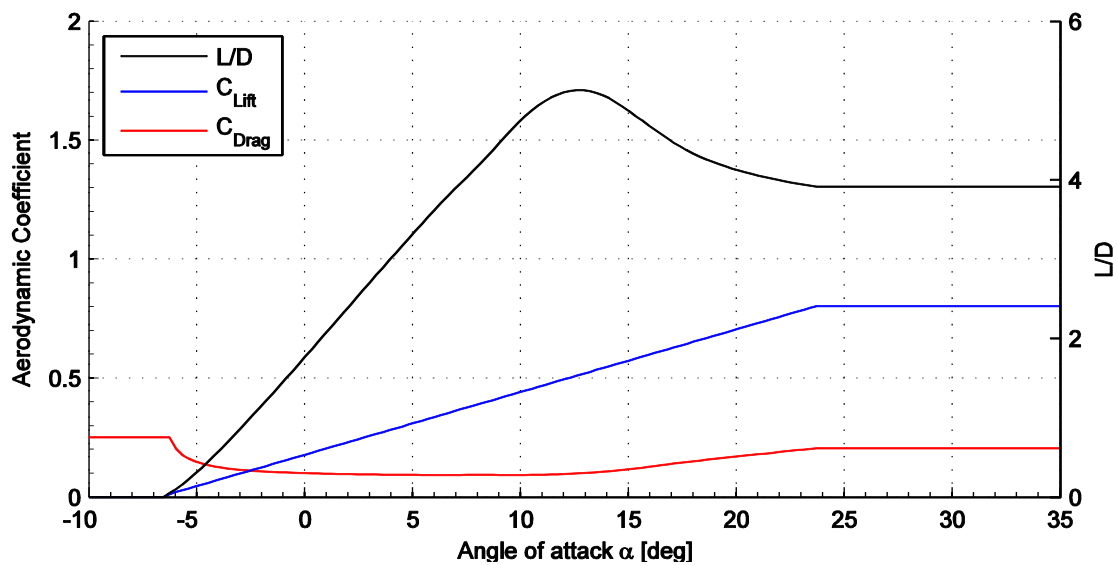


FIGURE 8-1, ALTERED LIFT AND DRAG CURVE

8.3 POSITIONS AND VELOCITIES

The two models were simulated with the altered lift and drag curves. Like stated before the two models are simulated with the same wind speed as during the test date. The starting points for the two models and the test data are identical. Figure 8-2 shows the trajectories of the test data and the two models.

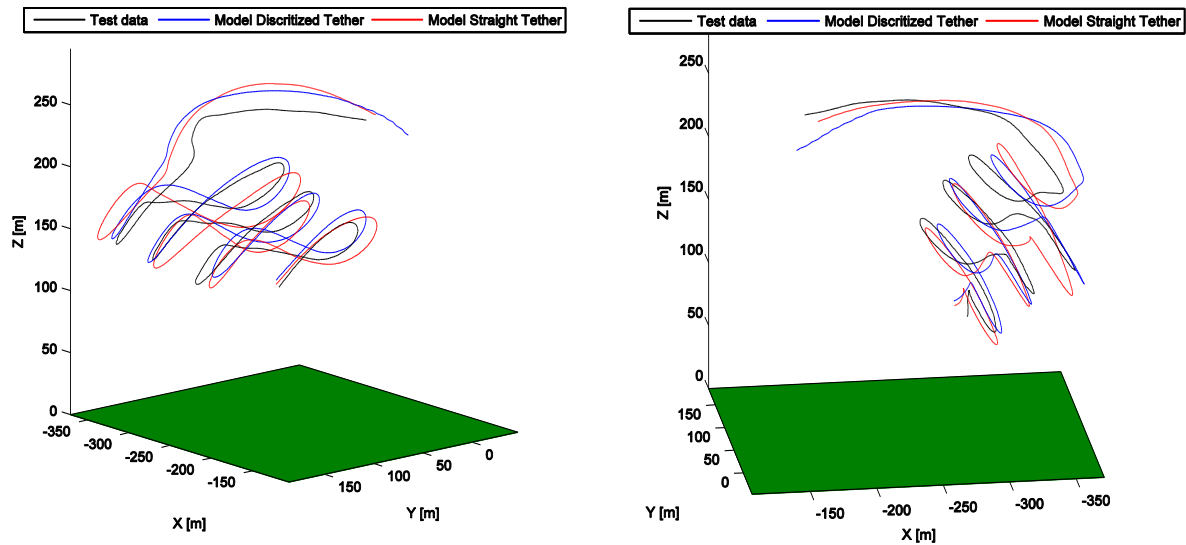


FIGURE 8-2, COMPARISON OF PATHS FLOWN

The three paths flown align quite good. For almost 150 seconds the trajectory of the models and trajectory from test data are almost equal. It is difficult to quantify this result however when considering the numerous possibilities which could lead to divergence off the path the results are above expectations and an indication of a correct implementation of all components. Errors in the kite model, wind model, winch model or control algorithms could easily result in a deviation of the path. It should be mentioned that the wind shear coefficient is to some extent fitted to make the path overlap. Different wind shear coefficients lead to different wind speeds at the kite and as a result the kite models would reel out faster or slower.

More important is the fact that due to the overlapping of the trajectories the other parameters could be compared. The kite velocity during the test day and the two models are plotted in Figure 8-3.

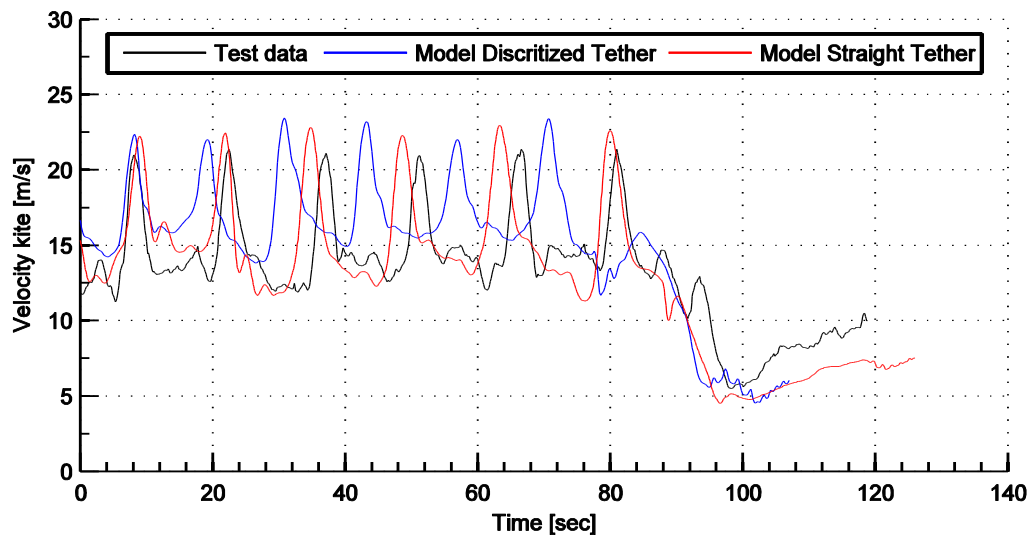


FIGURE 8-3, COMPARISON OF KITE VELOCITY

In the plot several things are noticed. First of all the velocities of both models are slightly higher than during the test day, especially the kite model with the discretised tether has a higher velocity which eventually results in the fact that a full cycle takes 15 sec less. Due to the higher speeds the downward loops are not flown exactly at the same time which leads to a time shift in the signals, as a result the peaks do not align perfectly. This time shift does not necessarily mean the model is incorrect. The downward loops are only flown at different times. The lift and drag curves and the weight of the kite are the main parameters influencing the kite speed. Most likely the drag of the discretised tether is defined too low. Overall the velocities correspond quite well indicating a correct implementation of all components.

8.4 FORCES AND REELING SPEED

The tether force is shown in Figure 8-4. Since the tether force is determined by the winch and winch controller the plot only shows the correct implementation of the winch controller.

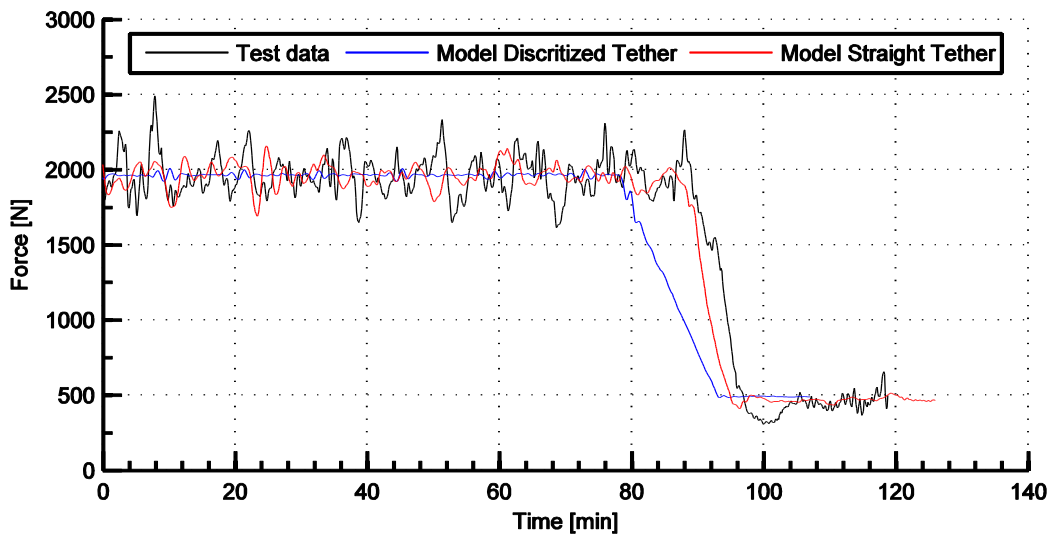


FIGURE 8-4, COMPARISON OF TETHER FORCES

The forces in the model are aligning with the test data demonstrating a correct implementation of the winch controller and winch model. As the wind, trajectory and forces are approximately identical the reeling speeds should also be roughly the same. In Figure 8-5 the reeling speeds are plotted.

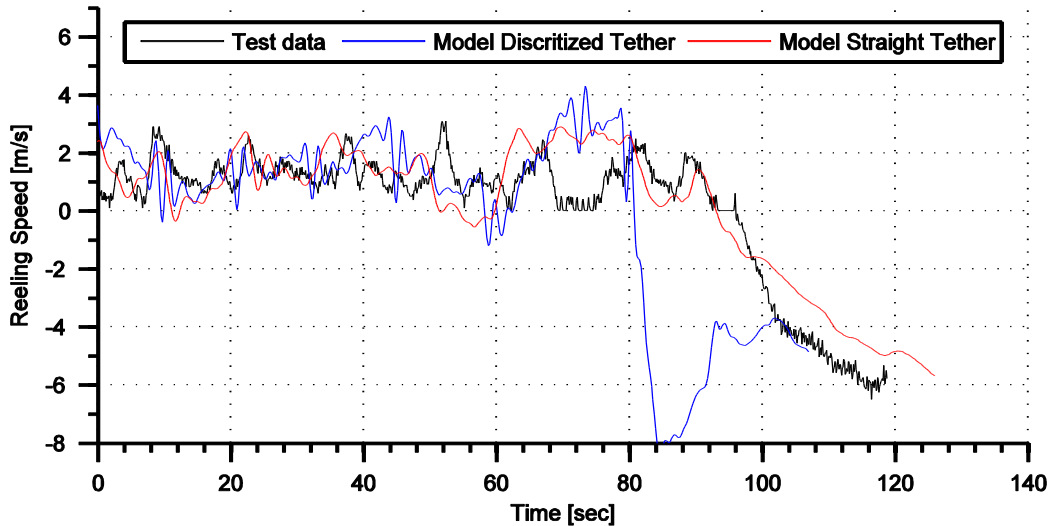


FIGURE 8-5, COMPARISON OF REELING SPEEDS

The figure shows that the reeling speeds are of a similar order. It should be noticed that the winch or winch controller from the discretised tether model is unrealistically during the transition from powered to depowered flight. The reeling speed drops too fast. Since the development of a realistic winch model was never the goal of this thesis, this is left to improve in future studies. Nevertheless the reeling speeds show representative behaviour.

8.5 POWER

The mechanical power from the test data and the two models is plotted In Figure 8-6.

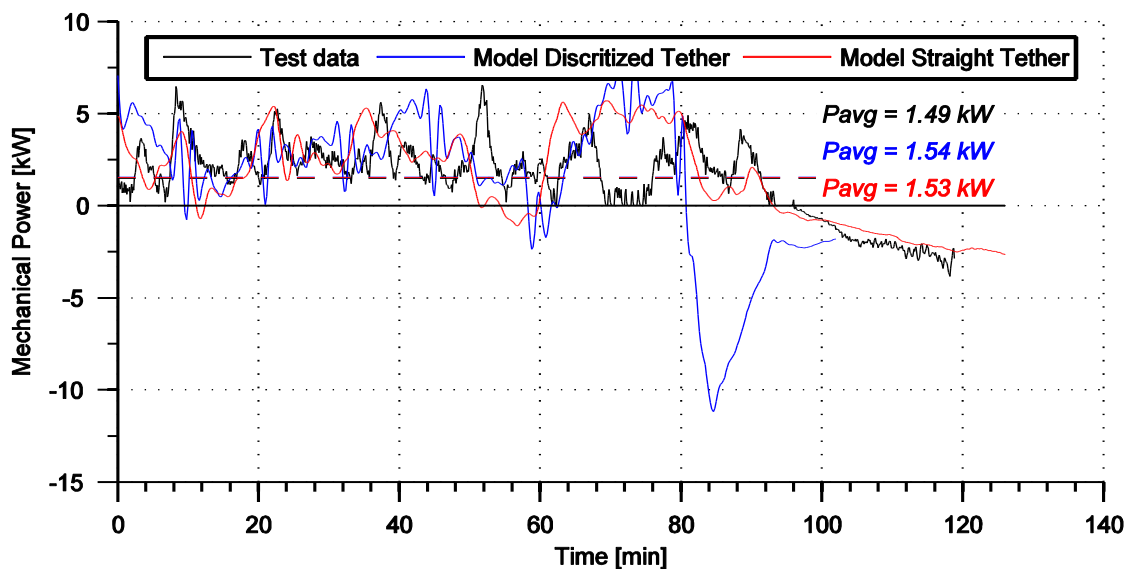


FIGURE 8-6, COMPARISON OF MECHANICAL POWER

Again the models shows resemblance with the measurement data. This could have been expected since the mechanical power is the result of the reeling speed and force, which corresponded quite well (section 8.4). More interesting to see is the fact that the mean power corresponds. This is essential for system performance and optimization studies which will probably be conducted in the future. The slightly higher mean power of both kite models could be explained by the slightly higher kite speeds (section 8.3).

8.6 ORIENTATION OF THE KITE RELATIVE TO THE TETHER

In section 5.5 the orientation of the kite relative to the tether was investigated. Small roll and pitch angles were found due to the pod dynamics and tether sagging. This was one of the reasons for the development of the discretised tether model. It is particularly interesting to see if the discretised tether kite model simulates the sagging of the tether and pod realistically. This is checked by performing a identical analysis as in section 5.5. The pitch angle relative to the tether is plotted in Figure 8-7.

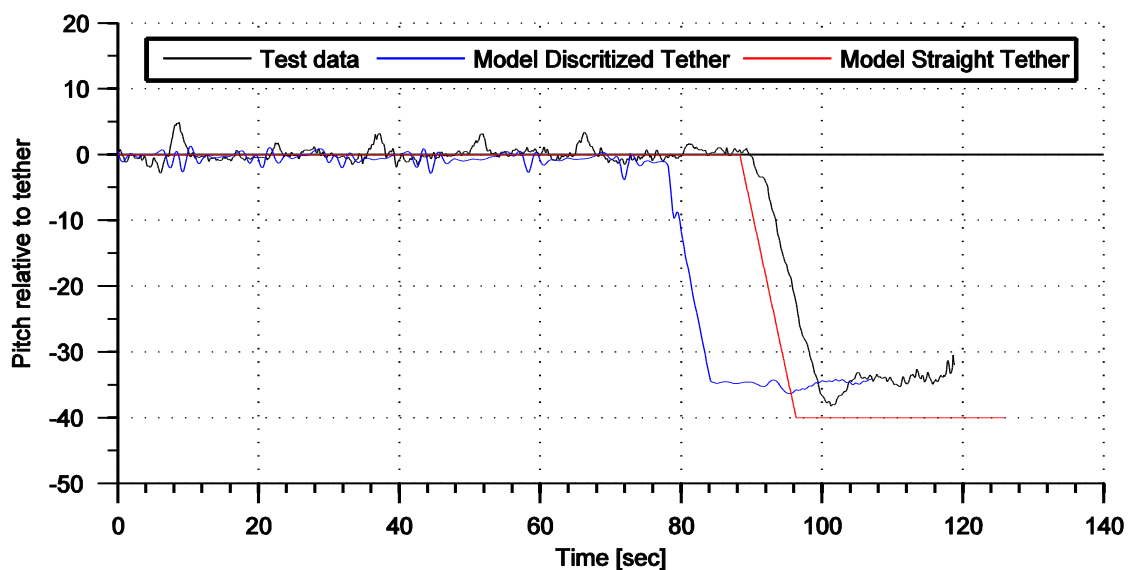


FIGURE 8-7, COMPARISON OF PITCH ANGLE

First thing noticeable is the correct implementation of the straight tether kite model. In the straight tether kite model the kite is by definition orthogonal to the tether. No dynamic pitch angles are therefore found. Only the pitching due to the depowering of the kite is visible. The pitch angle is directly controlled by the power setting.

The test data clearly show a small peak in the pitch angle each time the kite makes a downward turn. This is due to the dynamics of the pod and tether sagging (for more explanation see section 5.5 and Figure 5-10). To model these effects an additional discretised tether model was developed in chapter 7. In Figure 8-7 the developed discretised tether shows a similar pattern as the test data. Three small differences could be seen, the discretised tether model has smaller peaks, oscillates more and is sometimes shifted in time. The smaller peaks and oscillations are most likely the result of a too low drag coefficient of the tether. The time shift originates from the fact that the downward loops are not exactly flown at the same time. The plot clearly shows the correct implementation of the discretised tether model and its capability to simulate the dynamics of the tether.

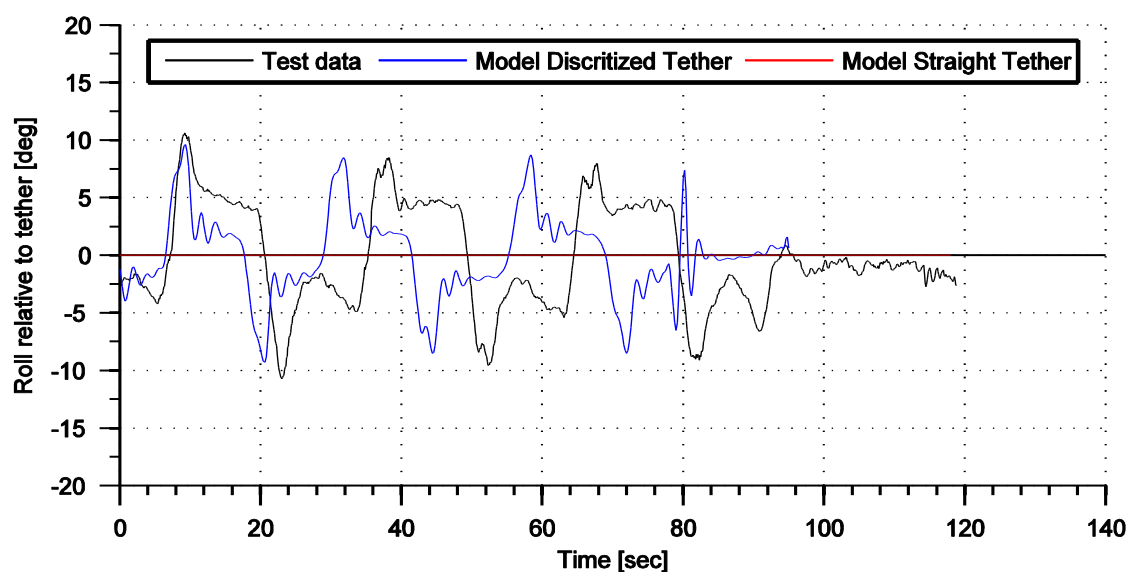


FIGURE 8-8, COMPARISON OF ROLL ANGLE

In Figure 8-8 the roll angle relative to the tether is shown. In the kite model with a straight tether the rolling around the tether is constrained, as a result a zero angle is found. The kite model with a discretised tether is able to simulate the pod dynamics and tether sag. The simulated roll angle nicely fits to the test data. Again slightly smaller angles are measured and a time shift is observed. As stated before the smaller angles are most likely the result of a too low tether drag coefficient.

8.7 ANGLE OF ATTACK AND SIDE SLIP ANGLE

Interesting to compare is whether the angle of attack and the side slip angles correspond with the measurement data. The aerodynamic force model depends on the angle of attack and therefore a correct estimation is important. It should be noted that the angle of attack of the test data depends on the definition of the cord line of the kite. With a different cord line the angle of attack is shifted up or down. So a direct comparison is difficult. Nevertheless the patterns could be studied and both models could be compared with each other. The angle of attack is plotted in Figure 8-9.

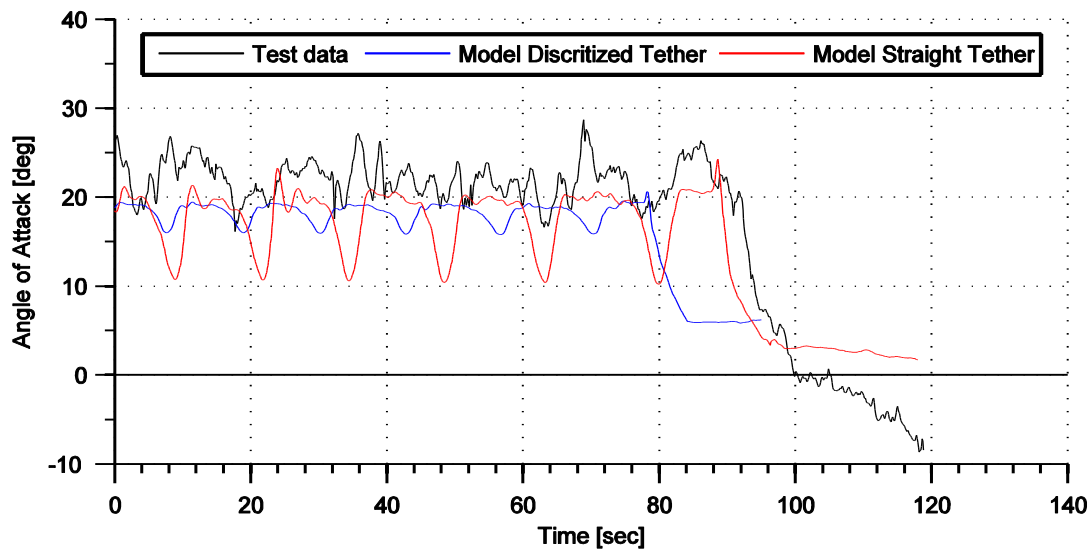


FIGURE 8-9, COMPARISON OF ANGLE OF ATTACK

First of all it should be observed that both models operate at an angle of attack around 20 degree but more interesting is to see the difference in angle of attack during the downward loop. The straight tether kite model has a large oscillation while the discretised tether model has only a small oscillation. This difference originates from the fact that the pod dynamics results in a higher pitch angle (see section 8.6) during the turns. The straight tether kite model does not simulate this effects and therefore a bigger oscillation is seen during the turns. Since the angle of attack is used in the aerodynamic force model the incorrect modelling of the angle of attack will most likely have an influence on the correct modelling of the system. A possible workaround for the straight tether kite model in future studies could be to define two fixed lift and drag coefficients, for powered and depowered flight respectively, instead of a lift and drag curve. Especially since the kite has a fairly constant angle of attack during straight flight.

The side slip angle of the test data and the two models are plotted in Figure 8-10. The side slip angle is particularly interesting as it indicates a correct implementation of the rotation moments and side force.

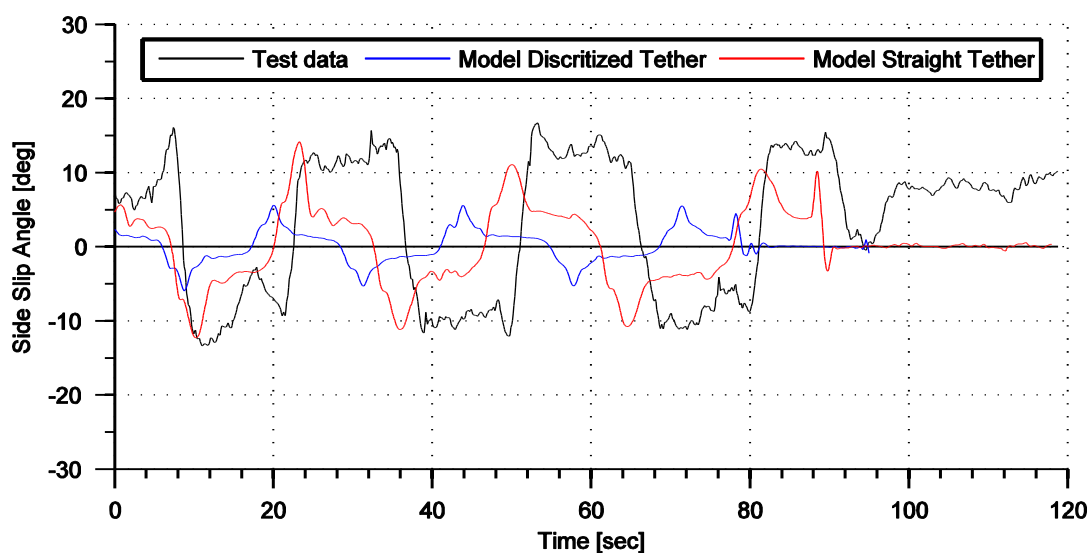


FIGURE 8-10, COMPARISON OF SIDE SLIP ANGLE

From all comparisons performed Figure 8-10 clearly shows the least resemblance between the lines. In all three lines a similar square wave pattern could be found nevertheless the angles are smaller in both kite models. The most likely cause for this is a too high coefficients for the side force or rotations moments.

8.8 STEER INPUTS

Finally it is interesting to compare the steer input from the developed model with test data. In Figure 8-11 the steer inputs of the model and test data are plotted.

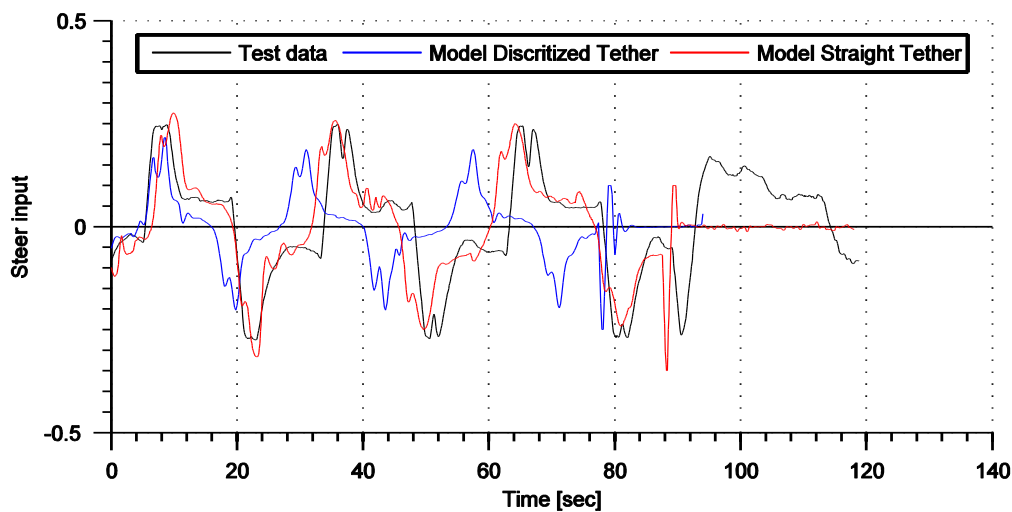


FIGURE 8-11, COMPARISON OF STEER INPUT

The steer inputs have the same appearance. The time shift in the signals, as stated before (section 8.6), is due to the fact that the kite makes the downward loops not exactly at the same time. The similarity between the steer inputs is particularly important since it is a good indication that the side forces and rotation moments are incorporated correctly. Section 8.7 also provided an indication of the correct implementation of the side forces and rotation moments however the autopilot could hide the effect of a wrong implementation. By comparing the steer inputs this effect is excluded.

8.9 SIMULATION TIME

One of the requirements of the developed kite model is that the model should simulate the kite in real time. This implies that the time to calculate a simulation step is smaller than the simulation step itself. The requirement to run in real time eventually led to the development of a semi-rigid kite model. Based on the simulations the simulation speeds could be assessed. The time needed for a simulation step also depends on the computational power. Therefore a normal desktop computer available at the TU Delft is used as a reference³.

The solver influences the simulation speeds. Currently a simple explicit fixed-step solver Ode3 (Bogacki-Shampine) is used. In Simulink multiple solvers are available and could be selected. However it should be kept in mind that the discretised tether model creates discontinuities in the model when masses are added or subtracted. Advance solvers will most likely have problems with these discontinuities. The Ode3 explicit fixed-step solver was able to correctly simulate the discretised tether model. For the comparison both models are simulated with the Ode3 solver.

The time step of the solver is currently determined in an iteratively manner. The time step has to be as large as possible without compromising the stability of the model. Both models prove to be stable with these settings. Further research is needed to optimise the solver. In Table 12 the performance of both models is shown.

³ Intel Duo Core processor E4400 (@2.00 GHZ) and 2GB RA.M

	Straight spring damper tether	Discretised point mass tether
Time modelled	300 sec	300 sec
Solver	Ode3	Ode3
Time Step	0.0666 sec	0.001 sec
Number of evaluations	4500	300000
Simulation time	38.14 sec	590.58 sec
Real-time	7.86	0.51

TABLE 12, SIMULATION SPEED

The developed semi-rigid body kite model could run in real time with a straight spring damper tether model. Currently it runs approximately 7 times faster than real time and the simulation speed could be further improved. The semi-rigid body kite model with a discretised tether is not able to run in real time. This is due to the discretised tether model which is highly nonlinear and stiff and therefore requires small time steps. This was expected beforehand. Nevertheless the tether model showed realistic behaviour and could be improved in future research.

9 CONCLUSIONS

Goal of this thesis is the development and validation of a real time pumping kite model. This task is split up in four parts, a literature study in chapter 2, a data analysis and system identification in chapter 5, the development of two kite models in chapter 6 and 7 and the validation of the models in chapter 8.

From the literature study it was concluded that most of the current models described in literature are not able to run in real time. The models which do meet this requirement are the point mass model and the (semi-) rigid body model. An analytic model is also capable of describing the performance of the kite in real time however it cannot simulate the kite dynamics and is therefore excluded.

To select the best modelling approach the dynamics of real kite system was studied in the subsequent data analysis and system identification. Multiple phenomena were found and studied, of which the following are relevant:

- The steering of the kite has been studied. A useful relation is found which relates the rotation of the kite to the steer input and the side slip angle (or gravitational vector). This relation originates from a moment study of the kite on a quasi-static basis and corresponds with measurement data. The relation is very useful in kite modelling and in controller design. The moment study also showed the relevant parameters for the turning speed of the kite and pointed out that bigger kites most likely turn slower.
- The side slip angle has been studied. The quasi static force analysis pointed out that the kite has to fly with a side slip angle to overcome gravity. Measurement data confirmed this and showed that the current kite often flies with side slip angles of 10-15°. Locally higher peaks are measured during the exiting of the downward loops.
- The sagging of the tether has been studied. It was established that the tether sag and pod dynamics result in relatively small sag angles of 0-15° during regular flights. The sagging and pod dynamics of the line have a distinctive pattern during a figure of eight movement which indicates that especially the pod dynamics plays an role in the kite dynamics.
- A first attempt has been undertaken to fit the aerodynamic coefficients to the measurement data. These coefficients are needed in an aerodynamic force model. While validating the complete system model in chapter 8 it was found that the aerodynamic coefficients are most likely too high and altered. These errors were most likely due to an incorrect estimation of the apparent wind speed in the system identification. In future studies the fit of aerodynamic coefficients could be improved by measuring the apparent wind speed directly at the kite for example with a pitot tube.

Based on the literature study and these results the workable models were evaluated. Since the kite flies with a side slip angle during normal flight it was concluded that a point mass model is inadequate. They incorrectly assume that the kite is aligned with the apparent wind. The other option, the development of a full rigid body kite model, is ineffective because the kite is bridled and as a result the kite rotations are constrained in two directions. Dynamic modelling of the bridle does not add any information and would only slow the simulation down. Therefore a semi-rigid kite model was developed which only simulate the rotation of the kite around the tether.

Question remained how the tether should be modelled for realistic results. The sagging of the tether and the pod dynamics are small but clearly visible in the measurement data. A discretised tether model is able to simulate these effect however will slow the simulation down. A spring damper tether model is simpler and faster but will assume the tether to be straight. It was unknown if the relative small angles would have a big influence on the accurate modelling of the kite system. Therefore two semi rigid kite model have been developed. One with a straight spring-damper tether model and one with a discretised point mass tether model.

The complete set of equations, which describe the dynamics of both models, have been derived. A aerodynamic force model is included based on the aerodynamic coefficients found in the system identification. The models are successfully implemented in the Simulink environment.

The validation of the developed models is difficult. The wind speed in front of the kite could not be measured but is essential in the validation process. Additional errors in the GPS sensors and the unavailable data of the pitot sensor further compromise the validation. To express the accuracy of the developed kite models in numbers is therefore not possible. To be able to validate the kite model a different approach was chosen. The kite model is extended with a winch model, wind model, state machine and autopilot to make a complete system model. This complete system model could be compared with test data..

In chapter 8 the two complete kite system models are simulated with the same wind speed, controller settings and initial positions as during the test day. Since the complete system is modelled theoretically the same results are expected. One random cycle of 148 seconds is selected from the measurement data and is compared. In general both models show good resemblance with the measurement data, after the lift and drag curve has been altered. The trajectory of the measurement data and the two full system models are roughly aligned for over 150 seconds. Considering the numerous possibilities for errors this is above expectations and a good indication of the correct implementation. The average power of the two models and measurement data differs only 3% (1.54 kW vs. 1.49kW respectively) confirming the correctness of the model. Some small differences have been found and suggestions are done for future improvements. Especially the kite speed of the kite model with the discretised tether is too high indicating a too low tether drag coefficient.

The discretised tether model was able to realistically simulate the dynamics of the pod and the tether. The same sagging patterns are found in the modelling and measurement data. The discretised tether model simulates the angle of attack more realistically then the straight spring damper model. Because the sagging of the tether prevents a large change in angle of attack during the downward loop. An unexpected advantage of this model is its capability to simulate irregular flight conditions. For example, when the tether tension is set to zero the kite will just glide down due to the weight of the pod and the kite. These non-normal flight conditions are interesting for controller design.

When comparing both tether models it is concluded that each model has its own advantages. The straight tether model is faster and especially suitable for optimization studies were many simulations have to be done subsequently. The model runs approximately 7x faster than real time. The discretised tether model is slower but incorporates the sagging of the tether and gives a better representation in non-normal flight conditions and is therefore more suitable for control design and realistic modelling. Currently the model runs approximate 0.5x real time.

All together it can be concluded that a realistic semi rigid body kite model has been developed. The tether is simulated by a straight spring damper tether model or by a discretised point mass tether model. Both tether models have their own advantages. The model is validated to the maximum current capabilities and shows good resemblance with measurement data. Some parts could still be further improved. Nevertheless the developed model is simple, fast and realistic. It is useful for future studies in the field of controller design, performance optimization, cost analysis or for example offline system tests. Hopefully this will lead to an optimised system, smart control and eventually a breakthrough in sustainable energy technology in the form of kites flying high in our sky.



10 RECOMMENDATIONS

For future work several recommendations are formulated.

A first step has been taken to extend the developed kite model to a full system model. A wind model, winch model, autopilot and state machine are incorporated. This is however done in a simplified way since it was not the goal of this thesis. The current winch model has to be replaced by a realistic winch model with a winch controller and the state machine has to be extended to model the current control strategy more precise.

Currently all aerodynamic coefficients are based on the system identification. However during the validation of the kite model it was found that multiple coefficients were slightly too high. Even the lift and drag curve had to be changed to get realistic results. An extensive research is needed into the modelling of the aerodynamic forces. Van Kappel [76] is currently working on an aerodynamic force model based on a panel method. Possibly this model could be integrated in the model. Another, probably more accurate option would be to develop a method which determines the aerodynamic coefficients based on dynamic flight data. Such methods are available in airplane flight dynamics. The present improvements in the sensors of the system (new GPS, pitot tube, better logging) makes a successful system identification more likely.

During validation it was found that the model with a straight tether does not simulate the angle of attack correctly. It is recommended to investigate if a fixed aerodynamic coefficient for powered and depowered flight will produce more accurate results in the case of a straight tether model.

The kite model with a discretised tether model does currently not run in real time. This is due to the discretised tether model which is highly nonlinear and stiff and therefore requires small time steps. Stiff nonlinear problems have always been difficult to model efficiently nevertheless special algorithms are available to speed up these simulations. When continuing with discretised tether models the implementation of these more advance algorithms is recommended.

It is worth evaluating if a discretised point mass tether model with only two masses, the kite and the pod, is advantageous. This would increase the simulation speed. Current simulation results seem to indicate that the pod dynamics are most important.

Appendix A: PARAMETERS

A.1 KITE MUTINY 25M2 V2

Symbol	Parameter	Value	Unit	Reference
A_{kite}	Projected surface area (\mathbf{XY}) _B	18.18	m ²	[77]
A_{side}	Projected side surface area of kite. (\mathbf{XZ}) _B	2.38	m ²	[77]
b	Wing span	6.97	m	[77]
m_{kite}	Mass of kite	10.5	kg	
m_{pod}	Mass of control pod	12	kg	
Ω	Volume of the kite	0.7657	m ³	[77]
I	Moment of inertia	$\begin{bmatrix} I_{XX} & I_{XY} & I_{XZ} \\ I_{XY} & I_{YY} & I_{YZ} \\ I_{XZ} & I_{YZ} & I_{ZZ} \end{bmatrix} = \begin{bmatrix} 69.6 & 0 & -4.3 \\ 0 & 15.6 & 0 \\ -4.3 & 0 & 63.6 \end{bmatrix}$	kgm ²	[77]

A.2 DYNEEMA TETHER

Symbol	Parameter	Value	Unit	Reference
A_T	Cross sectional area of the tether	12.56	mm ²	
c_0	Unit damping constant	473 ± 23 (1σ)	Ns	Appendix F:
d_T	Diameter tether	4	mm	
E_T	Tether elasticity modulus	4.8 · 10 ¹⁰	N/m ²	Appendix F:
k_0	Unit spring constant	6.1462 ± 0.0176 x 10 ⁵ (1σ)	N	Appendix F:
r_{ref}	Unstretched tether length (discretization)	50	m	
ρ_{tether}	Density tether	960	kg/m ³	

A.3 AERODYNAMIC PARAMETERS

Symbol	Parameter	Value	Unit	Reference
c_1	Yaw correlation coefficient 1 (w.r.t. steer input)	0.2	[-]	
c_2	Yaw correlation coefficient 2 (w.r.t. gravity)	0.25	[-]	
c_3	Yaw correlation coefficient 3 (w.r.t. side slip)	-1.1	[-]	
c_4	Side force correlation coefficient	0.8	[-]	
$C_{\perp D,T}$	Normal tether drag coefficient	1.22	[-]	
$C_{\parallel D,T}$	Parallel (friction) tether drag coefficient	0	[-]	
C_D	Drag coefficient	see Figure 8-1	[-]	
C_L	Lift coefficient	see Figure 8-1	[-]	
C_R	Resultant aerodynamic force coefficient	see Figure 5-27	[-]	
C_S	Side force coefficient	see chapter 5.10	[-]	
$C_{Z_{\alpha}(P_s)}$	Aerodynamic moment coefficient due to steering	0.032	[-]	
$C_{Z_{\beta}}$	Aerodynamic moment coefficient due side slip	0.091	[-]	
C_{Z_r}	Aerodynamic moment coefficient damping	-0.018	[-]	

A.4 WIND PARAMETERS

Symbol	Parameter	Value	Unit	Reference
z_0	Surface roughness length	± 1	m	
z_{ref}	Height of wind sensor	6	m	
ρ_{air}	Density air	1.225	kg/m ³	

Appendix B: NOMENCLATURE

This appendix is adopted from the thesis “Automatic Flight Control of Tethered Kites for Power Generation” from Jehle [71] and extended. The appendix gives an overview of the currently used notation and reference frames at the Kite Group at ASSET.

B.1 GENERAL NOMENCLATURE

Category	Notation	Remarks
Vectors	$\mathbf{v}, \boldsymbol{\gamma}$	bold, straight, lowercase ⁱ
Matrices	$\mathbf{M}, \boldsymbol{\Gamma}$	bold, straight, uppercase
Points	\mathbf{P}	bold, straight, uppercase ⁱⁱ
Scalars	A, a, α	normal, italic, upper and lowercase
Sets, Domains	S	normal, italic, uppercase

TABLE 13, SUMMARIZATION OF TYPEFACE DEFINITIONS OF VARIABLES

Remarks

1. This notation is also used for ‘unreal’ vectors, i.e. tuples that are not element of \mathbb{R}^3 . An example are the azimuth and elevations pairs $\mathbf{q} = [\xi, \eta]^T \in S \subset \mathbb{R}^2$.
2. Although the same notation as matrices, a confusion is unlikely, as most often used in different contexts.

B.2 INDEXING OF VECTORS AND MATRICES

Vectors in particular are elements of \mathbb{R}^3 and physically describe directions. For example the position vector pointing from a point \mathbf{A} to a point \mathbf{B} would be denoted by:

$$\mathbf{r}^{A,B} = \mathbf{r}^{AB} \stackrel{A=0}{=} \mathbf{r}^B \quad (-1)$$

Hence the direction of a vector is indexed *at* the vector with a right-upper index, where the two connected points are delimited by a comma. The first point is the starting point, the second the endpoint. If confusion is unlikely, the comma is dropped. Moreover, if the first point is the origin $\mathbf{0}$, it is often neglected. For angular rates $\boldsymbol{\omega}^{AB}$ (and accelerations), the indices correspond to references (reference frames) and have to be read as “the rotation of B relative to A”. If A is believed to be inertial, it is often dropped.

If the interpretation of a vector being a connection between points is difficult, e.g. for velocity vectors or the base vectors of a reference frame, their direction in a meaningful context is denoted there, however most often in lowercase letters to avoid confusion with points:

$$\mathbf{e}^z = [0 \ 0 \ 0]^T \quad (-2)$$

This vector is the unit vector in z-direction. The lower-right position is used for general purpose that arises from the context of usage.

- **N.B.:** It is often difficult to clearly distinct whether an index should be upper- or lower-right, e.g. the course vector \mathbf{t}_c . It is indeed pointing in the direction of the course, which would justify putting an upper-right C. Yet it is also in some sense closer describing the purpose of this tangent vector, namely the tangent vector to a curve, hence also a lower-right index is vindicated.
- **N.B.:** An upper-right T corresponds to the transposition operation, if not denoted differently.

Especially in differential geometry on surfaces, which is required and employed extensively in this thesis, it is often necessary to indicate the supporting point of a vector, which is marked by an upper-left index. An (i.e. one) interpretation is given in the following equation. Imagine the tangential vector $\mathbf{t}(s)$ to a parameterized curve $\gamma = \gamma(s)$. To abbreviate the declaration, at which parameter s_A the tangential vector has been evaluated, it is handy to write:

$$\mathbf{t}_\gamma(s = s_A) = \left(\frac{d}{ds} \gamma(s) \right) \Big|_{s=s_A} := {}^A \mathbf{t}_\gamma \quad (\Rightarrow \mathbf{A} = \gamma(s = s_A) \hat{=} {}^A \gamma) \quad (-3)$$

This is of course also valid for points, as indicated in brackets.

B.3 REFERENCE FRAMES AND TIME DERIVATIVES

Every vector can be expressed (i.e. its components) in different frames of reference. It is important to visualize that this is only ‘tool’ for humans to be able to conceive and handle vectors in an easier way. The application of reference frames does not change the actual vector. To emphasize this fact also in notation, the indication of the reference frame in which the components of a vector have to be understood, are indicated ‘outside’ (in contrast to an indication ‘at’ the vector as shown, cf. above) the vector by a lower-right index of the bracketed vector:

$$(\boldsymbol{\omega}_K)_W = {}_W \mathbf{T}_K \cdot (\boldsymbol{\omega}_K)_K \quad (-1)$$

The left-hand side indicates that the components of the kite’s rotational rates are given in the wind-reference frame. However, as they are measured by gyroscopes fixed to the kite, they are thus available in kite-fixed reference frame; they have to be transformed from K to W via the linear transformation matrix ${}_W \mathbf{T}_K$, to be read from lower-right to lower-left. Theory on transformation matrices themselves is anticipated to be known and will not be treated here.

As the transformation matrix can be interpreted as a function of consecutive rotations from one reference frame to another, and reference frames may rotate in respect to each other, the matrices are functions in time. Therefore their time dependency has to be regarded when differentiating. Let \mathbf{v} be an arbitrary vector and A, B two reference frames:

$$\begin{aligned} (\mathbf{v})_A &= {}_A \mathbf{T}_B \cdot (\mathbf{v})_B & \Big| \cdot \frac{d}{dt} \\ \frac{d}{dt} (\mathbf{v})_A &= {}_A \mathbf{T}_B \cdot \left(\frac{d}{dt} (\mathbf{v})_B \right) + \left(\frac{d}{dt} {}_A \mathbf{T}_B \right) \cdot (\mathbf{v})_B & \Big| \frac{d}{dt} (\#)_A := (\dot{\#})_A \\ (\dot{\mathbf{v}})_A^A &= {}_A \mathbf{T}_B \cdot (\dot{\mathbf{v}})_B^B + {}_A \dot{\mathbf{T}}_B \cdot (\mathbf{v})_B \end{aligned} \quad (-2)$$

The outer upper-right index denotes the reference frame, relative to which a vector has been differentiated. This can also be interpreted as the amount of which the components of the vector change as observed by a reference-frame-fixed observer. Left-multiplying Eq. (1.3) by ${}_B \mathbf{T}_A$ yields

$$\begin{aligned}
(\dot{\mathbf{v}})_B^A &= (\dot{\mathbf{v}})_B^B + {}_B\mathbf{T}_{AA}\dot{\mathbf{T}}_B \cdot (\mathbf{v})_B \\
&= (\dot{\mathbf{v}})_B^B + (\tilde{\boldsymbol{\omega}}^{A,B})_B \cdot (\mathbf{v})_B \\
&= (\dot{\mathbf{v}})_B^B + (\boldsymbol{\omega}^{A,B})_B \times (\mathbf{v})_B,
\end{aligned} \tag{-3}$$

respectively in a reference-free version

$$(\dot{\mathbf{v}})^A = (\dot{\mathbf{v}})^B + \boldsymbol{\omega}^{AB} \times \mathbf{v} \tag{-4}$$

Hence, the change of \mathbf{v} relative to A (left-hand side) consists of a change of \mathbf{v} as observed in B (1. term RHS) plus the relative rotation of B in respect to A (2. term RHS).

B.4 REFERENCE FRAMES IN PROGRAMMING LANGUAGES

The use of lower and uppercase in programming languages is in generally not possible. Therefore a different notation is used in programming (Matlab, C++, Java). The reference frame is indicated in front of the vector (instead of the lower-right index outside the brackets) and the reference frame and vector are separated by an underscore. The general indication (lower-right index *at* the vector) is written after the vector, again separated by an underscore.

Point	Notation	Programing
Position	P	-

Vector	Notation	Programing
Position vector	P	R
Velocity	v = $\dot{\mathbf{p}}$	V
Acceleration	a = $\ddot{\mathbf{p}}$	A
Angle	θ	W
Angular velocity	$\boldsymbol{\omega}$	O (omega)
Angular acceleration	$\boldsymbol{\alpha}$	- (not used yet)

Indication	Notation	Programing
Kite	Kite	k
Kite Sensor	KiteSensor	ks
Wind	Wind	w
Apparent wind	App	wapp

Reference frame	Notation	Programing
Earth-Xsens	<i>EX</i>	ex
Earth-Groundstation	<i>EG</i>	eg
Wind	<i>w</i>	w

Etc... (see Table 14)

Examples

	Thesis	Programing
Position of the kite measured by the GPS in earth reference frame	$(\mathbf{P}_{\text{Kite}})_{EX}$	ex_R_k
Angular velocities of the kitesensor measured by IMU in kite sensor reference frame	$(\boldsymbol{\omega}_{\text{KiteSensor}}^{EX,KS})_{KS} = (\boldsymbol{\omega}_{\text{Kite}}^{EX,K})_K$	k_O_k
Apparent wind described in kite reference frame	$(\mathbf{v}_{\text{App}})_K$	k_V_wapp

Appendix C: REFERENCE FRAMES

Positions, velocities and acceleration are given in a Eulerian specification. Positions, velocities and accelerations are always with respect to a certain reference frame. Angles are always defined by right hand rotation around a given axis of a given reference frame. Below a listing is given of all reference frames that are used in this thesis. These frames are currently the standard at the ASSET kite group.

1. The earth fixed reference frames (EX and EG) are used as inertial reference frame. The wind reference frame W rotates along with the wind. The wind reference frame is used to describe the location of the kite in azimuth and elevation angles relative to wind window
2. The kite sensor reference frames KS is measured with the IMU/GPS. The sensor is not aligned perfectly with the kite, therefore KS frame has to be corrected for misalignment. The result is the kite frame K which determines the orientation of the kite and is used to analyse the data. See Figure C-2.
3. For data analysis, control and modelling it is useful to define a reference frame which is tangential to the (unit) sphere. Two reference frames which are tangential to a sphere are used. The small-earth frame, SE and the local frame L . Both frames are almost identical only the origin differs. The SE frame is especially used in control. The local frame is used to determine the tether sag from test data. Further the L frame is used in modelling.
4. The local frame L is not appropriate when a discretised tether model is used. Therefore an additional reference frame is constructed, which is called the local tether frame LT . The LT reference frame is derived based on the orientation of the last discretized tether element.
5. The modelling frame B is used to express the orientation of the kite in the model. The B frame is achieved by two consecutive rotations of the L frame (yawing and pitching).
6. Two velocities frames are used to calculate various angles. The apparent wind frame AW is coupled to the aerodynamic velocity vector \mathbf{v}_{app} and the kite velocity frame KV is coupled to the \mathbf{v}_{kite} .

C.1 TABLE WITH REFERENCE FRAMES

Reference frames	Abbre	Origin	Definition X	Definition Y	Definition Z	Remark
Earth fixed reference frames						
Earth-Xsens	EX	Tether exit point $\mathbf{0}$	North	(East)	\perp to ground	Used as inertial RF (not completely true since the earth is rotating)
Earth-Groundstation	EG	Tether exit point $\mathbf{0}$	$+\mathbf{x}_{EX}$	$(-\mathbf{y}_{EX} = \text{West})$	$-\mathbf{z}_{EX}$	
Wind	W	Tether exit point $\mathbf{0}$	Downwind	(\otimes)	$+\mathbf{z}_{EG}$	Non-inertial RF
Sensor frames (with IMU/GPS)						
Kite sensor	KS	IMU	Main strut	Left to right wingtip	(\otimes)	= Note that the sensor is not in kite CG
Kite frame	K	Kite CG	Main chord line	Left to right wingtip	(\otimes)	= KS corrected for misalignment
Tangential frames to unit sphere (used for autopilot & determination of tethersag etc)						
Small Earth	SE	$\mathbf{P} \in M$	(Small-North)	$\mathbf{z}_w \times \mathbf{p}^{OP}$	$-\mathbf{p}^{OP}$	SE and L are almost identical, only the origin differs. Both tangential to unit sphere
Local	L	Kite CG	(Small-North)	$\mathbf{z}_w \times \mathbf{p}^{OP}$	$-\mathbf{p}^{OP}$	
Frames used in modeling						
Local tether	LT	Kite CG	$\mathbf{x}_{LT} = \mathbf{z}_{LT} \times \mathbf{y}_{LT}$	$\mathbf{y}_{LT} = \mathbf{z}_{LT} \times \mathbf{z}_{EG}$	\mathbf{p}^{m_2}	Used in kite model with a discretized tether. Tangential to last tether element
Body	B	Kite CG	Symmetry plane \mathbf{xz}_B	-	-	Local frame L first rotated around \mathbf{z}_L axis and secondly around \mathbf{y}_L axis. Identical to kite frame K , only zero roll ($\phi^{SE,K} = 0$) by definition.
Velocities frames						
Apparent wind (air-path)	AW	Kite CG	\mathbf{v}_{app}	(\otimes)	Symmetry plane \mathbf{xz}_B	Used for aerodynamic forces $\begin{pmatrix} F_D \\ F_C \\ F_L \end{pmatrix}$
Kite velocity (flight-path)	KV	Kite CG	\mathbf{v}_{kite}	(\otimes)	Symmetry plane \mathbf{xz}_B	Used for kinematic slip angles and control.

TABLE 14, ORIGINS AND DEFINITIONS OF REFERENCE FRAMES

Remarks

1. All reference frames are right-handed
2. The axis that results from applying the right-hand rule on two principle ones is denoted in brackets
3. \mathbf{p}^{0P} is the unit vector pointing from 0 to P, where **P** is the location of the kite.
4. In the case of a discretized tether the unit vector $\mathbf{p}^{m_1 m_2}$ is used. This unit vector points along the last tether element (from the last mass m_1 to the second last mass m_2)
5. The *SE* and the *L* frame are identical and could be combined. However to make a clear distinction between control and modelling both frames are used.
6. $\psi^{SE,K}$ and $\psi^{L,B}$ are defined as the heading of the kite

C.2 EARTH FIXED REFERENCE FRAMES & WIND

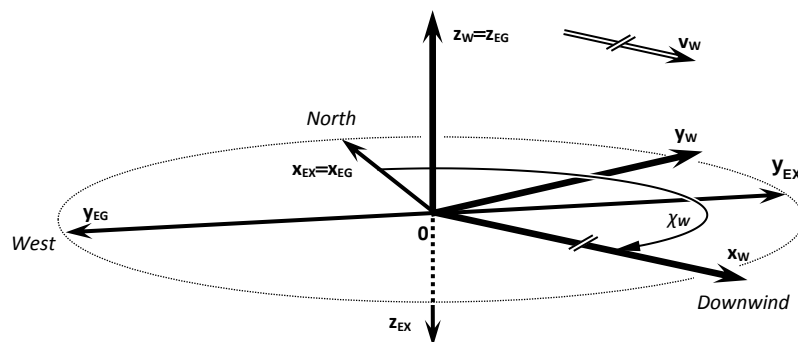


FIGURE C-1, ILLUSTRATION OF THE THREE REFERENCE FRAMES EX, EG AND W

C.3 SENSOR REFERENCE FRAMES AND TANGENTIAL FRAMES

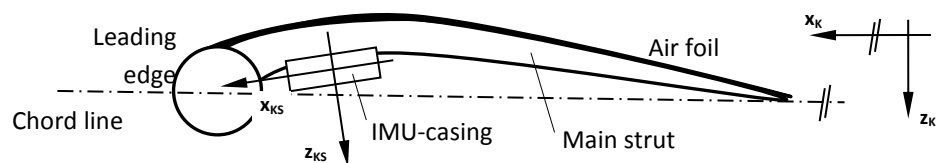


FIGURE C-2, ILLUSTRATION OF THE TWO FRAMES KS AND K FRAME

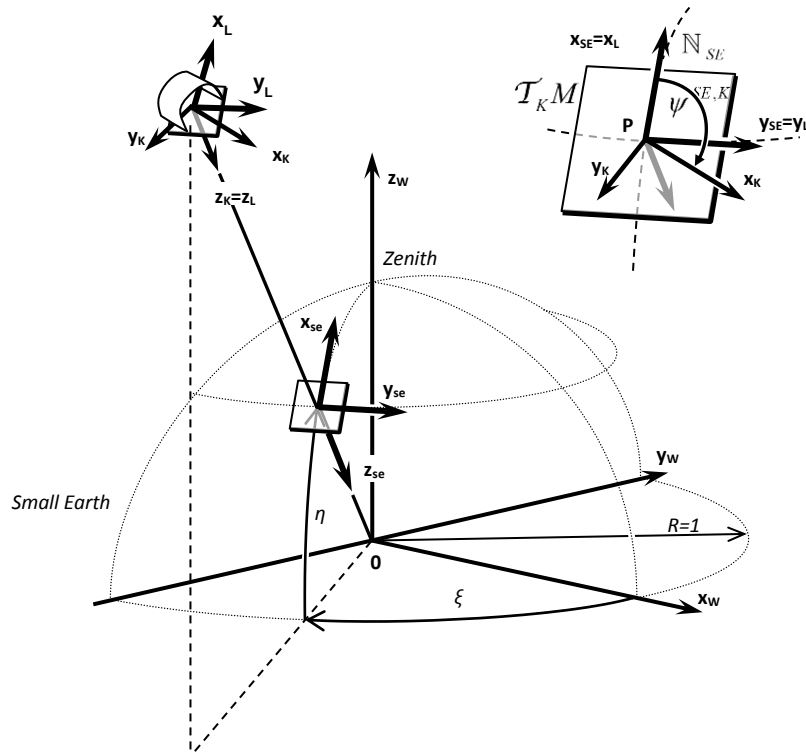


FIGURE C-3, ILLUSTRATION OF W, K, SE AND L REFERENCE FRAME; NOTE THAT $\theta_{SE}^{SE,K} = \phi_{SE}^{SE,K} = 0$ HAS BEEN ASSUMED

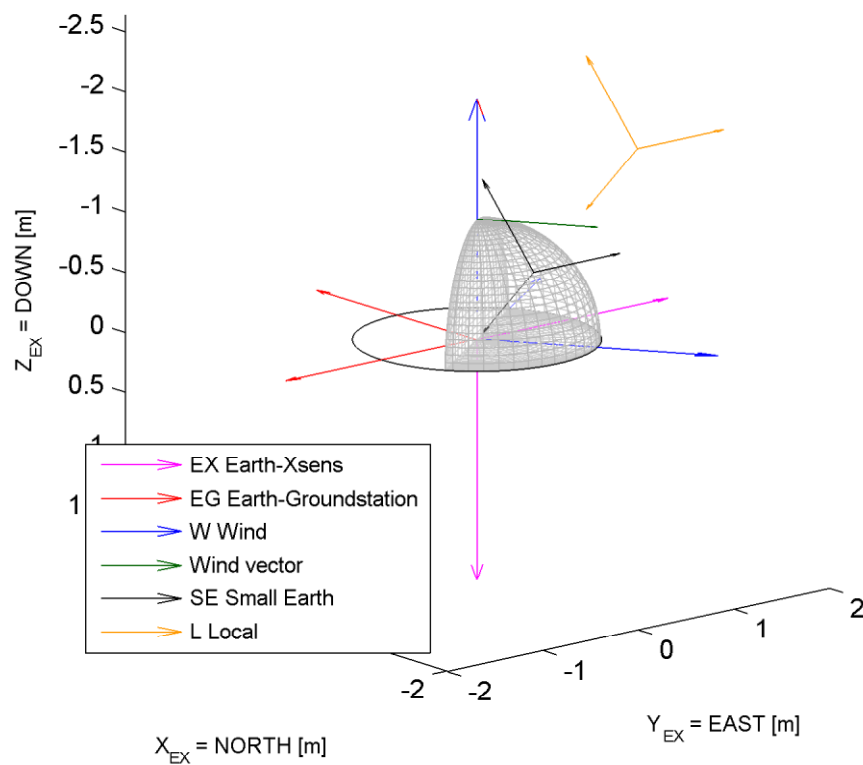


FIGURE C-4, ILLUSTRATION OF THE SMALL-EARTH SE AND LOCAL REFERENCE FRAMES L

While Figure C-1 illustrates the three reference frames EG, EX and esp. W at the tether exit point 0, in Figure C-3 the small-earth-analogy is visualized. Imagine a unit sphere wrapped around the tether exit point 0, then

- this unit sphere is referred to as small earth,
- the azimuth and elevation angles ξ , η correspond to longitude and latitude, respectively⁴,
- the zenith, also denoted as small-north pole, corresponds to the earth's north pole,
- the tether force can be interpreted as the gravitational force.

In general, if analogies between the real world and the small earth shall be emphasized, the word 'small' is prepended (e.g. 'small west' to indicate the y -axis of the SE-reference frame).

C.4 LOCAL TETHER FRAME

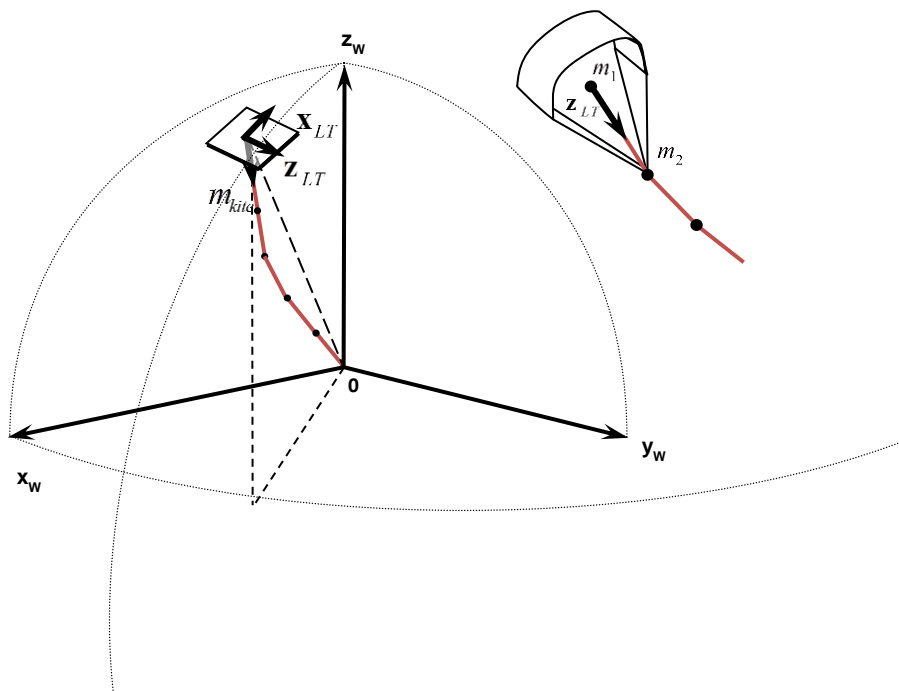


FIGURE C-5 ILLUSTRATION OF THE LOCAL TETHER FRAME, LT

⁴ Note however that the azimuth is counted positive east-wards, in contrast to the longitude.

C.5 BODY FRAME

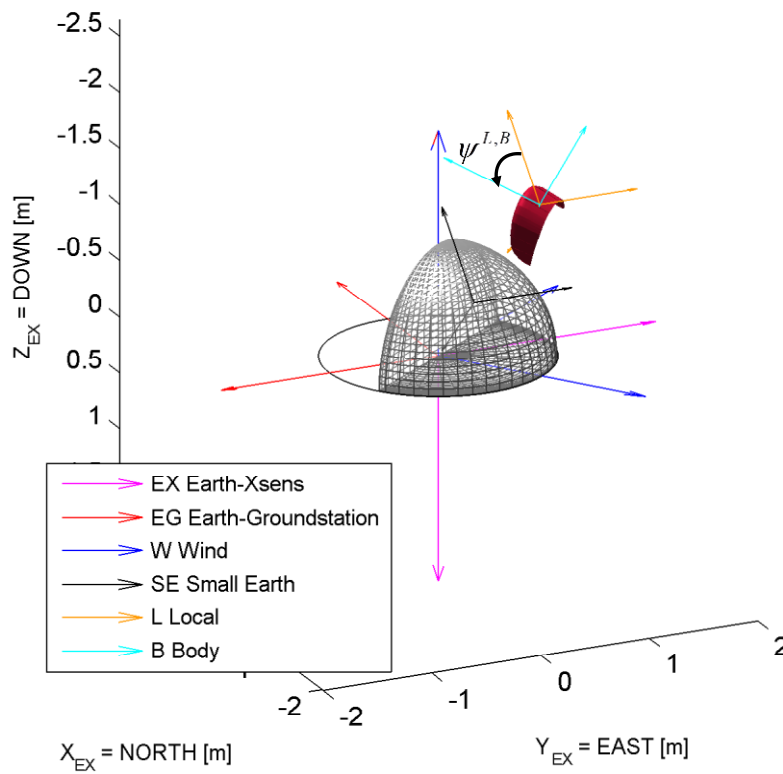


FIGURE C-6, ILLUSTRATION OF THE BODY FRAME, FIRST ROTATION $\psi^{L,B}$, YAWING AROUND Z_L

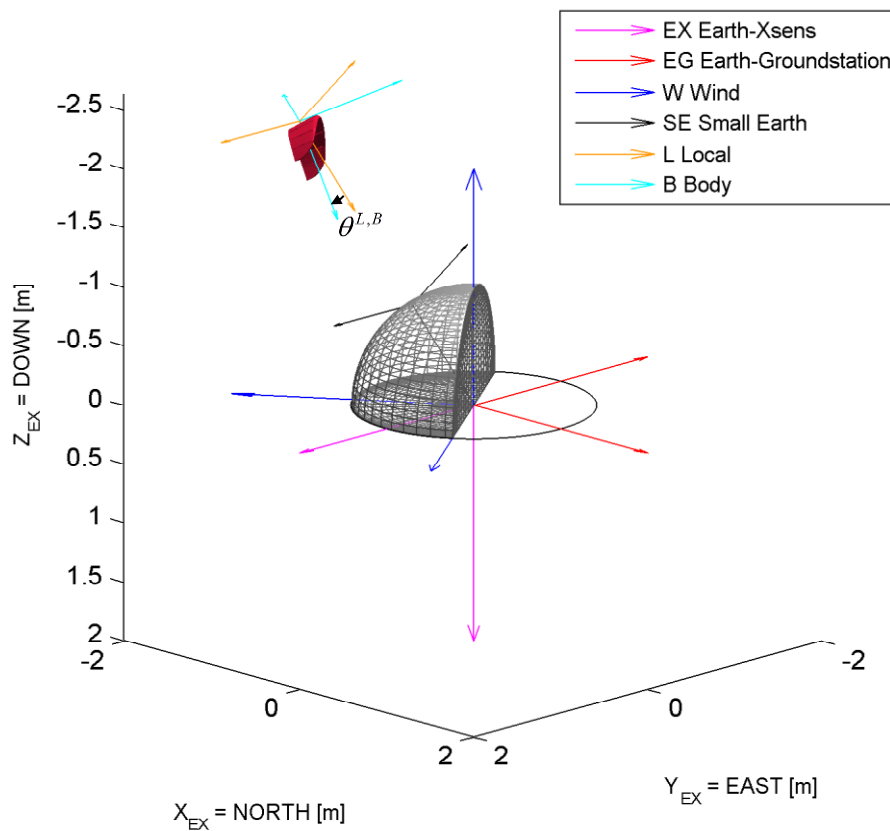


FIGURE C-7, ILLUSTRATION OF THE BODY FRAME, SECOND ROTATION $\theta^{L,B}$, PITCHING AROUND Y_L

C.6 APPARENT WIND FRAME

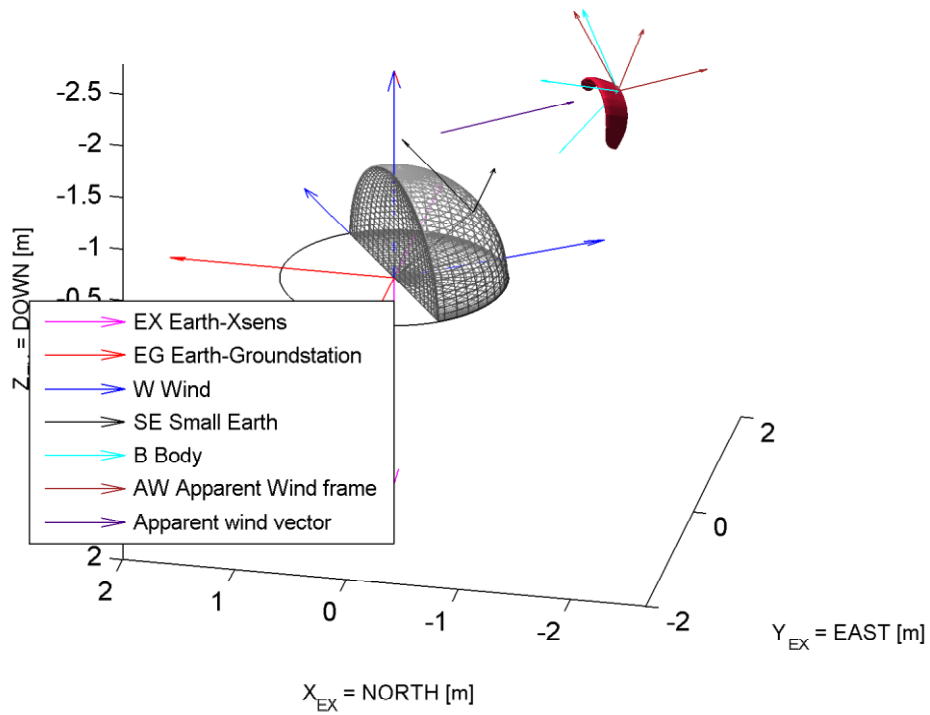


FIGURE C-8, ILLUSTRATION OF THE APPARENT WIND FRAME

C.7 ALL REFERENCE FRAMES

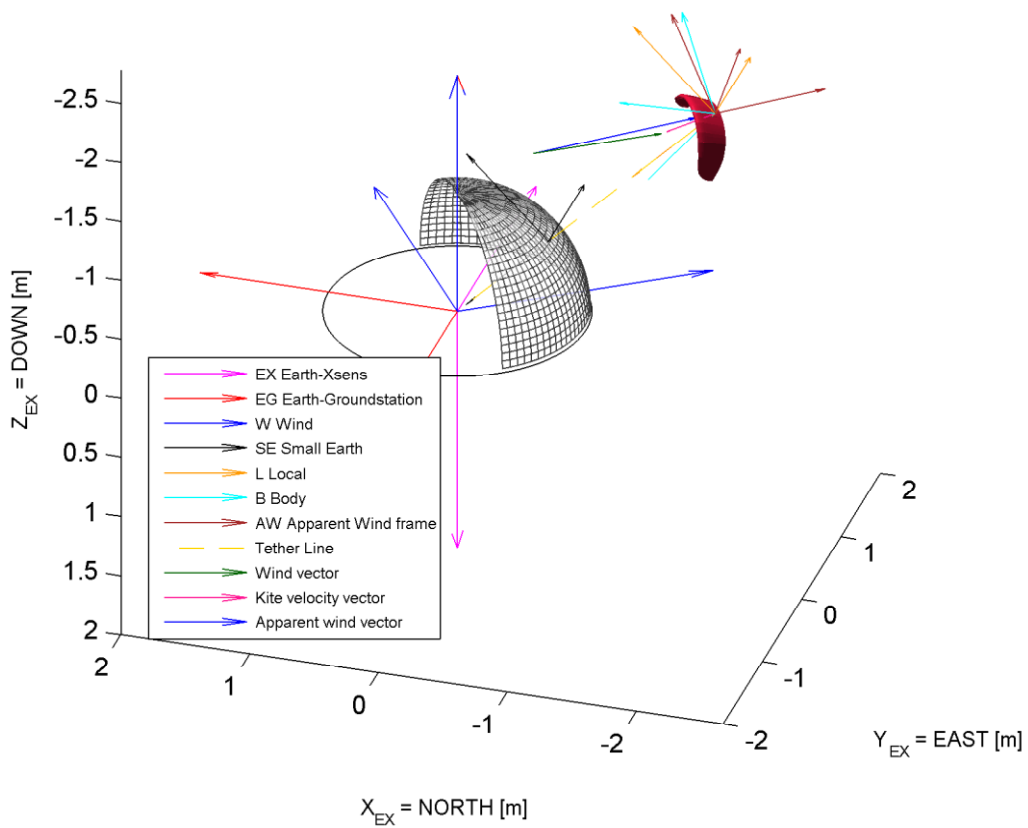


FIGURE C-9, ILLUSTRATION OF THE ALL REFERENCE FRAMES CURRENTLY USED

Appendix D: TRANSFORMATION MATRICES OF REFERENCE FRAMES

The three basic rotation matrices used in this chapter are:

$$\mathbf{T}_x(\alpha) = \begin{bmatrix} 1 & 0 & 0 \\ 0 & c\alpha & s\alpha \\ 0 & -s\alpha & c\alpha \end{bmatrix}, \quad \mathbf{T}_y(\alpha) = \begin{bmatrix} c\alpha & 0 & -s\alpha \\ 0 & 1 & 0 \\ s\alpha & 0 & c\alpha \end{bmatrix}, \quad \mathbf{T}_z(\alpha) = \begin{bmatrix} c\alpha & s\alpha & 0 \\ -s\alpha & c\alpha & 0 \\ 0 & 0 & 1 \end{bmatrix}$$

Sometimes it is useful having the following relations at hand:

$$\begin{aligned} \sin(-\alpha) &= -\sin(\alpha) \\ \cos(-\alpha) &= \cos(\alpha) \end{aligned}$$

D.1 TRANSFORMATION FROM EX TO EG

$${}_{EG}\mathbf{T}_{EX} = \mathbf{T}_x(\pi) = \begin{bmatrix} 1 & 0 & 0 \\ 0 & -1 & 0 \\ 0 & 0 & -1 \end{bmatrix}$$

D.2 TRANSFORMATION FROM EG TO W

$${}_{W}\mathbf{T}_{EG} = \mathbf{T}_z(-\chi_w) = \begin{bmatrix} c(-\chi_w) & s(-\chi_w) & 0 \\ -s(-\chi_w) & c(-\chi_w) & 0 \\ 0 & 0 & 1 \end{bmatrix}$$

D.3 TRANSFORMATION FROM W TO SE/L

$$\begin{aligned} {}_{SE}\mathbf{T}_W &= {}_L\mathbf{T}_W = \mathbf{T}_y(-\eta)\mathbf{T}_x(-\xi)\mathbf{T}_y\left(-\frac{\pi}{2}\right) \\ &= \begin{bmatrix} c(-\eta) & 0 & -s(-\eta) \\ 0 & 1 & 0 \\ s(-\eta) & 0 & c(-\eta) \end{bmatrix} \begin{bmatrix} 1 & 0 & 0 \\ 0 & c(-\xi) & s(-\xi) \\ 0 & -s(-\xi) & c(-\xi) \end{bmatrix} \begin{bmatrix} c\left(\frac{-\pi}{2}\right) & 0 & -s\left(\frac{-\pi}{2}\right) \\ 0 & 1 & 0 \\ s\left(\frac{-\pi}{2}\right) & 0 & c\left(\frac{-\pi}{2}\right) \end{bmatrix} \\ &= \begin{bmatrix} -s\eta c\xi & s\eta s\xi & c\eta \\ s\xi & c\xi & 0 \\ -c\eta c\xi & c\eta s\xi & -s\eta \end{bmatrix} \end{aligned}$$

D.4 TRANSFORMATION FROM EX TO K

$$\begin{aligned} {}_K\mathbf{T}_{EX} &= \mathbf{T}_x(\phi_0)\mathbf{T}_y(\theta_0)\mathbf{T}_z(\psi_0) = \begin{bmatrix} 1 & 0 & 0 \\ 0 & c\phi & s\phi \\ 0 & -s\phi & c\phi \end{bmatrix} \begin{bmatrix} c\theta & 0 & -s\theta \\ 0 & 1 & 0 \\ s\theta & 0 & c\theta \end{bmatrix} \begin{bmatrix} c\psi & s\psi & 0 \\ -s\psi & c\psi & 0 \\ 0 & 0 & 1 \end{bmatrix} \\ &= \begin{bmatrix} c\theta c\psi & c\theta s\psi & -s\theta \\ s\phi s\theta c\psi - c\phi s\psi & s\phi s\theta s\psi + c\phi c\psi & s\phi s\theta \\ c\phi s\theta c\psi + s\phi s\psi & c\phi s\theta s\psi - c\phi c\psi & c\phi s\theta \end{bmatrix} \end{aligned}$$

D.5 TRANSFORMATION FROM SE TO K

$${}_{K} \mathbf{T}_{SE} = \mathbf{T}_X(\phi^{SE,K}) \mathbf{T}_Y(\theta^{SE,K}) \mathbf{T}_Z(\psi^{SE,K})$$

Identical to D.4.

D.6 TRANSFORMATION FROM L TO B

$$\begin{aligned} {}_B \mathbf{T}_L = \mathbf{T}_Y(\theta^{L,B}) \mathbf{T}_Z(\psi^{L,B}) &= \begin{bmatrix} c\theta^{L,B} & 0 & -s\theta^{L,B} \\ 0 & 1 & 0 \\ s\theta^{L,B} & 0 & c\theta^{L,B} \end{bmatrix} \begin{bmatrix} c\psi^{L,B} & s\psi^{L,B} & 0 \\ -s\psi^{L,B} & c\psi^{L,B} & 0 \\ 0 & 0 & 1 \end{bmatrix} \\ &= \begin{bmatrix} c\theta^{L,B} c\psi^{L,B} & c\theta^{L,B} s\psi^{L,B} & -s\theta^{L,B} \\ -s\psi^{L,B} & c\psi^{L,B} & 0 \\ s\theta^{L,B} c\psi^{L,B} & s\theta^{L,B} s\psi^{L,B} & c\theta^{L,B} \end{bmatrix} \end{aligned}$$

In modeling it is assumed that $\theta^{L,B}$ is a function of the power setting P_p

D.7 TRANSFORMATION FROM B TO AW

$$\begin{aligned} {}_{AW} \mathbf{T}_B = \mathbf{T}_Y(\pi) \mathbf{T}_Z(\beta) \mathbf{T}_Y(-\alpha) &= \begin{bmatrix} c\pi & 0 & -s\pi \\ 0 & 1 & 0 \\ s\pi & 0 & c\pi \end{bmatrix} \begin{bmatrix} c\beta & s\beta & 0 \\ -s\beta & c\beta & 0 \\ 0 & 0 & 1 \end{bmatrix} \begin{bmatrix} c(-\alpha) & 0 & -s(-\alpha) \\ 0 & 1 & 0 \\ s(-\alpha) & 0 & c(-\alpha) \end{bmatrix} \\ &= \begin{bmatrix} -c\beta c\alpha & s\beta & -c\beta s\alpha \\ s\beta c\alpha & c\beta & s\beta s\alpha \\ s\alpha & 0 & -c\alpha \end{bmatrix} \end{aligned}$$

Appendix E: MATLAB CODE REFERENCE FRAMES PLOTTING TOOL

```

%%%%%%%%%%%%%%%%%%%%%%%%%%%%%%%%%%%%%%%%%%%%%%%%%%%%%%%%%%%%%%%%%%%%%%%%
%% SHOW ROTATION MATRICES
% author: Marien Ruppert
% date: 12-9-2012
%%%%%%%%%%%%%%%%%%%%%%%%%%%%%%%%%%%%%%%%%%%%%%%%%%%%%%%%%%%%%%%%%%%%%%%%
clear all;
close all;
clc;

%% INPUT
eg_W_w    = 145 * pi/180; %wind hoek chi
V_w       = 1
ex_R_k    = [-2 0 -2]'    %positie kite in ex
ex_V_k    = 0.5*[0.5800 -0.8146 0]' %velocity kite in ex
psi_kite  = -45 * pi/180;
theta_kite = -10 * pi/180;

%% TRANSFORMATION FROM EX TO EG
egTex     = [[ 1      0      0 ]; ...
              [ 0     -1      0 ]; ...
              [ 0      0     -1 ]];
exTeg     = egTex';

%% TRANSFORMATION FROM EG TO W
wTeg      = [[ cos(-eg_W_w) sin(-eg_W_w) 0 ]; ...
              [ -sin(-eg_W_w) cos(-eg_W_w) 0 ]; ...
              [ 0      0      1 ]];
egTw      = wTeg';

%% CALCULATE ELEVATION AND AZIMUTH
w_R_k     = wTeg* egTex * ex_R_k;

elevation = (atan2(w_R_k(3,:),sqrt((w_R_k(1,:)).^2+(w_R_k(2,:)).^2)));
azimuth   = (atan2(-w_R_k(2,:),w_R_k(1,:)));

%% TRANSFORMATION FROM W TO SE OR L
tmp1      = [[ cos(-elevation)      0 -sin(-elevation) ]; ...
              [ 0      1      0 ]; ...
              [ sin(-elevation)      0 cos(-elevation) ]];

tmp2      = [[ 1      0      0 ]; ...
              [ 0      cos(-azimuth) sin(-azimuth) ]; ...
              [ 0      -sin(-azimuth) cos(-azimuth) ]];

tmp3      = [[ cos(-pi/2)      0 -sin(-pi/2) ]; ...
              [ 0      1      0 ]; ...
              [ sin(-pi/2)      0 cos(-pi/2) ]];

seTw      = tmp1 * tmp2 * tmp3;
wTse      = seTw';

lTw       = tmp1 * tmp2 * tmp3;
wTl       = lTw';

%% TRANSFORMATION FROM L TO B
tmp1      = [[ cos(theta_kite)      0 -sin(theta_kite) ]; ...
              [ 0      1      0 ]; ...
              [ sin(theta_kite)      0 cos(theta_kite) ]];

tmp2      = [[ cos(psi_kite) sin(psi_kite)      0 ]; ...
              [ -sin(psi_kite) cos(psi_kite)      0 ]; ...
              [ 0      0      1 ]];

bTl       = tmp1 * tmp2;

```

```

lTb      = bTl';

%% CALCULATE AERO VARIABLES
w_V_w    = ([1 0 0]' * V_w)
ex_V_w    = exTeg*egTw*w_V_w
b_V_w    = bTl*lTw*w_V_w

eg_R_k    = egTex*ex_R_k
b_V_k    = bTl*lTw*wTeg*egTex*ex_V_k

b_V_wapp  = b_V_w - b_V_k;
ex_V_wapp = exTeg*egTw*wTl*lTb*b_V_wapp

k_Alpha   = atan2(-b_V_wapp(3,:),-b_V_wapp(1,:));
rad2deg(k_Alpha)
k_Beta    = asin(-b_V_wapp(2,:)/norm3(b_V_wapp));
rad2deg(k_Beta)
k_Delta   = atan2(b_V_k(2,:),b_V_k(1,:));

%% TRANSFORMATION FROM B TO AW
tmp1      = [[ cos(pi)      0   -sin(pi)   ]; ...
             [ 0            1    0          ]; ...
             [ sin(pi)      0    cos(pi)    ]];

tmp2      = [[ cos(k_Beta)  sin(k_Beta)   0   ]; ...
             [ -sin(k_Beta) cos(k_Beta)   0   ]; ...
             [ 0            0            1   ]];

tmp3      = [[ cos(-k_Alpha)  0 -sin(-k_Alpha) ]; ...
             [ 0            1  0              ]; ...
             [ sin(-k_Alpha)  0  cos(-k_Alpha)  ]];

awTb = tmp1 * tmp2 * tmp3;
bTaw = awTb';

%% PLOT REFERENCE FRAME EARTH X DOWN BLACK
hFig = figure

set(gcf, 'Units', 'centimeters');
afFigurePosition = [1 2 15 15]; %
set(gcf, 'Position', afFigurePosition); %
set(gcf, 'PaperPositionMode', 'auto');

grid off
hold on
box off

origin = [ 0 0 0 ];
unitvec = [[ 1 0 0 ]; ...
           [ 0 1 0 ]; ...
           [ 0 0 1 ]];

hEx = quiver3(ones(3,1)*origin(1),ones(3,1)*origin(2),ones(3,1)*origin(3),...
             unitvec(:,1),unitvec(:,2),unitvec(:,3),2,'m')

%% PLOT REFERENCE FRAME EARTH GROUNDSTATION UP
eg = egTex * unitvec;
hEg = quiver3(ones(3,1)*origin(1),ones(3,1)*origin(2),ones(3,1)*origin(3),...
             eg(:,1),eg(:,2),eg(:,3),2,'r')

%% PLOT REFERENCE FRAME WIND
w = wTeg * egTex * unitvec;
hW = quiver3(ones(3,1)*origin(1),ones(3,1)*origin(2),ones(3,1)*origin(3),...
             w(:,1),w(:,2),w(:,3),2,'b')

%% PLOT WIND VECTOR

```



```

hWv = quiver3(ex_R_k(1)-ex_V_wapp(1),ex_R_k(2)-ex_V_wapp(2),ex_R_k(3)-ex_V_wapp(3),...
             ex_V_w(1),ex_V_w(2),ex_V_w(3),1,'color',[0 0.3906 0])

%% PLOT SPEED VECTOR
hKv = quiver3(ex_R_k(1),ex_R_k(2),ex_R_k(3),...
             ex_V_k(1),ex_V_k(2),ex_V_k(3),'color',[1.0000 0.0781 0.5742])

%% PLOT APPARENT WIND VECTOR
hAwv= quiver3(ex_R_k(1)-ex_V_wapp(1),ex_R_k(2)-ex_V_wapp(2),ex_R_k(3)-ex_V_wapp(3),...
             ex_V_wapp(1),ex_V_wapp(2),ex_V_wapp(3), 'color',[0 0 1])

%% PLOT REFERENCE FRAME SMALL EARTH
se = seTw * wTeg * egTex * unitvec;
hSe =quiver3(ones(3,1)*ex_R_k(1)/norm3(ex_R_k),ones(3,1)*ex_R_k(2)/norm3(ex_R_k),...
            ones(3,1)*ex_R_k(3)/norm3(ex_R_k),...
            se(:,1),se(:,2),se(:,3),'k')

%% PLOT REFERENCE FRAME LOCAL
l = lTw * wTeg * egTex * unitvec;
hL = quiver3(ones(3,1)*ex_R_k(1),ones(3,1)*ex_R_k(2),ones(3,1)*ex_R_k(3),...
            l(:,1),l(:,2),l(:,3),'color',[1.0000 0.6 0])

%% PLOT REFERENCE FRAME BODY
b = bTl * lTw * wTeg * egTex * unitvec;
hB = quiver3(ones(3,1)*ex_R_k(1),ones(3,1)*ex_R_k(2),ones(3,1)*ex_R_k(3),...
            b(:,1),b(:,2),b(:,3),'c')

%% PLOT REFERENCE FRAME WIND
aw = awTb * bTl * lTw * wTeg * egTex * unitvec;
hAw = quiver3(ones(3,1)*ex_R_k(1),ones(3,1)*ex_R_k(2),ones(3,1)*ex_R_k(3),...
            aw(:,1),aw(:,2),aw(:,3),'color',[ 0.6445 0.1641 0.1641])

%% PLOT KITE
[Tri, Pts_w] = plyread('finalekite.ply','tri');
clear Pts
Pts(:,1) = -Pts_w(:,2);
Pts(:,2) = Pts_w(:,1);
Pts(:,3) = -Pts_w(:,3);
Pts = Pts' / 10;
clear Pts_w
set(hFig,'Renderer','OpenGL');
lightangle(60,-60)

hKiteSym = trisurf(Tri ,...
                 Pts(1,:) ,...
                 Pts(2,:) ,...
                 Pts(3,)+0.4 ,...
                 'FaceColor',[ 0.8594 0.0781 0.2344],...
                 'EdgeColor','none');
set(hKiteSym,...
    'FaceLighting', 'flat', ...
    'AmbientStrength', 0.3, ...
    'DiffuseStrength', 0.8, ...
    'SpecularStrength', 0.3, ...
    'SpecularExponent', 15.0, ...
    'SpecularColorReflectance', 0.2, ...
    'BackFaceLighting','reverselit')

hTKiteSym = hgtransform; set(hKiteSym, 'Parent',hTKiteSym);

set(hTKiteSym,'Matrix',[ eye(3) [0 0 0]' ; 0 0 0 1 ] )
set(hTKiteSym,'Matrix',[ exTeg*egTw*wTl*lTb ex_R_k; 0 0 0 1 ] )

%% PLOT KITELINE
hTL = plot3([origin(1) ex_R_k(1)],[origin(2) ex_R_k(2)],[origin(3) ex_R_k(3)],...

```

```

    '--', 'color', [1 0.8398 0])

%% PLOT WINDWINDOW!
[X,Y] = pol2cart((0:5:360)*pi/180,1);
hCircle1 = plot3(X,Y,zeros(length(X)), 'k')

[XX,YY,ZZ] = sphere(51);
R0 = 0.99;
hBol = mesh(abs(XX)*R0, YY*R0, -abs(ZZ)*R0);
hTBol = hgtransform;set(hBol, 'Parent',hTBol);

Rz = makehgtform('zrotate',eg_W_w);
Sxy = makehgtform('scale',1);
set(hTBol, 'Matrix',Rz*Sxy)

colormap([1 1 1]*0.72)
set(hBol,...
    'FaceLighting','none',...
    'FaceAlpha', 0.3);

%% MAKE LEGEND
hLegend = legend(
    [hEx, hEg, hW,hSe,hL,hB,hAw,hTL,hWv,hKv,hAwv], ...
    'EX Earth-Xsens'           , ...
    'EG Earth-Groundstation'  , ...
    'W Wind'                   , ...
    'SE Small Earth'          , ...
    'L Local'                  , ...
    'B Body'                   , ...
    'AW Apparent Wind frame'  , ...
    'Tether Line'              , ...
    'Wind vector'              , ...
    'Kite velocity vector'     , ...
    'Apparent wind vector'     , ...
    'orientation', 'vertical', ...
    'location', 'BestOutside' );
set(hLegend, 'FontSize', 8 );

%% SET VIEW, AXIS LABELS, ETC
view(-163,29)
hx = xlabel('X_E_X = NORTH [m]')
hy = ylabel('Y_E_X = EAST [m]')
hz = zlabel('Z_E_X = DOWN [m]')
set([hx,hy,hz], 'fontsize',8)
set(gca, 'ZDir', 'rev')
set(gca, 'YDir', 'rev')
axis equal;

print(hFig, '-depsc2', '-r300', 'example_name')

```

Appendix F: EXPERIMENTAL DETERMINATION OF DYNEEMA PROPERTIES

To find the spring and damping coefficient of the Dyneema tether an experiment was carried out using the method described in [75].

F.1 THEORY

The stretch of a rope within its elastic limit consists of two components: permanent and elastic stretch. There is a permanent elongation upon initial loading, which arises because of, and varies in magnitude with, the rope construction. Elastic stretch is a reversible elongation that typically varies linearly with load over the working range of a rope according to Hooke's law,

$$F = -kx \quad (\text{F-1})$$

where F is the applied tension, x is the resulting elongation (the change in rope length generated by the application of the load F), and k is the spring constant of the rope. For a single homogeneous strand, the spring constant can be calculated from the Young's modulus of elasticity for the material from which the strand is made according to

$$k = \frac{EA}{l_0} \quad (\text{F-2})$$

where l_0 and A are the length and cross-sectional area of the unstretched line. However, typical ropes consist of many strands that can be arranged in a wide variety of ways. In addition, some constructions combine cores and jackets of different materials (a Dacron jacket on a Kevlar core, for example). Since these constructional features contribute to the elasticity of the rope, the application of (F-2) is inappropriate. Alternatively, an expression for the spring constant of a rope can be derived from the equation for a mass-spring oscillator. A mass hanging from a spring with elastic property described by (F-1) can be set into a linear oscillation by exciting the mass and then releasing it. Damping, which eventually brings the mass to rest, is caused by the rope's internal friction. For most cases, particularly when the friction is small, a good approximation is that the damping is proportional to the velocity. By approximating the internal friction in this way, the motion can be described as:

$$\ddot{x} + \frac{c}{m} \dot{x} - \frac{k}{m} x = 0 \quad (\text{F-3})$$

where x is the displacement of mass m from its equilibrium position and c is the damping constant. The following parameters are defined:

$$\begin{aligned} \omega_0 &= \sqrt{\frac{k}{m}} \\ \omega_0 &= 2\pi f \\ \zeta &= \frac{c}{2\sqrt{mk}} \end{aligned} \quad (\text{F-4})$$

Which result in the following differential equation:

$$\ddot{x} + 2\zeta\omega_0\dot{x} + \omega_0^2x = 0$$

This expression has a solution consisting of decaying and periodic terms:

$$x(t) = F * e^{-\zeta\omega_0 t} * \cos(\sqrt{1-\zeta^2}\omega_0 t - \phi) \quad (\text{F-5})$$

The displacement x and the Force in the tether are coupled so by measuring the time history of the force the parameters ζ and ω_0 can be determined from which the spring and damping constants can be calculated if the mass is known.

F.2 EXPERIMENT

The Dyneema tether was suspended on an overhead hoist in the 'vliegtuighal' at Aerospace Engineering. At both ends of the tether a splice of 20 cm was present. The splice will have an influence on the measured spring constant of the tether but there was no alternative and due the limited length the influence is expected to be small. The hoist has an maximum loading capacity of 6000kg. In our measurement we expect the crane to be far more stiffer than our tether and neglect the dynamics of the crane.

At the end of the tether two force measurement devices where present. One Celtron STC-1t load cell with calibrated loadmeter TR150 from Novatech. And a 1500 lbs loadcell from Transducer Techniques with an self-build analogue amplifier attached to a GWinstek - GDS-1000A oscilloscope. Two loadcells where used because the measuring frequency of the loadmeter of Novatech was too low. The first loadcell was used to correctly determine the weight of the mass and the second was used to make a time history of the tension in the tether. The oscilloscope saved the data on a sd-card and after the experiment the data was imported in matlab.

To the second loadcell a threaded rod was attached where metal disks of 20kg and 10 kg could be loaded. The weight of the two load cells and the threaded rod was 2.7kg. Figure F-1, F-2 and F-3 show the setup.

The mass was excited by dropping a 10kg metal disk on top from approximately 3cm high. The test was performed with three different weights (+/-300kg, 200kg and 100kg) and each test was performed three times.

As a secondary test and as check-up also the elongation of the tether was measured. A tape-measure was attached to the top of tether just below the splice. At the bottom an mark was placed and the length of the tether was noted after each 20kg increase of the load. Because we measured the elongation between the splices the splices didn't influence the measurement.

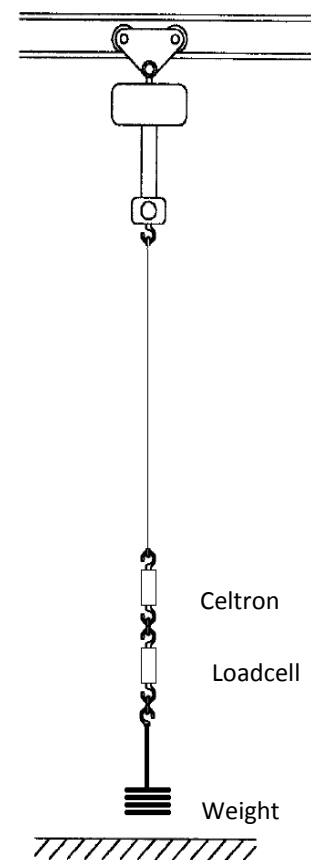


FIGURE F-1, EXPERIMENT SETUP

Loadcell 1	
Manufacturer	Celtron
Number	STC-1t
Rated weight	1000kg

Loadcell 2	
Manufacturer	Transducer Techniques
Rated weight	1500lbs

Oscilloscope	
Manufacturer	GWinstek
Number	GDS-1000A Celtron

Tether	
Manufacturer	Lankhorst Ropes
Material	Dyneema
Unstretched Length	5.14m
Diameter	4.0 mm
Theoretical Young's modulus	55 GPa



FIGURE F-2, EXPERIMENT SETUP



FIGURE F-3, EXPERIMENT SETUP

F.3 RESULTS

In Matlab the data was analysed. The first graph in Figure F-5 shows the typical data of a test. From the data can be seen that there is a mass of 327.8 kg attached. After 12 sec a 10kg weight is lifted. At 16 sec the mass is dropped which results in a longitudinal vibration of the mass. The vibration damps out in approximately 30 sec.

First the time is found where the mass is excited and then the next 16 seconds are selected for analysis. The second graph shows the selected data. Due the analogue amplifier there was high frequency noise in signal. By filtering the signal with a low-pass filter at 20hz the high frequency noise was cancelled and the filtered signal is displayed in the third graph.

The frequency of the signal was determined by two methods. First of all a FFT analysis was performed. For all test the FFT showed two peaks (see the fourth graph in Figure F-5). The highest peak is clearly the natural frequency of the tether. The second peak is probably the pendulum motion of the weights. When the mass was excited a small pendulum motion could be seen (Figure F-4). Also the observation that the frequency goes down when the mass goes down agrees with this finding. The second peak was around 4 Hz.

As a second method the theoretical curve (F-5) was fitted to the data with a LSQ curve fitting tool in Matlab. This resulted in a frequency and damping ratio. The fifth graph in Figure F-5 shows the filtered data with the fitted theoretical curve. Also the damping term is separately plotted to show the correspondence. All test results are displayed in Table 15. In the table the unit spring constant and unit damping constant are displayed. The unit spring constant is defined as:

$$k_0 = \frac{k}{l_0},$$

$$c_0 = \frac{c}{l_0}$$

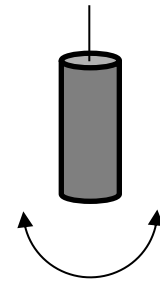


**FIGURE F-4,
NATURAL
FREQUENCY
CYLINDER**

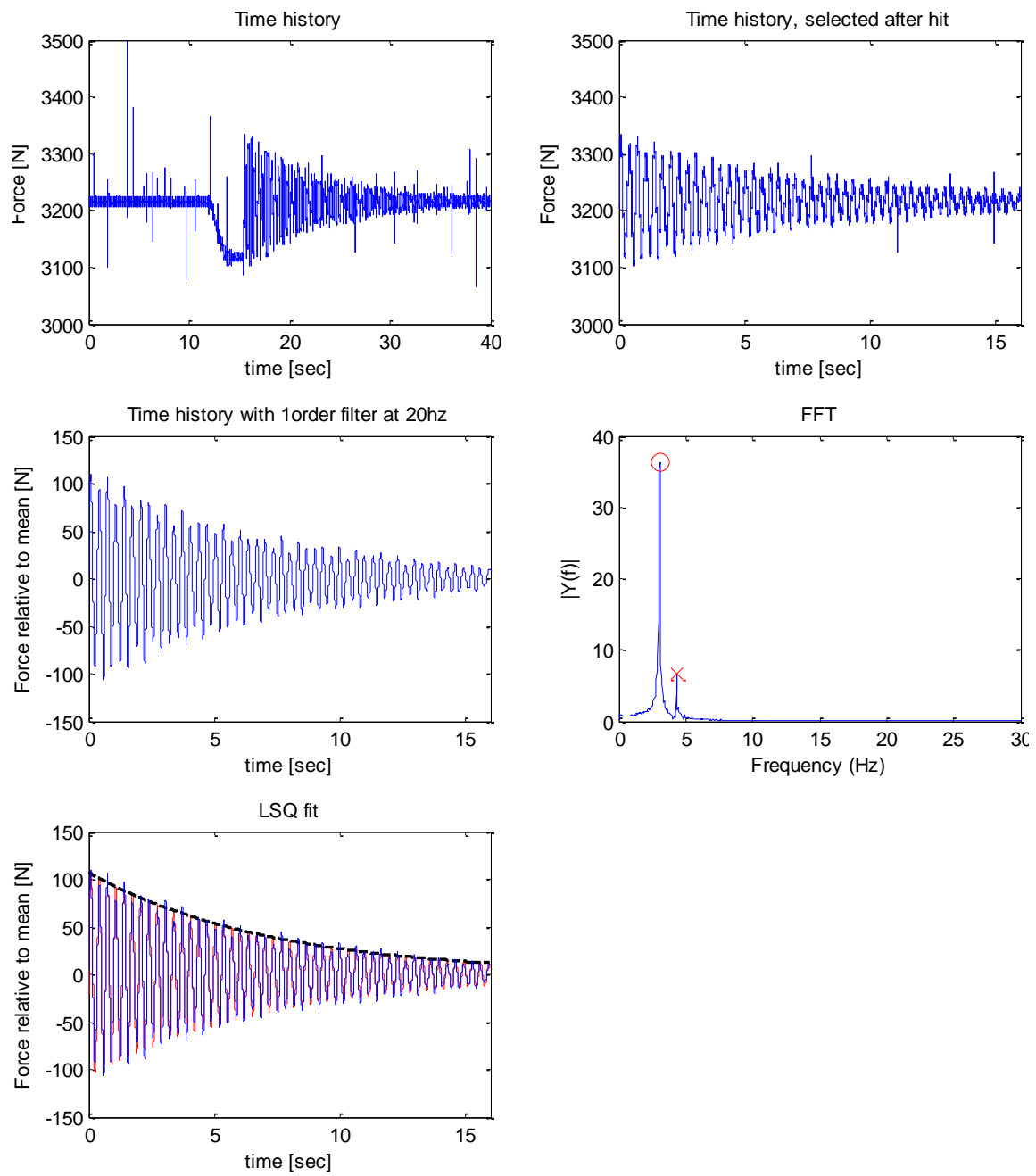


FIGURE F-5, MATLAB RESULTS

TABLE 15, MATLAB DATA

Test	1	2	3	4	5	6	7	8	9
Mass [kg]	327.8	327.8	327.8	217.9	217.9	217.9	97.5	97.5	97.5
Frequency FFT [Hz]	3.0041	3.0518	3.0518	3.5286	3.5286	3.5286	5.5313	5.5313	5.5313
Second Frequency FFT [Hz]	4.3392	4.3392	4.3392	4.4823	4.4823	4.4823	4.0054	4.0054	4.0054
Frequency LSQ fit [Hz]	3.0306	3.0391	3.0438	3.5353	3.5373	3.5395	5.5653	5.5670	5.5639
Damping Ratio ζ	0.0077	0.0072	0.0073	0.0068	0.0064	0.0064	0.0124	0.0138	0.0139
Unit Damping Coefficient [Ns]	496	463	468	341	317	320	434	486	489
Unit Spring Constant [N]	6.1203 $\times 10^5$	6.1545 $\times 10^5$	6.1738 $\times 10^5$	5.5369 $\times 10^5$	5.5432 $\times 10^5$	5.5503 $\times 10^5$	6.1425 $\times 10^5$	6.1464 $\times 10^5$	6.1396 $\times 10^5$
Unit Theoretical Spring Constant [N]	6.9115 $\times 10^5$	6.9115 $\times 10^5$	6.9115 $\times 10^5$	6.9115 $\times 10^5$	6.9115 $\times 10^5$	6.9115 $\times 10^5$	6.9115 $\times 10^5$	6.9115 $\times 10^5$	6.9115 $\times 10^5$

From the table it can be seen that especially the test with 217.9 kg gave different results. A explanation could be that the second frequency is very close to the first frequency. The frequency of the pendulum motion probably influenced the measurements of the frequency of the tether. In the time history a form of coupling can be seen (Figure F-6)

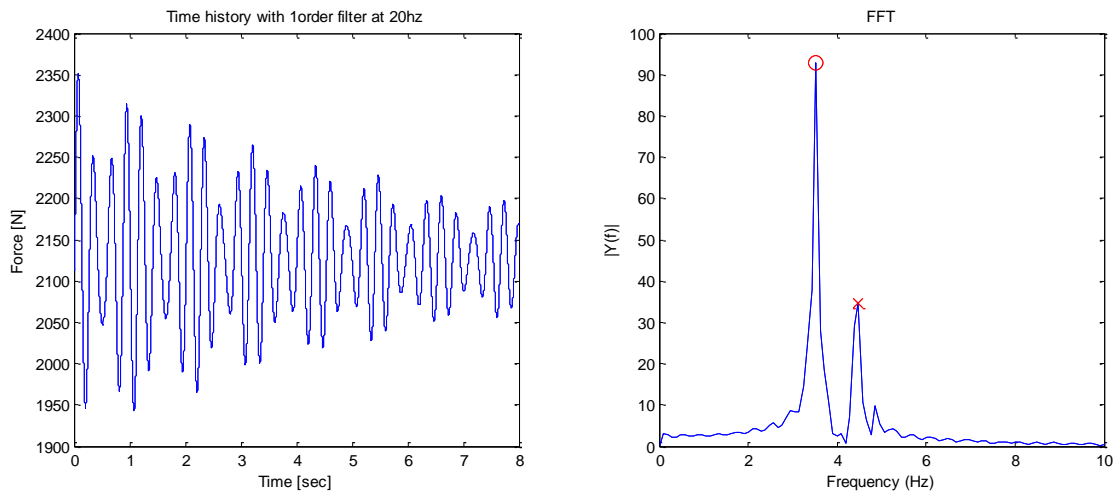


FIGURE F-6, RESULTS TEST 4

When rejecting the results of test 4,5,6 the average unit spring constant and unit damping was found to be :

$$k_0 = 6.1462 \pm 0.0176 \times 10^5 (1\sigma)N$$

$$c_0 = 473 \pm 23 (1\sigma) Ns$$

As a second test the elongation of the tether was measured during loading and unloading the tether. Figure F-7 shows the results. The pre-stretching effect can clearly be seen in the results. Before the test the tether was wound around a cylinder and fully flexible. During loading the tether became 10 cm longer and after a break of 1 hour the tether become an additional 1.6 cm longer due creep effects. During unloading the results are more realistic. A linear fit results in a unit spring constant of $4.8511 \times 10^5 N$. For the calculation of the unit spring constant the length of the end of the test is used as unstretched length.

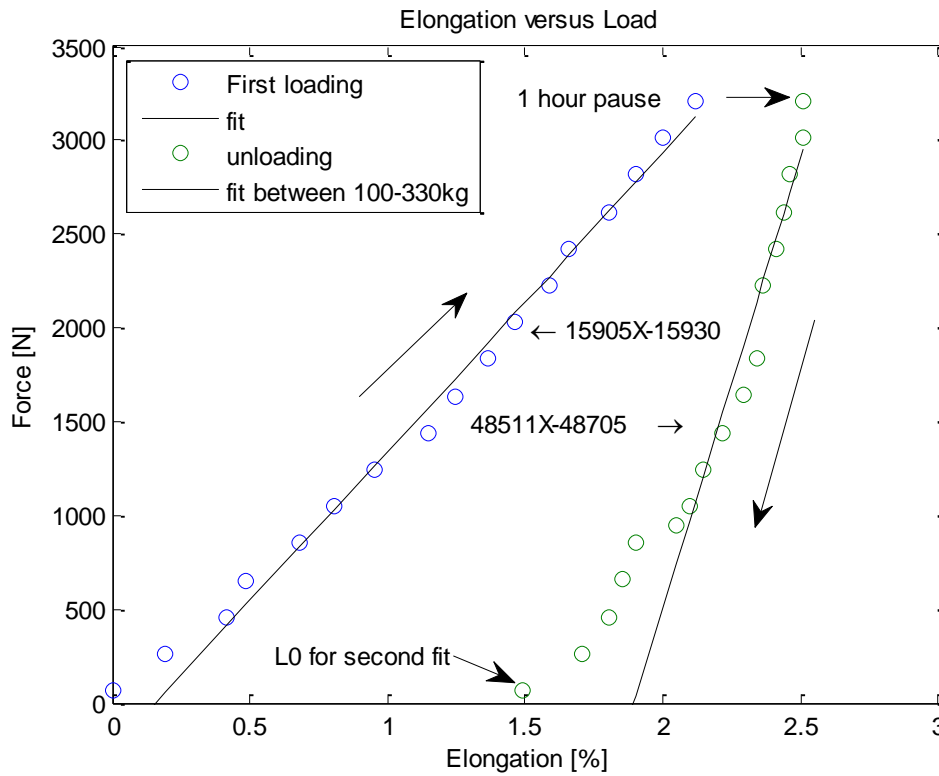


FIGURE F-7, ELONGATION VS. FORCE

It should be noticed that the measured spring constant with the mass-spring oscillator test is higher than the values with the elongation test. This is probably due the fact that creep in the tether and other structural effects of the tether are not measured with the mass-spring oscillator.

11 REFERENCES:

1. Maddison, A., *The World Economy: Historical Statistics*. 2003: Development Centre of the Organisation for Economic Co-operation and Development.
2. REN21, *Renewables 2011 Global Status Report*. 2011 Paris: REN21 Secretariat.
3. Arya, S.P., *Introduction to Micrometeorology*. 2001: Academic Press.
4. Loyd, M.L., *Crosswind kite power*. *Journal of energy*, 1980. **4**(3): p. 106-111.
5. Hassan, G.G., *Market Report High Altitude Wind Energy*. 2011.
6. Schmehl, R. *Lecture Notes, AE4T40 Kite Power and Propulsion*. 2012 [cited 2012 May 2012].
7. Ippolito, M. *Kitegen*. 2012 21 May [cited 2012 May 2012]; Available from: <http://www.kitegen.com/en/kiteblog-2/>.
8. Manwell, J.F., J.G. McGowan, and A.L. Rogers, *Wind Energy Explained: Theory, Design and Application*. 2010: Wiley.
9. Chen, W.F., *Handbook of Structural Engineering*. 1997: CRC Press.
10. Ockels, W.J., *Laddermill, a novel concept to exploit the energy in the airspace*. *Aircraft Design*, 2001. **4**(2-3): p. 81-97.
11. Archer, C.L. and K. Caldeira, *Global assessment of high-altitude wind power*. *Energies*, 2009. **2**(2): p. 307-319.
12. Miller, L., F. Gans, and A. Kleidon, *Jet stream wind power as a renewable energy resource: little power, big impacts*. *Earth System Dynamics Discussion*, 2011. **2**: p. 435-465.
13. Schmehl, R., *Airborne Wind Energy 2011*. 2011: Delft.
14. Schmehl, R., *Die kraft des Drachens, in Erneuerbare Energien*. 2011. p. 64-69.
15. Makani Power Inc. 2012 21 May [cited 2012 21 May]; Available from: <http://www.makanipower.com/>.
16. Terink, E.J., *Kiteplane Flight Dynamics Stability and control analysis of tethered flight for power generation purposes*, in *Aerospace Engineering*. 2009, TU Delft: Delft. p. 240.
17. Furey, A. *Kite, airborne and high altitude wind energy blog*. [web page] 2009 21 May [cited 2012 21 May]; Available from: <http://kiteenergy.blogspot.com>.
18. Institute for Applied Sustainable Science, E.a.T. 2012 21 May 2012 [cited 2012 5 May]; Available from: www.kitepower.eu.
19. HighWind, E. 2012 [cited 2012 12 June]; Available from: <http://homes.esat.kuleuven.be/~highwind/>.
20. SchwissKitePower. 2012 [cited 2012 6 June]; Available from: <http://www.swisskitepower.ch/team.html>.
21. Furey, A. 2011 [cited 2012 6 June]; Available from: <http://www.sussex.ac.uk/Users/adjf20/research.html>.
22. Skysails. 2012 [cited 2012 June 6]; Available from: <http://www.skysails.info/english/company/>.
23. Power, A. 2012 [cited 2012 June 6]; Available from: <http://www.ampyxpower.com/Our-company.html>.
24. KiteGen. 2012 [cited 2012 June 6]; Available from: <http://www.kitegen.com/en/who-we-are/kite-gen-research/>.
25. Windlift. 2012 [cited 2012 June 6]; Available from: <http://windlift.com/team.html>.
26. Enerkite. 2012 [cited 2012 June 6]; Available from: <http://www.enerkite.com/Team.html>.
27. Ockels, W.J., *Wind energy converter using kites*. . 1996.
28. Lansdorp, B. and W.J. Ockels, *Comparison of concepts for high-altitude wind energy generation with ground based generator*, in *The 2nd China International Renewable Energy Equipment & Technology Exhibition and Conference*. 2005: Beijing, China.
29. Lansdorp, B., R. Ruiterkamp, and W. Ockels. *Towards flight testing of remotely controlled surfkites for wind energy generation*. 2007. Hilton Head, SC.

30. Heilmann, J., *The Technical and Economic Potential of Airborne Wind Energy*, in *Institute of Aerosol and Sensor Technology 2012*, University of Applied Sciences Northwestern Switzerland, Utrecht University Internal.
31. MutinyKites. 2012 [cited 2012 August 8]; Available from: <http://www.mutinykites.com/>.
32. GenetrixKitesurf. 2012 [cited 2012 August 1]; Available from: <http://www.genetrixkitesurf.com/>.
33. van den Heuvel, J., *Kitesailing*, in *Applied Sustainable Science Engineering and Technology*. 2010, TU Delft.
34. Schölkopf, M., *Design of a Ground Station for a Kite Power System*, in *Applied Sustainable Science Engineering and Technology*, Technische Universität München. 2011: Delft.
35. Argatov, I., P. Rautakorpi, and R. Silvennoinen, *Estimation of the mechanical energy output of the kite wind generator*. *Renewable Energy*, 2009. **34**(6): p. 1525-1532.
36. Argatov, I. and R. Silvennoinen, *Energy conversion efficiency of the pumping kite wind generator*. *Renewable Energy*, 2010. **35**(5): p. 1052-1060.
37. Anderson, J. and J.D. Anderson, *Fundamentals of Aerodynamics*. 2010: McGraw-Hill.
38. Argatov, I. and R. Silvennoinen, *Structural optimization of the pumping kite wind generator*. *Structural and Multidisciplinary Optimization*, 2010. **40**(1): p. 585-595.
39. Argatov, I., P. Rautakorpi, and R. Silvennoinen, *Apparent wind load effects on the tether of a kite power generator*. *Journal of Wind Engineering and Industrial Aerodynamics*, 2011. **99**(10): p. 1079-1088.
40. Diehl, M., *Real-time optimization for large scale nonlinear processes.*, in *Naturwissenschaftlich-Mathematischen Gesamtfakultät*. 2001, Ruprecht-Karls-Universität: Heidelberg.
41. Diehl, M., H.G. Bock, and J.P. Schlöder, *A real-time iteration scheme for nonlinear optimization in optimal feedback control*. *SIAM Journal on Control and Optimization*, 2005. **43**(5): p. 1714-1736.
42. Baayen, J.H. and W. Ockels, *Tracking control with adaption of kites*. *IET Control Theory & Applications*, 2011. **7**(1): p. 1-10.
43. Baayen, J.H., *Automatic trajectory tracking control of kites*, in *Applied Mathematics*. 2011, TU Delft: Delft. p. 52.
44. Williams, P., et al., *Modeling, Simulation, and Testing of Surf Kites for Power Generation Generation*, in *AIAA Modeling and Simulation Technologies*. 2008, Delft University of Technology, The Netherlands: Honolulu, Hawaii.
45. de Groot, S.G.C., *Modelling the Dynamics of an Arc-shaped Kite for Control Law Design, Design of a Rigid Body Model for Real-Time Simulation using a Multi-Body Reference*, in *Aerospace Engineering*. 2011, TU Delft: Delft. p. 233.
46. Breukels, J., *An Engineering Methodology for Kite Design*, in *Aerospace Engineering*. 2011, TU Delft: Delft. p. 288.
47. Knappskog, H., *Nonlinear control of Tethered Airfoils, Path-following control of Tethered Airfoils*, in *Engineering Cybernetics*. 2011, Norwegian University of Science and Technology.
48. Houska, B., *Internal Paper: A 9DOF Kite Model*. 2009, University of Heidelberg: Heidelberg.
49. Williams, P., B. Lansdorp, and W. Ockels. *Flexible tethered kite with moveable attachment points, part I: Dynamics and control*. 2007. Hilton Head, SC.
50. Williams, P., B. Lansdorp, and W. Ockels. *Flexible tethered kite with moveable attachment points, part II: State and wind estimation*. 2007. Hilton Head, SC.
51. Furey, A. and I. Harvey, *Evolution of neural networks for active control of tethered airfoils*. 2007: Lisbon. p. 746-755.
52. Schwoll, J., ... in *Applied Sustainable Science Engineering and Technology*,. 2012, TU Delft: Delft.
53. Bosch, H.A., *Finite element analysis of a kite for power generation*, in *Precision and Microsystems Engineering, Applied Sustainable Science Engineering and Technology*. 2012, TU Delft: Delft.

54. Mulder, J.A., et al., *Lecture notes, Flight Dynamics*. 2000, Delft University of Technology.
55. Carqueija, P.F.P., *Aerodynamic Investigations of a High-altitude Wind Energy Extraction System*, in *Mechanical Engineering*. 2010, Universidadada Técnica de Lisboa: Lisboa. p. 122.
56. Dadd, G.M., D.A. Hudson, and R.A. Sheno, *Comparison of two kite force models with experiment*. *Journal of Aircraft*, 2010. **47**(1): p. 212-224.
57. Weilenmann, G. and F. Tischhauser, *Preliminary Study on Kite Autonomy - Design, Model and Control -*, in *Autonomous Systems Lab*. 2007, ETH: Zurich.
58. Fagiano, L., *Control of tethered airfoils for high-altitude wind energy generation*, in *Complex System Modeling and Control Group* 2009, Politecnico di torino.
59. Williams, P., B. Lansdorp, and W. Ockels. *Modeling and control of a kite on a variable length flexible inelastic tether*. 2007. Hilton Head, SC.
60. Baayen, J.H., *Modeling a kite on a variable length flexible tether*, in *Aerospace Engineering*. 2011, TU Delft: Delft. p. 30.
61. Santel, C., *Numerical Simulation of Glider Winch Launches*, in *Flight Dynamics*. 2008, RWTH-Aachen: Aachen.
62. Houska, B. and M. Diehl, *Optimal Control for Power Generating Kites*, in *European Control Conference*. 2007: Kos.
63. Houska, B., *Robustness and Stability Optimization of Open-Loop Controlled Power Generating Kites*, in *Mathematik und Informatik*. 2007, Universitat Heidelberg: Heidelberg,. p. 159.
64. Williams, P. *Optimal wind power extraction with a tethered kite*. 2006. Keystone, CO.
65. Williams, P., B. Lansdorp, and W. Ockels. *Optimal cross-wind towing and power generation with tethered kites*. 2007. Hilton Head, SC.
66. Hobbs, S., *A Quantitative study of kite performance in natural wind with application to kite anemometry*, in *Ecological Physics Research Group*. 1986, Cranfield University.
67. Dadd, G.M., D.A. Hudson, and R.A. Sheno, *Determination of kite forces using three-dimensional flight trajectories for ship propulsion*. *Renewable Energy*, 2011. **36**(10): p. 2667-2678.
68. Furey, A. and I. Harvey. *Robust adaptive control for kite wind energy using evolutionary robotics*. in *Proc. Biological Approaches for Engineering*. 2008. University of Southampton, Chilworth Manor, Southampton, UK.
69. Marchand, J., *Energy production with kite Simulation and Test of Prototype*. 2011, Fachhochschule Nordwestschweiz. p. 99.
70. Gaunaa, M., et al., *A computationally efficient method for determining the aerodynamic performance of kites for wind energy applications*, in *EWEA Annual Event 2011* 2011: Brussels (BE).
71. Jehle, C., *Automatic Flight Control of Tethered Kites for Power Generation*, in *Lehrstuhl für Flugsystemdynamik, Applied Sustainable Science Engineering and Technology*. 2012, Technische Universität München: Delft.
72. Erhard, M. and H. Strauch, *Control of Towing Kites for Seagoing Vessels*. Arxiv preprint arXiv:1202.3641, 2012.
73. Argatov, I. and R. Silvennoinen, *Asymptotic modeling of unconstrained control of a tethered power kite moving along a given closed-loop spherical trajectory*. *Journal of Engineering Mathematics*, 2011: p. 1-17.
74. Ilzhöfer, A., *Real-time Automatic Control and Estimation with Application to Power Generating Kites under Varying Wind Conditions*, in *Fakultat fur Mathematik und Informatik*. 2007, Ruprecht-Karls-Universität Heidelberg: Heidelberg
75. Hamilton, J.M., *Vibration-Based Techniques for Measuring the Elastic Properties of Ropes and the Added Mass of Submerged Objects*. *Journal of Atmospheric and Oceanic Technology*, 2000. **17**(5): p. 688-697.
76. Kappel, v., *Unfinished work*, in *Applied Sustainable Science Engineering and Technology*. 2012, TU Delft
77. Verheul, R., *Designsheet Mutiny 25m Excel*. 2012, TU Delft.



Author: Marien Ruppert
06 30288509
MarienRuppert@gmail.com

Delft University of Technology
Asset Institute
015 278 5176
Room 10.07
Kluyverweg 1
2629 HS Delft
The Netherlands